University of Alberta

CMOS Micromachined Devices for Application in Fluids

by

Sandra Esteves

A thesis submitted to the faculty of Graduate Studies and Research in partial fulfillment of the requirements for the degree of Master of Science.

Department of Mechanical Engineering

Edmonton, Alberta

Fall 2000

National Library of Canada
Acquisitions and Bibliographic Services
395 Wellington Street
Ottawa ON K1A 0N4
Canada

Bibliothèque nationale du Canada
Acquisitions et services bibliographiques
395, rue Wellington
Ottawa ON K1A 0N4
Canada

Your file Votre référence

Our file Notre référence

The author has granted a non-exclusive licence allowing the National Library of Canada to reproduce, loan, distribute or sell copies of this thesis in microform, paper or electronic formats.

L'auteur a accordé une licence non exclusive permettant à la Bibliothèque nationale du Canada de reproduire, prêter, distribuer ou vendre des copies de cette thèse sous la forme de microfiche/film, de reproduction sur papier ou sur format électronique.

The author retains ownership of the copyright in this thesis. Neither the thesis nor substantial extracts from it may be printed or otherwise reproduced without the author's permission.

L'auteur conserve la propriété du droit d'auteur qui protège cette thèse. Ni la thèse ni des extraits substantiels de celle-ci ne doivent être imprimés ou autrement reproduits sans son autorisation.

0-612-59801-2

Canada

University of Alberta

Library Release Form

Name of Author: Sandra Esteves

Title of Thesis: CMOS Micromachined Devices for Application in Fluids

Degree: Master of Science

Year this Degree Granted: 2000

Permission is hereby granted to the University of Alberta Library to reproduce single copies of this thesis and to lend or sell such copies for private, scholarly, or scientific research purposes only.

The author reserves all other publication and other rights in association with the copyright in the thesis, and except as hereinbefore provided, neither the thesis nor any substantial portion thereof may be printed or otherwise reproduced in any material form whatever without the author's prior written permission.

Sandra Esteves

(Sandra Esteves)

8720 – 159A Avenue
Edmonton, Alberta
Canada, T5Z 3E8

Date: OCTOBER 6, 2000

ABSTRACT

CMOS-compatible magnetically actuated micromachined cantilevers have been designed, fabricated and tested. The cantilever devices were designed in three sizes in order to determine the effect of geometry on static and dynamic response, and also the effect of fluid viscosity on the ability of micro-cantilevers to resonant in fluids. This work is a precursor to the determination of the suitability of the microstructures to propel or modify fluid flow in a channel.

Experimental results compiled for the static and dynamic behaviours of the cantilevers have been analyzed and compared with finite element and analytical models. These results have also been compared with expressions developed to relate the response of piezoresistive sensors, embedded in the cantilever arms, to the static deflection and vibrational amplitude of the cantilever tip.

University of Alberta

Faculty of Graduate Studies and Research

The undersigned certify that they have read, and recommended to the Faculty of Graduate Studies and Research for acceptance, a thesis entitled **CMOS Micromachined Devices for Application in Fluids** submitted by **Sandra Esteves** in partial fulfillment of the requirements for the degree of Master of Science.

A. Bhattacharyya

Dr. A. Bhattacharyya, Supervisor

Dr. A. M. Robinson, Co-supervisor

Dr. R. P. W. Lawson

Dr. R. W. Toogood

Date: OCTOBER 2, 2000

This thesis is dedicated to the memory of my grandfather

Augusto Esteves,

1919 – 2000.

ACKNOWLEDGEMENTS

I would like to express my gratitude to my supervisors, Dr. A. Bhattacharyya and Dr. A. M. Robinson, for initiating and suggesting this course of research. I would also like to acknowledge the technical feedback, insight and encouragement provide by Dr. W. Allegretto, Dr. R. P. Lawson and Dr. K. Fyfe.

I am also grateful for the invaluable resource support provided by the Canadian Microelectronics Corporation (CMC), as well as the services afforded by the Alberta Microelectronic Corporation (AMC) and the University of Alberta Microfabrication facility. Funding provided by the Government of Alberta through the Province of Alberta Graduate Scholarship and financial support from the Natural Sciences and Engineering Research Council (NSERC) are also duly noted and appreciated.

It is also my wish to extend special thanks to my fellow graduate students: Allen Goh, Julian Amalraj, Vesselin Stoilov, Yuan Ma, and Tiansheng Zhou. Their knowledgeable advice and insightful ideas were perhaps at the time not fully appreciated, but proved to be of great importance. Special thanks are also extended to Stefanie Lee, Colin Michael, Pauli Pitkanen, Gorman Ho, Trevor Semeniuk and Eric Tremblay for their contributions throughout various stages of this work, and to Dave Pape, Bernie Faulkner and Ian Buttar for their technical expertise.

Lastly, I would like to express my thanks to my parents and to my brother Luciano (Looch) for their belief in this project and in myself. I would also like to thank my friends Nicole Brunelle and Lisa Yung for their encouragement, and lastly Keith B. Brown without whom this project would not have been as gratifying or successful.

TABLE OF CONTENTS

Chapter		Page
1. INTRODUCTION		
1.1	Microelectromechanical Systems	1
1.2	Thesis Overview	2
2. OVERVIEW OF MICROMACHINING TECHNIQUES		
2.1	Introduction	5
2.2	Materials in Micromachining	6
2.2.1	Silicon	6
2.2.2	Other MEMS Materials	9
2.3	Micromachining	9
2.3.1	Surface Micromachining	10
2.3.2	Bulk Micromachining	14
2.3.3	CMOS Micromachining	22
3. DEVICE FABRICATION AND ANALYSIS		
3.1	Introduction	29
3.2	Device Fabrication and Mode of Actuation	30
3.2.1	Device Fabrication and Post Processing	30
3.2.2	Mode of Actuation	35
3.3	Device Modeling and Simulation	36

3.3.1 Static Deflection Modeling 36

3.3.2 Dynamic Response Modeling 40

3.3.3 Piezoresistive Polysilicon Physical Sensors 44

3.3.4 Finite Element Simulation 49

4. EXPERIMENTAL OVERVIEW AND RESULTS

4.1 Introduction 55

4.2 Experimental Setup 55

4.2.1 Static and Dynamic response Experimental Method 55

4.2.2 Optical Detection Measurements 59

4.3 Experimental Results and Analysis 62

4.3.1 Static Deflection 62

4.3.1.1 Piezoresistive Response Data 62

4.3.1.2 Optical Detection Data 67

4.3.2 Dynamic Response 70

4.3.2.1 Piezoresistive Response Data 70

4.3.2.2 Optical Detection Data 76

5. DISCUSSION

5.1 Introduction 78

5.2 Static Deflection 79

5.2.1 Deflection in Air 79

5.2.2 Comparison of FEM Simulation and Expression (3.3.26) 83

5.3 Dynamic Response 85

5.3.1 Structural Response in Air 85

5.3.2 Comparison of FEM Simulation and Expression (3.3.27) 93

5.3.3 Comparison of Micro-cantilever Response in Fluids 97

5.3.4 Finite Element Simulation in Fluids 101

5.4 Device design and Optimization 102

5.5 Pumping Performance Testing 104

5.6 Micro-cantilever Applications 106

6. CONCLUSIONS AND FUTURE WORK

6.1 Magnetically Actuated Micro-cantilevers 108

6.2 Future Work 109

REFERENCES 112

APPENDIX 120

LIST OF TABLES

Table	Page
2.1: The relationship between opening, surface orientation, and structure [18, p.55]	18
3.1: Dimensions of cantilever devices.	31
3.2: List of constitutive layer thickness and material properties.	32
5.1: Finite element, analytical, and optical results for Figures 5.7 and 5.8.	89
5.2: Physical properties of fluids utilized during experimentation.	98
5.3: Dynamic response results obtained from small cantilever interaction with fluids.	98
5.4: Dynamic response results obtained from medium cantilever interaction with fluids.	99

LIST OF FIGURES

Figure	Page
2.1: (a) A schematic representation of a lattice. (b) A unit cell shown with shaded plane (111) and corresponding direction [111].	7
2.2: Schematic representations of: (a) <110> and (b) <100> plane orientations.	8
2.3: Surface micromachining: (a) substrate, sacrificial layer and patterned sacrificial layer; (b) patterned structural layer; (c) final structure after sacrificial etching.	11
2.4: Outline of the HEXSIL process: (a) deep silicon mold etch; (b) sacrificial layer deposition; (c) structural layer deposition; (d) release and extraction.	12
2.5: Basic SLIGA method.	13
2.6: Examples of (a) isotropic and (b) anisotropic geometries possible in bulk micromachining.	15
2.7: XeF_2 etching system (chambers and valves) schematic.	20
2.8: Illustrative example of a simple CMOS fabricated micro-cantilever.	23
2.9: CMOS micromachining process. (a) Simple CMOS-fabricated cantilever device indicating cross-section A-A. (b) Cross section A-A following silicon nitride and silicon dioxide patterning and etches.	24
2.10: Cross section A-A following: (a) growth of field oxide and (b) removal of silicon nitride and silicon dioxide layers.	25
2.11: Cross section A-A following: (a) deposition and patterning of poly-	26

silicon and (b) deposition of protective silicon dioxide layer.

2.12: Cross section A-A following: (a) current path definition and (b) via patterning. 26

2.13: Microphotograph of a nested cantilever device. 27

3.1: (a) Photograph of an unetched medium micro-cantilever device; (b) Schematic plan view of a micro-cantilever device. 30

3.2: Schematic cross sections (a) of the micro-cantilever platform (section A-A) and (b) the base of the support arms (section B-B). 32

3.3: Polysilicon piezoresistive element embedded into the base of the support arms of the device. 33

3.4: Deflection due to residual stress of a CMOS-fabricated micro-cantilever device following XeF_2 post-processing. 35

3.5: Magnetic actuation principle for micro-cantilever structures. 36

3.6: Static end deflection and rotation of a homogeneous cantilever beam under the influence of (a) a concentrated point load and (b) a moment. 38

3.7: Discretized micro-cantilever utilized with superposition principle. 39

3.8: Schematic of the total deflection of a micro-cantilever device. 39

3.9: Schematic representation of a fundamental single degree-of-freedom system subject to forced vibrations with viscous damping. 42

3.10: Schematic relating physical quantities related in Equation (3.3.25). 48

3.11: Schematic of the Three-Dimensional structural solid SOLID46. 51

3.12: Schematic of the cross sections of the two layered element configurations used in the micro-cantilever simulations: (a) four layered and (b) six layered 52

elements.

3.13: ANSYS model of a small cantilever device under the influence of simulated Lorentz forces. 54

4.1: Experimental layout of device and permanent magnet. 56

4.2: Experimental layout for determination of static response of micro-cantilever devices. 56

4.3: Experimental layout for determination of dynamic response of micro-cantilever devices. 57

4.4: (a) Assembly diagram and (b) illustration of the cross section A-A of fully prepared die. 58

4.5: (a) Experimental layout and (b) external magnet orientation used in optical method of deflection measurement. 61

4.6: Correlation between reflected beam and micro-cantilever deflection. 62

4.7: Static deflection piezoresistive response for the small micro-cantilever in air and at constant actuating current. 63

4.8: Static deflection piezoresistive response for the medium micro-cantilever in air and at constant actuating current. 64

4.9: Thermal effect for the small and medium cantilevers in air. 65

4.10: Static piezoresistive response for the small cantilever in air. 66

4.11: Static piezoresistive response for the medium cantilever in air. 66

4.12: Static deflection of the small cantilever, measured using optical method. 68

4.13: Static deflection of the medium cantilever, measured using optical method. 68

4.14: Static deflection of the small cantilever due solely to Lorentz forces. 69

4.15: Static deflection of the medium cantilever due solely to Lorentz forces. 69

4.16: Piezoresistive response of small cantilever dynamically actuated in air. 71

4.17: Piezoresistive response of medium cantilever dynamically actuated in air. 71

4.18: Maximum piezoresistive response for given value of Lorentz force. 72

4.19: Piezoresistive response of small cantilever dynamically actuated in distilled water. 73

4.20: Piezoresistive response of small cantilever dynamically actuated in IPA. 73

4.21: Piezoresistive response of medium cantilever dynamically actuated in distilled water. 74

4.22: Piezoresistive response of medium cantilever dynamically actuated in IPA. 74

4.23: Tip deflection of small micro-cantilever, measured using optical method. 77

4.23: Tip deflection of the medium micro-cantilever, measured using optical method. 77

5.1: FEM, analytical, and optical static deflection data for the small cantilever. LN and LP denote optical results, the 0 and 100 % nitride lines are results from ANSYS modeling and SBT denotes results obtained from applying simple beam theory. 80

5.2: FEM, analytical, and optical static deflection data for the medium cantilever. LN and LP denote optical results, the 0 and 100 % nitride lines are results from ANSYS modeling and SBT denotes results obtained from applying simple beam theory. 81

5.3: Curved beam subjected to free end loading. 83

5.4: Static tip deflection results for the small cantilever obtained from FEM 84

modeling and application of Equation (3.3.26).

5.5: Static tip deflection results for the medium cantilever obtained from FEM modeling and application of Equation (3.3.26). 85

5.6: ANSYS results illustrating the first four modes of vibration for the micro-cantilevers. Small Cantilever: (a) 2.5 kHz; (b) 11.9 kHz; (c) 19.5 kHz; (d) 23.8 kHz. Medium Cantilever: (a) 0.9 kHz; (b) 4.3 kHz; (c) 7.1 kHz; (d) 9.4 kHz. 87

5.7: FEM, analytical, and optical measurement dynamic response data for the small cantilever. The 0, 50 and 100 % nitride lines are results from ANSYS modeling and SDFM denotes results obtained from applying the single degree-of-freedom model. 88

5.8: FEM, analytical, and optical measurement dynamic response data for the medium cantilever. The 0, 50 and 100 % nitride lines are results from ANSYS modeling and SDFM denotes results obtained from applying the single degree-of-freedom model. 89

5.9: Micro-cantilever with residue attached to the folded support arms. 92

5.10: Dynamic response results for the small cantilever obtained from FEM modeling and application of Equation (3.3.27). 94

5.11: Dynamic response results for the medium cantilever obtained from FEM modeling and application of Equation (3.3.27). 95

5.12: Schematic of a die prepared for pumping performance testing (performed while devices are dynamically actuated). 105

LIST OF ABBREVIATIONS AND SYMBOLS

α	Thermal coefficient of expansion
A_{member}	Cross-sectional area of support beam
AMC	Alberta Microelectronic Corporation
Al	Aluminum
Au	Gold
$\bar{B}$	Magnetic field vector
c	Coefficient of viscous damping
CH_3COOH	Acetic acid
CIC	Cantilever-in-cantilever
CMC	Canadian Microelectronics Corporation
CMOS	Complementary metal oxide semiconductor
CVD	Chemical vapour deposition
Cu	Copper
δ	Displacement (end deflection)
D	Flexural rigidity
DC	Direct current
DIP	Dual in-line package
ε	Strain
E	Young's modulus
EDP	Ethylene diamine pyrocatechol-water
f, ω	Frequency
$\bar{F}$	Lorentz force
F	Applied load/surface area
Fe	Iron
FEA	Finite element analysis
FEM	Finite element method
GaAs	Gallium arsenide
GF	Gage factor

h	Structural thickness
H_2O	Water
HeCd	Helium cadmium
HF	Hydrofluoric acid
HNO_3	Nitric acid
I	Moment of inertia
I_o	Current
IC	Integrated circuit
IPA	Isopropyl alcohol
φ	Phase angle
k	Stiffness constant
KOH	Potassium hydroxide
$\vec{L}$	Length vector along current path
L	Length of cantilever beam
LIGA	Lithography, electroplating, and micro-molding (X-ray lithographie, galvanoformung, abformtechnik)
LPCVD	Low-pressure chemical-vapour-deposition
m	Mass
M	Bending moment
MEMS	Microelectromechanical systems
MST	Microsystems technology
NaOH	Sodium hydroxide
Ni	Nickel
NiTi	Nickel titanium
OH^-	Hydroxide
P	Concentrated point load
PSG	Phosphosilicate glass
PMMA	Polymethylmethacrylate
ρ	Density
Q	Quality factor

θ	Rotation
r	Radius of curvature
RIE	Reactive-ion etching
$\sigma_{critical}$	Critical buckling stress
SCS	Single crystal silicon
Si	Silicon
Si_3N_4	Silicon nitride
SiO_2	Silicon dioxide
SLIGA	Sacrificial LIGA
t	Thickness
T	Equilibrium temperature during actuation
T_o	Temperature of non-actuated device
TCR	Thermal coefficient of resistance
Ti	Titanium
TiNi	Titanium nickel
TMAHW	Tetramethyl ammonium hydroxide-water
U	Total strain energy
UV	Ultra violet
w_o	Amplitude of vibration
ξ	Damping ratio
XeF_2	Xenon difluoride
ZIF	Zero insertion force
ZnO	Zinc oxide

Chapter 1

INTRODUCTION

1.1 Microelectromechanical Systems

Micromachine is not an unfamiliar term in today's industrialized society. Scientists and researchers throughout the world have conveyed the possibility of miniaturized mechanizations, on the order of microns (10^{-6} m) or nanometers (10^{-9} m), working and redesigning themselves collectively to perform a common task. To many, creations of this size, particularly on the nano-scale, seem improbable due to difficulties that may be encountered in resolving fine structural details or in the barriers encountered against forces and scaling laws at this size; however, science and engineering have already begun to transform the improbable into the plausible.

While only small advances have been made in the area of nano-scale devices, or nano-technology, micro-scale mechanical devices have been widely produced. Miniature devices, or Microelectromechanical Systems (MEMS) as they are referred to in North America and Microsystems Technology (MST) in Europe and Japan, are currently being researched and developed for use in the aerospace, agricultural, industrial and biomedical fields. These devices are proving to be attractive alternatives to their macro-scale counterparts as these devices are not cumbersome, may be batch fabricated and are cost effective. The automotive industry, for instance, utilizes MEMS accelerometers to deploy vehicle airbags; MEMS fuel atomizers are employed in the aerospace and transportation industries; and DNA handling is performed by MEMS biological assay devices [1].

Perhaps one of the most burgeoning and diverse subdisciplines of MEMS is the area of microfluidics. Fluidic systems and micropumps are currently being developed for applications such as drug delivery, chemical analysis, fuel injection and biological sampling. The most common designs for these mechanical micropumps are categorized as positive displacement pumps [2]. Positive displacement pumps achieve the transmission of fluids through controlled contraction and expansion of a membrane or diaphragm used as the principal actuator. The membrane can be actuated based on piezoelectric, thermopneumatic, magnetic, or bimetallic effects [3]-[5]. Essentially, the type of membrane used dictates, and often limits, the stroke of the actuator and therefore the effectiveness of the pump. These pumps are often composed of several moving components and are also susceptible to interference and blockage from dust or air bubbles and wear resulting in leaks and reduced efficiency. Furthermore, some of the present pump designs require complex fabrication processes in order to be manufactured.

Over the past two years, we have researched the possibility of developing a micropump based on simple micro-cantilever structures. Cantilever devices, in comparison, can be easily fabricated and can potentially produce sufficient motion to control or modify fluid flow [6]-[8].

1.2 Thesis Overview

The following thesis presents the findings and conclusions obtained from studying the effect of fluids on the dynamic response of micro-cantilevers. This work is essentially intended as a precursor to the study of micromachined cantilever devices as the principal actuators in a micropump. The micro-cantilever devices are based on

magnetic actuation, produced by a Lorentz force – the product of an interaction of an electric current with an external, static magnetic field. Intricate CMOS-fabricated cantilever devices of this genre were first introduced to the world research community at the University of Alberta [9] and have been shown to be feasible as chemical [10], pressure [11], gas [12], humidity [13], temperature [14], and acceleration sensors [15].

Chapter 2 of this thesis discusses various micromachining techniques that are presently available to fabricate such microelectromechanical devices. Bulk, surface, and CMOS micromachining are discussed, as well as a technique that is currently employed at the Micromachining and Development Laboratory, at the University of Alberta, for post-processing of CMOS devices.

In Chapter 3, an overview of the working principle and the analytical static and dynamic models of the micro-cantilever devices are presented. This chapter also contains background information on the design and fabrication of the structures, as well as a discussion on the Finite Element Analysis that was conducted regarding the micro-cantilever devices.

Experimental procedures utilized throughout the course of this thesis and the analyses of the resultant experimental data are then presented in Chapters 4 and 5, respectively. In the latter chapter, post-processing effects such as the effect of particular structural layers on device response, and the static and dynamic response of the device in different media are discussed. Chapter 5 also correlates experimental findings with results obtained from the models presented in Chapter 3. Possible applications of the device are also discussed.

Lastly, Chapter 6 presents conclusions pertaining to the work completed, as well

as suggestions for future research work involving micro-cantilever devices for fluid control or propulsion.

Chapter 2

OVERVIEW OF MICROMACHINING TECHNIQUES

2.1 Introduction

Electrical devices such as sensors and electronic circuits are well established technically; however, the study of mechanical devices such as microactuators and micromechanisms began over two decades ago. Over the past several years, researchers and engineers have incorporated conventional integrated circuit (IC)-based micromachining techniques into the fabrication of MEMS devices. Miniaturized motors, pumps, and nozzles, among other devices, may be produced using surface, bulk or complementary metal-oxide semiconductor (CMOS) micromachining methods.

The first of these methods, surface micromachining, involves the deposition of structural and sacrificial layers onto a substrate. Etching of these layers can create three-dimensional structures, with layer thicknesses of several micrometers. In contrast, bulk micromachining involves removal of substrate material via use of an etchant. This process allows for the fabrication of several structures such as pits, pyramids, and trenches. Lastly, CMOS micromachining combines the process for development of CMOS circuitry with bulk micromachining techniques.

Essentially, the required characteristics of a given MEMS design dictate which of these micromachining methods will be utilized. Whether it be surface, bulk or CMOS micromachining, the appropriate process is chosen by observing specified device design requirements, such as final structural shape, equipment and material availability, process safety and overall production yield and cost. An overview of the aforementioned

micromachining techniques and their relative merits will be discussed in the following chapter.

2.2 Materials in Micromachining

2.2.1 Silicon

Silicon (Si) is the most commonly used material in micromachining. This is due primarily to the intrinsic mechanical stability of single crystal Si and the possibility of coupling sensors and electronics on a single Si substrate [16, p. 148]. In single crystalline form, silicon is composed of atoms arranged in a diamond-like structure. As with all crystalline materials, this arrangement of atoms forms a repetitive, grid-like pattern or lattice that extends throughout the material. The lattice is comprised of a collection of periodically arranged atoms or lattice points; these points in turn form the basis for the unit cell, which retains the overall shape and lattice point arrangement as the overall lattice [17, p. 51]. A unit cell and its defining lattice points are shown in Figure 2.1(a). By stacking consecutive unit cells, the lattice structure is constructed.

The determination of certain directions and planes within the unit cell are of particular importance to predicting the performance of silicon, as well as other materials incorporated into MEMS, during device fabrication. To identify a plane or direction, a set of integers or Miller indices are used [17, p. 60]. To determine the Miller indices of a plane it is first necessary to identify the intercepts of the plane with the x, y, and z-axes. The reciprocals of the intercepts are then taken and reduced to lowest integers. By this procedure, the shaded plane in Figure 2.1(b) is determined to be (111). Here, the curved

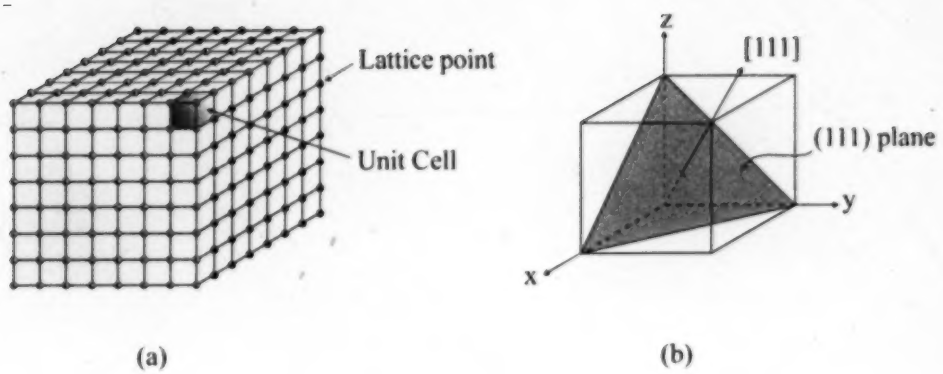

Figure 2.1: (a) A schematic representation of a lattice. (b) A unit cell shown with shaded plane (111) and corresponding direction [111].

brackets denote that the integers 1,1,1 are representative of a plane. The family of planes equivalent by the symmetry of the given crystal, such as (100) and (010) which are crystallographically equivalent to plane (001), are marked as {abc} planes (a, b, and c representing integers). For the planes (100), (010) and (001), for instance, the family of planes is designated by {100}. Similarly, the procedure for finding the Miller indices for direction first involves determining the coordinates of two points on a line that lie along the specified direction. The coordinates of the "tail" of the vector are then subtracted from the "head" of the vector and the results reduced to the lowest integer values. A notation of the form [hkl], where h, k, and l are given by integers, represents a single direction, whereas the notation <hkl> represents the family of parallel vectors. [111] gives the body diagonal shown in Figure 2.1(b), for example, that is normal to plane $(\bar{1}11)$.

Some of the more common crystal orientations used in the IC industry include the

<111>, <110>, and <100> orientations. The first of these orientations has been previously shown in Figure 2.1(b); the remaining orientations are shown in Figure 2.2. The <100> orientation is primarily allocated for use in CMOS technologies [11]. Furthermore, the {111} planes in Si wafers contain the highest packing density [16, p. 148] within the unit cell thereby making it less susceptible to etching. Essentially, the orientation of the chosen Si wafer surface will dictate the shape of any and all features that are to be etched into the substrate. The dependence of micromachining techniques on crystal orientation will be further discussed in a later section of this chapter.

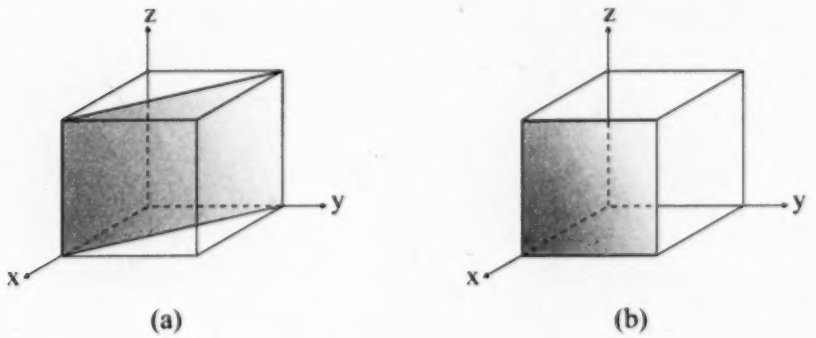

Figure 2.2: Schematic representations of: (a) <110> and (b) <100> plane orientations.

The crystalline structure of Si allows this material to be easily fractured or cleaved; however, despite its seemingly fragile nature, Si is a mechanical material with high strength. Single crystal silicon (SCS), for example, shows a yield strength approximately 3.5 times higher than steel; furthermore, SCS is brittle and yields by fracture, unlike metals, which are ductile and deform plastically before failure [18, p. 50]. Si sensors have also been shown to be very insensitive to fatigue failure when subjected

to high cyclic loading, such as 100 million cycles, without detectable failure [16, p. 159].

Polycrystalline silicon (polysilicon) films have mechanical properties (fractural strength, Young's modulus, hardness, etc.) that differ from single crystal values as a consequence of deposition rates, grain-size effects, and annealing times [19]. For MEMS device fabrication, polycrystalline silicon is deposited using gas-phase decomposition of silane in a low-pressure chemical-vapour-deposition (LPCVD) furnace at temperatures ranging between 585-625°C. The resultant film is compatible with any of the micromachining techniques, to be discussed in this chapter.

2.2.2 Other MEMS Materials

Other materials have been used for specific purposes in micromachining. Nickel (Ni), copper (Cu), gold (Au), iron (Fe) and aluminum (Al) are used to electroplate structural features and to create current traces or paths. Quartz, zinc oxide (ZnO) and titanium-nickel alloy (TiNi) are commonly employed as actuators or membranes. Similarly, new materials, such as, gallium arsenide (GaAs), are emerging for use in the area of optics and communication [1].

2.3 Micromachining

Present micromachining technology allows for the fabrication of mechanical structures with features on the micron (10^{-6} m) scale. As stated previously, the technology required to manufacture these structures is typically divided into two main categories: surface and bulk micromachining. Surface micromachining involves the deposition and subsequent removal of specific layers to create micro-devices.

Conversely, in bulk micromachining, features are etched in the bulk of a single crystal material such as silicon, quartz or glass. The differences in these two methods are discussed in the following sections.

2.3.1 Surface Micromachining

Surface micromachining is a technique by which three-dimensional structures are fabricated from deposited and patterned thin films. The basic concept of this technique was first demonstrated with metal films in the late 1960's. Interest in the technique was later renewed after two major papers on the subject of polysilicon-machined structures were presented in 1987 in Tokyo [18, p. 96]. The following section presents an overview of the basic surface micromachining process, as well as brief discussions pertaining to two specific processes, which are extensions on the surface micromachining theme.

The surface micromachining process sequence will be illustrated using an example of the fabrication of a simple, freestanding cantilever structure as shown in Figure 2.3. The process initially involves the deposition of a layer onto a silicon substrate for electrical isolation (thus, the protective layer is known as an isolation layer) or as a substrate protective layer [18, p. 96]. A thin (approximately 2μm) sacrificial phosphosilicate glass (PSG) layer is then deposited by LPCVD (low-pressure chemical-vapour-deposition). PSG is often used as the sacrificial or spacer layer due to its ease of etching in hydrofluoric acid (HF) [16, p. 231]. The sacrificial layer is then patterned or etched to allow for the creation of the cantilever anchor (Figure 2.3(a)). This is followed by the deposition of a structural film, comprised of polysilicon, metal or an alloy, which is annealed and patterned a second time by reactive-ion etching (RIE) (Figure 2.3(b)).

Lastly, the wafer is immersed in aqueous HF to dissolve the sacrificial PSG layer and later rinsed and dried [19]. The resulting structure, as shown in Figure 2.3(c), is a freestanding cantilever.

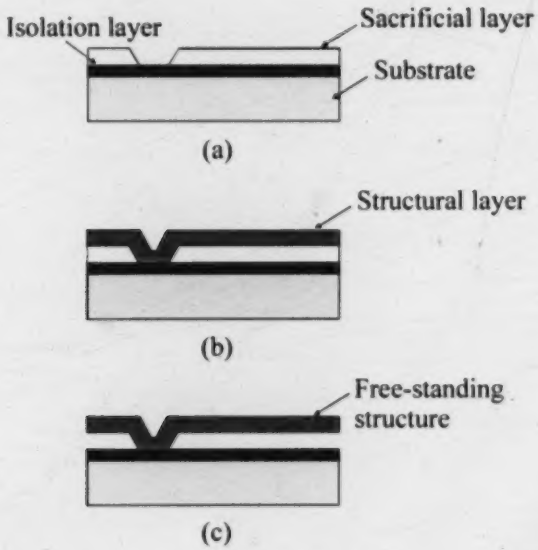

Figure 2.3: Surface micromachining: (a) substrate, sacrificial layer and patterned sacrificial layer; (b) patterned structural layer; (c) final structure after sacrificial etching.

HEXSIL Process

The basic surface micromachining technique can be further extended to create three-dimensional microstructures through the implementation of molds [19]. The HEXSIL process, shown in Figure 2.4, involves the use of deep etched patterns in the silicon wafer to be used as molds for deposited films. The mold is then layered with a sacrificial and a structural layer as depicted in Figures 2.4(b) and 2.4(c), respectively. The exposed surface of the structural layer may then be chemically and/or mechanically

polished at this stage. Etching of the sacrificial film releases the microstructure from the mold. The extracted components may then be utilized as independent devices or as part of larger structures and the mold may be recycled in order to repeat the process.

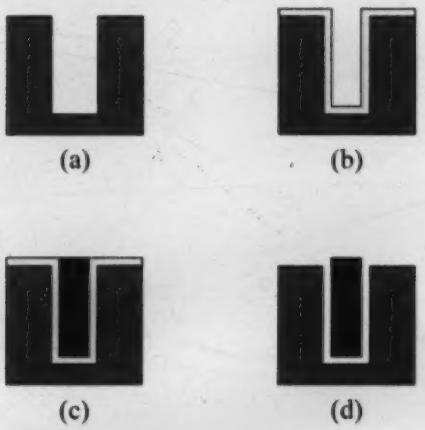

Figure 2.4: Outline of the HEXSIL process: (a) deep silicon mold etch; (b) sacrificial layer deposition; (c) structural layer deposition; (d) release and extraction.

LIGA Process

The LIGA process is also a layer deposition (surface micromachining) technique used for the fabrication of three-dimensional micro-mechanical structures with high aspect ratios (height/width). LIGA, a German acronym for lithography (X-ray lithographie), electroforming (galvanoformung), and micro-molding (abformtechnik), combines X-ray lithography with resist and electroplated metal layers to form the desired structure. This process may also be combined with sacrificial layers, in which case the process is called sacrificial LIGA or SLIGA. The basic SLIGA technique is shown in Figure 2.5.

For the SLIGA fabrication method, processing begins with deposition of a sacrificial layer onto a substrate. This sacrificial layer must withstand X-ray energy and must be easily removed during etching. The layer is then patterned and covered (sputtered) by a plating base (typically titanium (Ti) or nickel (Ni)) that serves as a core for electroplating that occurs in latter steps. A photoresist layer (usually

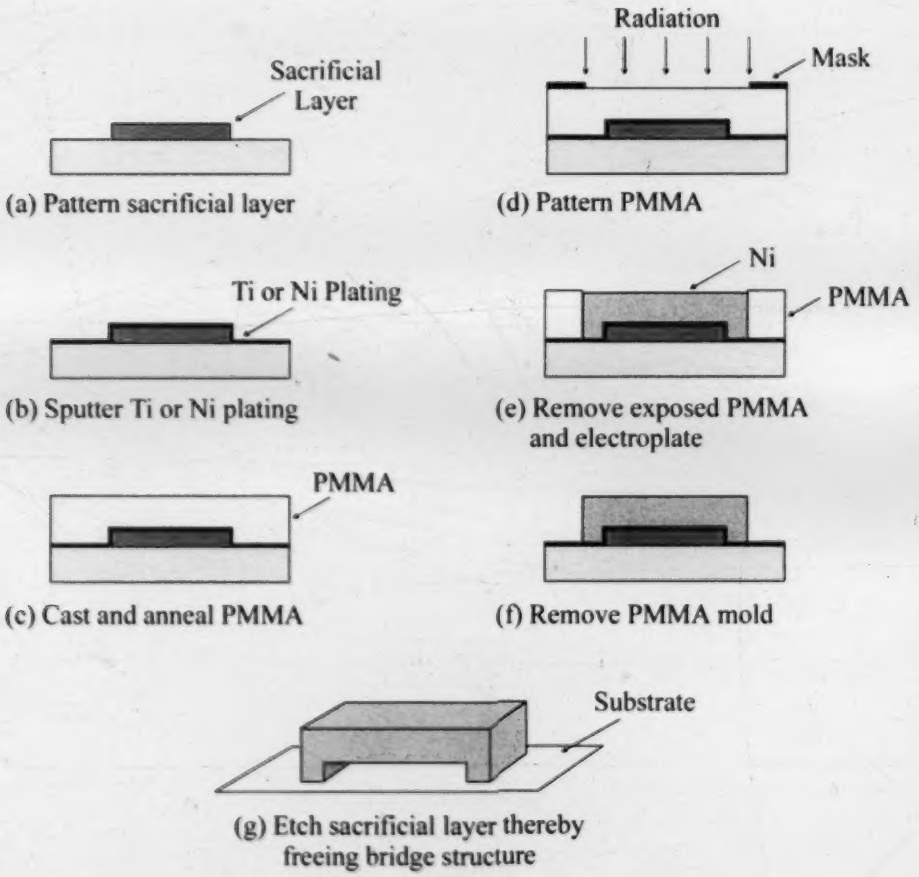

Figure 2.5: Basic SLIGA method.

polymethylmethacrylate, PMMA) is applied over these layers and is cured. A patterned mask is then aligned with the surface of the photoresist and is exposed to X-ray photons [18, p. 147]; removal of the exposed PMMA results in a three-dimensional resist mold.

In the last stages of the process, a core material (nickel or titanium) is electroplated into the exposed cavity. The PMMA is then removed along with the plating base in selective areas. Lastly, the sacrificial layer is etched to undercut freestanding structures. The micro-mold may then be reused to cast new metallic components. For the LIGA process, the steps shown in Figure 2.5 involving the additional sacrificial layer (steps a and g) would be excluded.

Using the procedure outlined above, vertical cantilevers, coils, micro-optical devices, and actuators may be fabricated [18, p. 147]. LIGA, however, is not extensively used in North America due to the high initial investment cost (greater than $30 million US [16, p. 279] for a synchrotron radiation source and approximately $15000 US for a single X-ray mask [16, p. 281]) and limited access to the technology [16, p. 359].

2.3.2 Bulk Micromachining

Bulk micromachining was first reported in the late 1960's and early 1970's; however, the technique was not fully recognized until the late 1970's and early 1980's [18, p. 51]. Micro-mechanical structures fabricated using bulk micromachining concepts are typically constructed using either silicon crystal or composite materials deposited or grown on a silicon substrate [20]. Portions of the silicon or composite material are then selectively removed; this is performed to create membranes; to undercut structures that are physically required to move; or to make holes, channels or vias. For a given

application, the removal of the silicon is achieved through the use of either liquid (wet or aqueous) etchants or vapour or plasma (dry) etchants. The most appropriate type of etching for a given application is determined by several factors such as the required surface roughness of the final device, etchant cost and availability and the required geometry of device features.

Geometries ranging from fully isotropic (rounded features) to anisotropic (flat surfaces and well defined, sharp angles) are attainable through employing bulk micro-machining methods [20]. Typical examples of wet etch geometries are shown Figure 2.6. Structural features are essentially defined by the nature of the chemical reactions, the diffusion of the reactants, and the shapes of the masks used to define the etched regions.

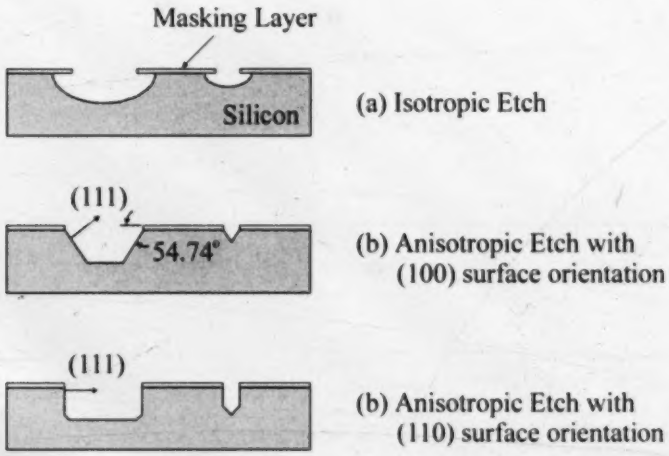

Figure 2.6: Examples of (a) isotropic and (b) anisotropic geometries possible in bulk micromachining.

Wet Etching

Wet etching is employed mainly to clean, shape, or polish structural, micromachined features. This process is also commonly used due to its higher degree of selectivity and reasonably fast etch rates in comparison with dry etching processes. Isotropic etchants, for instance, have been shown to demonstrate etch rates of tens of μm/minute; anisotropic etchants have demonstrated rates of 1 μm/min whereas dry etching rates for typical dry etchants are approximately 0.1 μm /min [16, p. 163].

Isotropic Wet etching

Isotropic etchants etch in all crystallographic directions at the same rate. Essentially, the etchant moves downward and outward from the mask opening thereby undercutting the masked surface and both deepening and widening the etched opening. An example of undercutting is illustrated in Figure 2.6(a).

In the case of aqueous chemistries, etching of silicon is achieved by using highly reactive acids or bases. The most common isotropic wet etch is HNA, a mixture of hydrofluoric acid, nitric acid (HNO_3), and acetic acid (CH_3COOH) [20]. This mixture causes the oxidation of the silicon while also forming soluble silicon compounds.

These reactions are very complex, therefore a brief simplified explanation of the overall reaction process is discussed here. In using highly reactive acids, isotropic etching usually involves the injection of an oxidant into the silicon [16, p. 164]. Nitric acid in the HNA mixture acts as one such oxidant creating holes in the silicon. The holes attack the covalent bonds of the Si thereby oxidizing the material and resulting in the formation of Si^{++} and Si^{+} [20]. These Si fragments are subsequently attached to OH^- to form SiO_2.

Following this association, the hydrated Si reacts with a complexing agent (i.e. HNO) present in the etching solution and the result is the dissolution of the reaction products into soluble silicon compounds.

This process is comparatively inexpensive, is moderately safe, and is adequate for etching structures such as membranes, grooves, and reflective surfaces. A comprehensive review of isotropic etchants and their intended applications may be found in Kern and Dechert [21].

Anisotropic Wet Etching

Wet anisotropic etching, unlike other aqueous etching methods, involves preferential directional etching [18, p. 51]. Anisotropic etchants, or crystal-orientation-dependent etchants, such as potassium hydroxide (KOH) and sodium hydroxide (NaOH), etch much faster in one crystallographic direction than in another. The maxima of etch rates, for instance, coincide with the (133) planes. Conversely, the (111) planes of silicon etch at a slower rate than other crystal planes. These planes, (111), are generally either at 54.74^0 to the surface of the crystal or perpendicular to it as shown in Figure 2.6(b).

Exploiting the orientation dependence of the etchant yields a variety of fabricated shapes. Truncated pyramids or trenches may be created by properly aligning a specified mask shape with a given surface orientation [18, p. 55]. To obtain a truncated pyramidal pit, for example, a square mask must be aligned with a (100) surface plane. If the edges of the mask are misaligned, concave corners and edges will be undercut [18, p. 55]. Table 2.1 indicates the relationship between properly oriented elemental shapes, surface orientation and the final structure.

Table 2.1:

The relationship between opening, surface orientation, and structure [18, p. 55].

Opening	Surface Orientation	Structure
Square	(100)	Pyramidal or truncated pyramidal pit
Rectangle	(100)	Rectangular pit (trench)
Circle	(100)	Pyramidal pit
Arbitrary Shape	(100)	Rectangular pit
Square	(110)	Hole with vertical side walls
Rectangle	(110)	Hole with vertical side walls

As with all engineering processes, the selection of an appropriate anisotropic etchant is dictated by a number of factors. Ease of etchant handling, toxicity, IC-compatibility and desired structural surface smoothness are some of the factors that influence etchant selection. Ethylene diamine pyrocatechol-water (EDP), KOH, and tetramethyl ammonium hydroxide-water (TMAHW) have all been incorporated into the bulk micromachining process; however, these etchants do not satisfy certain aspects of the aforementioned selection criteria. EDP, for instance, has been shown to etch aluminum and silicon dioxide at rates of approximately 10 nm/min and 10 nm/hr respectively [11]. More importantly, EDP has been reported to cause allergic respiratory sensitization and to be a toxic corrosive. Similarly, KOH shows poor selectivity for Si and SiO_2; is incompatible with IC fabrication methods and may cause blindness if contact

with the eyes occurs. Lastly, TMAHW is poisonous if absorbed through the skin and may cause severe skin and eye irritation if not used with extreme caution.

Vapour Phase Etching

Dry etching may be achieved with suitably reactive gases or vapours [20]. In vapour phase etching, the reactions of the etchant with the structural layer rely on the absorption and subsequent dissociation of fluorine-containing compounds (noble gas fluoride and interhalogens).

Xenon Difluoride Etching Process

Xenon difluoride (XeF_2), is one such fluorine compound, which is used as part of an isotropic dry-etch process utilized by, but not exclusive to, researchers at the University of Alberta. XeF_2 is in granular crystalline form at standard room conditions; however, the crystals sublimate into a vapour when employed in environments of pressure less than its equilibrium vapour pressure (approximately 4.5 Torr).

XeF_2 provides high selectivity for aluminum, silicon dioxide, and photoresist. These properties make this etchant very useful for CMOS post processing. At present, however, there is a large discrepancy amongst available literature as to the effects of XeF_2 on the silicon nitride layer that covers the surface of CMOS devices. Winters and Coburn [22] state that silicon nitride is not etched by exposure to XeF_2, whereas Williams and Muller [23] quote an etch rate of 0.012 μm/min for stoichiometric silicon nitride. Furthermore, qualitative observation, by researchers at the Micromachining Applications and Development Laboratory at the University of Alberta, of nested cantilever structures

has shown that these devices have larger amplitudes of vibration after having been etched using xenon difluoride as compared to devices released with EDP [24]. This observation implies that the silicon nitride layer is etched.

The structures studied for this thesis were post-processed in a XeF_2 etch. The etching system utilized, shown partially in Figure 2.7, consists primarily of three chambers and computer-controlled flow valves between chambers. Mechanical components, such as a pump, a Zeolite trap (used to contain any back streaming gases or oil droplets from the pump), and a nitrogen gas source also comprise part of the complete etching system.

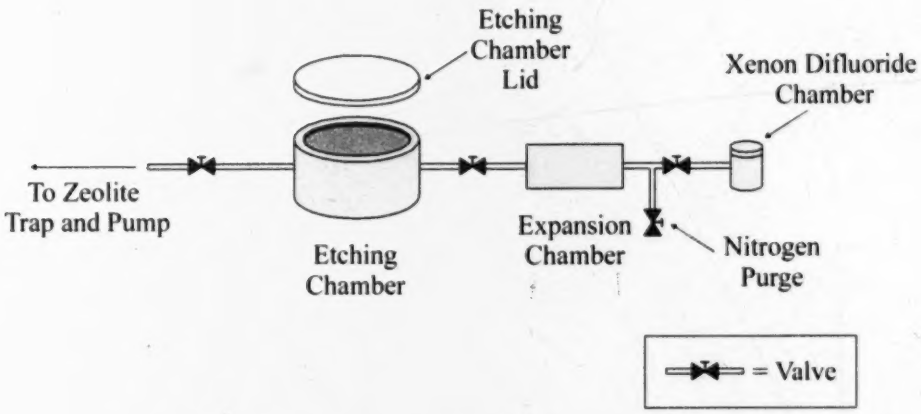

Figure 2.7: XeF_2 etching system (chambers and valves) schematic.

Initially, the device is placed in the etching chamber and the chamber lid is held in place under vacuum. Vacuum conditions within the system are created by pumping the chambers and system lines to approximately 50 mTorr. The system is then purged via nitrogen gas to clean the apparatus of any extraneous gases and water vapour. Once the system has been purged, the XeF_2 gas is allowed to expand into the expansion chamber

for approximately 1 minute. Following this pressurization period, the gas is passed into the etching chamber where the etching process occurs for approximately another minute. The gas is then expelled from the etching chamber, and the process is repeated for another three sequences of these steps, collectively termed as etch pulses.

After having undergone four complete etch pulses, the etching system is re-purged and the etching reinitiated. During the course of the etching process, the progress of the release of the structures from the substrate is monitored visually via the use of a microscope. Once fully freed from the substrate, the etch pulses are terminated, the device is removed, and the system is again sealed and pumped down.

Plasma Etching

Lastly, in plasma etching or reactive ion etching (RIE), external energy in the form of radio frequency power drives chemical reactions [20]. The kinetic energy of stray electrons is increased to levels at which the electrons can break bonds in the reactant gases, forming ions that are later neutralized. A variety of chlorofluorocarbon gases are produced as bi-products of the reaction; however, these gases are utilized during the process in parallel with the etching to form polymers on sidewalls so as to inhibit lateral silicon etching. A full range of isotropic through anisotropic etches are available using these methods. A unique feature of these etches is the ability to control the degree of anisotropy during the etch process via the plasma chemistry; therefore, the undercutting of fragile mechanisms is an appropriate task for dry-etching methods.

2.3.3 CMOS Micromachining

CMOS micromachining was first publicly disclosed as a viable method to manufacture MEMS devices by researchers from the University of Alberta in 1988 [25]-[26]. Since then, structures such as mechanical gas pressure sensors [11] and cantilever microresonators [27] have been developed and extensively tested at the Micromachining Applications and Development Laboratory at the University of Alberta. A simplified version of the CMOS process used to create such structures is presented in the following section. This process is discussed through introducing the steps required to fabricate a simple cantilever device shown in Figure 2.8. The device is comprised of a fixed-end beam, complete with a metal current path about the perimeter of the structure and a polysilicon piezoresistive element at the base of the beam. The structure lies upon the surface of the substrate on which it is created and is released by one of the post-processing etches described earlier in this chapter. A detailed discussion of the CMOS process as used for IC design can be found in [28].

CMOS processing is initiated by the fabrication of defect-free, crystalline (single crystal) wafers or substrates. Wafers are produced from rods or ingots of single-crystalline silicon that are pulled from molten, impurity-free (less than 1 part-per-billion impurity levels [29, p. 22]) silicon, which are then cut into disks approximately 1 mm in thickness. The resulting wafers are then polished to remove damage sustained during cutting and fine polished with SiO_2 (silicon dioxide) particles in an aqueous NaOH solution. Once the wafers have been fabricated, a thin layer of SiO_2 is grown onto the surface of the substrate. This layer serves to protect the surface of the device to be processed and to prepare the substrate for the extensive lithography process that follows.

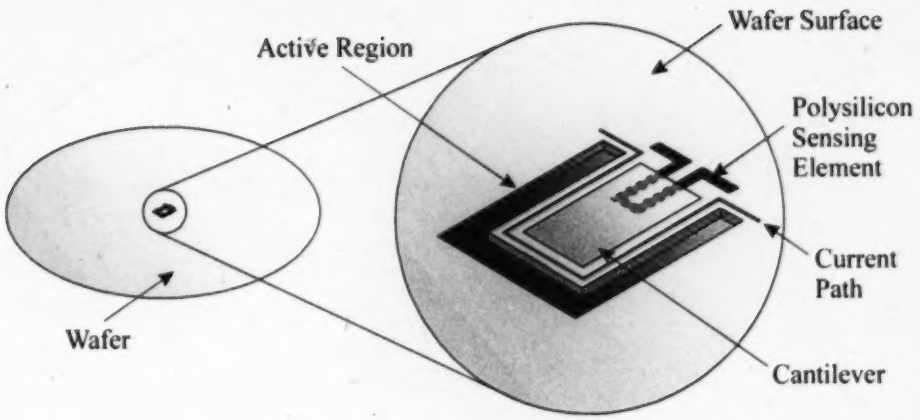

Figure 2.8: Illustrative example of a simple CMOS fabricated micro-cantilever.

The first step in the lithography process involves the definition of *active regions*. In MEMS designs, these regions represent the void areas that separate the outline of structures from the rest of the surface of the device. In Figure 2.8, for instance, the grey, shaded region surrounding the structure illustrates the active region for the simple cantilever device. To define these regions, silicon nitride (Si_3N_4) is deposited onto the surface of the wafer via chemical-vapour-deposition (CVD), followed by the application of a positive photo-resist. A mask containing the desired image of the active regions is then aligned with the surface of the wafer and exposed to ultraviolet (UV) radiation. In using a positive photo-resist, regions that are covered by opaque sections of the mask will remain intact, whereas transparently masked regions will soften and subsequently be removed by phosphoric acid. The remaining silicon nitride acts as a mask to protect active regions from a thick oxide layer that is grown in the next step. SiO_2 that is not

protected by the silicon nitride is also removed with a hydrofluoric acid etch. The resulting layer configuration is shown in Figure 2.9.

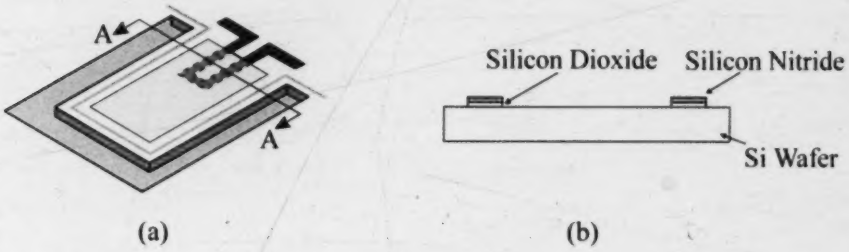

Figure 2.9: CMOS micromachining process. (a) Simple CMOS-fabricated cantilever device indicating cross-section A-A. (b) Cross section A-A following silicon nitride and silicon dioxide patterning and etches.

Next, a thick layer of field oxide (SiO_2) is grown. This layer may be grown using one of two methods. The first method, known as a wet process, entails introducing water vapour over the surface of the device at a moderately high temperature. The water is absorbed into the silicon and reacts as

$$Si + 2H_2O \rightarrow SiO_2 + 2H_2 \qquad (2.3.1)$$

The second of the two processes involves introducing oxygen over the surface of the wafer in order to catalyze the following reaction:

$$Si + O_2 \rightarrow SiO_2 \qquad (2.3.2)$$

Both processes occur at high temperatures of approximately 800 – 1200°C, therefore the resulting oxide is often termed as a thermal oxide. The silicon nitride layer is then removed using hot phosphoric acid and the silicon dioxide previously protected by the silicon nitride is removed via a hydrofluoric etch. This layer growth and subsequent removal of superfluous layers are illustrated in Figures 2.10(a) and (b) respectively.

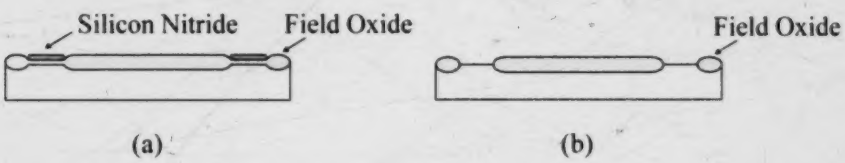

Figure 2.10: Cross section A-A following: (a) growth of field oxide and (b) removal of silicon nitride and silicon dioxide layers.

Polysilicon material is then deposited onto the entire surface via CVD. The polysilicon is then patterned in a similar manner to that used for the active region definition. The cross-sectional view of the device at this stage is illustrated in Figure 2.11(a). In the given example, the patterned polysilicon will serve as a piezoresistive-sensing device for the monitoring of cantilever deflection. This concept, of piezoelectric sensors, will be discussed in Chapters 3 and 4. The wafer is then covered anew, as shown in Figure 2.11(b), with a protective silicon dioxide layer that is approximately 0.25 – 0.5 μm thick and contact regions are patterned.

Metal 1, which in the example serves as a current path, is then deposited onto the device, patterned, and then etched. Historically, aluminum has served as the principle

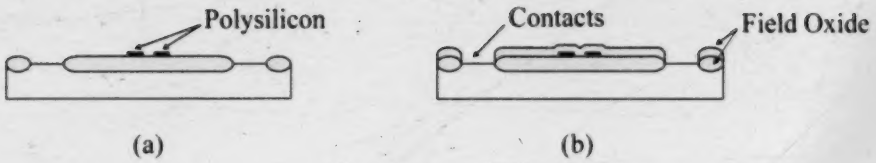

Figure 2.11: Cross section A-A following: (a) deposition and patterning of polysilicon and (b) deposition of protective silicon dioxide layer.

deposited metal; however, other metals such as tungsten have also been incorporated into the process. The metal layer is then protected and isolated from additional metal layers by the addition of another CVD SiO_2 layer. At this stage of the process, vias, akin to contacts, are opened, as shown in Figure 2.12(a). Additional metal layers, may also be added at this point in the process. In the simple cantilever device, used to illustrate the CMOS process, an additional metal layer is deposited on to the central portion of cantilever, as shown in Figure 2.12(b) so as to serve as a mirror. This mirror is often used in optical measurement techniques to determine device deflection.

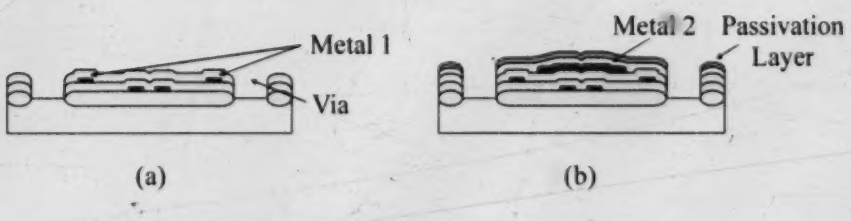

Figure 2.12: Cross section A-A following: (a) current path definition and (b) via patterning.

After the last metal layer is deposited, a thin, protective passivation layer is deposited over the entire device. This layer typically consists of SiO_2; however, an additional layer of Si_3N_4 is often also deposited to protect the device from moisture. The final layer configuration is depicted in Figure 2.12(b).

An example of a CMOS-processed structure is shown in Figure 2.13. This figure illustrates a magnetically actuated nested cantilever, or cantilever-in-cantilever (CIC), device. This device has been employed as a pressure sensor [11], a magnetic field sensor [30], and a thin film deposition monitor [31].

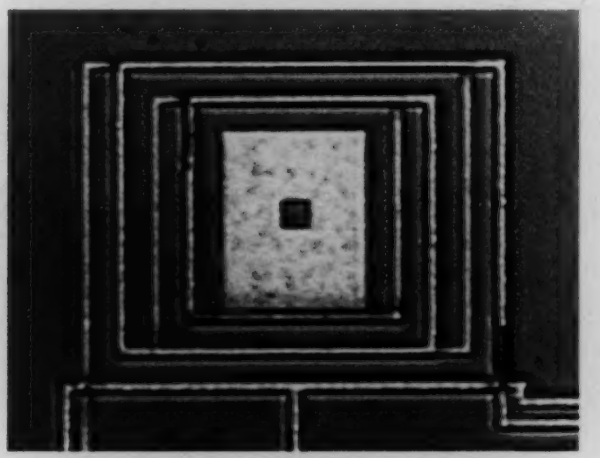

Figure 2.13: Microphotograph of a nested cantilever device.

Essentially, new advances in micromachining, such as LIGA and HEXSIL, and innovative implementation of known technologies, such as the CMOS IC-fabrication process, are allowing for the continuous refinement of MEMS devices. Present technologies, however, must be further advanced in order to create a multitude of novel

microelectromechanical systems that are perhaps not feasible with the processes now available to industry and research communities.

Chapter 3

MICRO-CANTILEVER DESIGN AND MODELING

3.1 Introduction

Actuators are employed in order to perform specific tasks on surrounding environments in response to a driving input or signal. Microbridges, diaphragms, rotational shells, and cantilever beams are common structures used as actuators in a variety of MEMS devices [32, pp. 12-18]. At the micro-level, these devices do not always function comparably with their macro-scale counterparts. Gravitational effects, for instance, are considered to be negligible on micron-sized devices and surface tension effects become very significant [16, p. 406]. Due to these factors, it is desirable, and often necessary, for the behaviour of a MEMS device to be fully characterized. For the devices presented in this thesis, it is of particular importance to characterize the behaviour of the micro-cantilevers in a variety of media. Mechanical behaviour of the cantilevers is greatly affected by the medium in which the devices are immersed, thereby affecting the ability of the microelectromechanical system to transport or modify fluid flow.

In this chapter, a description of the design and method of actuation of the micro-cantilever devices is presented. Theoretical discussion concerning the static and dynamic characterizations of the devices is also presented, as is an overview of the theory involving the response of piezoresistive elements and a derived relationship of response to device deflection. Lastly, an introduction to the Finite Element Analysis technique employed to simulate device response is given.

3.2 Device Fabrication and Mode of Actuation

3.2.1 Device Fabrication and Post Processing

The micro-cantilever devices investigated for this thesis are comprised of simple platforms suspended within a channel via a folded support arm configuration, as shown in Figures 3.1(a) and (b). The support arms, which are 20 μm in width for all devices, were included in the device design so as to allow for greater deflection of the platform free-end in and out of the plane of the device surface. Three devices of similar geometry, but differing dimensions were designed and fabricated. These devices are suspended in series within a channel and are arranged from the smallest to the largest structure. Figure 3.1(a) shows the medium-size cantilever, which is flanked on the top and bottom of the photograph by the smaller and larger cantilevers (which are not shown), respectively.

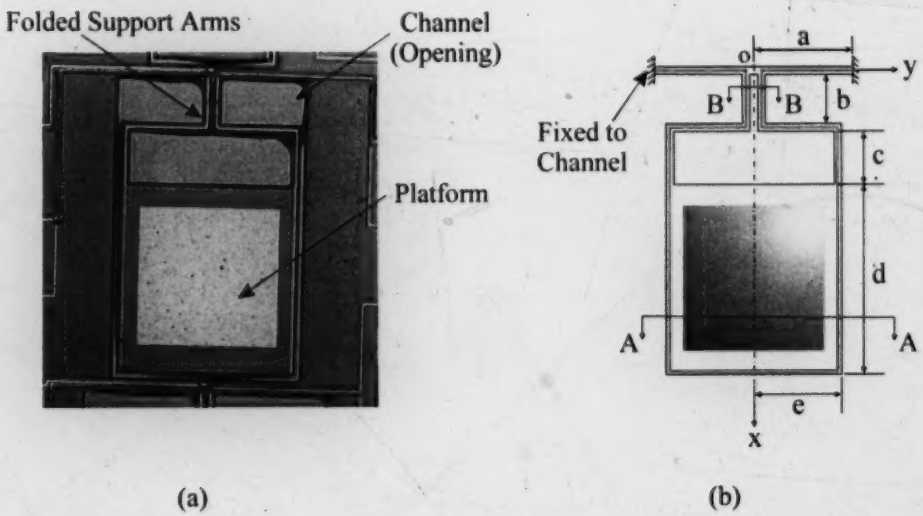

Figure 3.1: (a) Photograph of an unetched medium micro-cantilever device;
(b) Schematic plan view of a micro-cantilever device.

The overall geometry of the devices is shown in Figure 3.1(b) and the dimensions of the devices, associated with the parameters - a, b, c, d, e - shown in this figure, are summarized in Table 3.1.

Table 3.1: Dimensions of cantilever devices.

	Device Dimensions [μm] as Indicated in Figure 3.1				
Cantilever	a	b	c	d	e
Small	200.0	90.0	65.0	430.0	180.0
Medium	295.0	140.0	158.5	557.5	275.0
Large	380.0	140.0	158.5	657.5	360.0

The geometries and various structural (layer) features identified for the manufacture of the devices were created using CADENCE, a computer-aided drafting package supplied by the Canadian Microelectronics Corporation (CMC). Following the design layout, the devices were fabricated through the CMC using the Mitel Corporation 1.5 μm CMOS fabrication process. This process, similar to the CMOS process outlined in the previous chapter, can resolve features as small as 1.5 μm (hence the process title).

Due to this method of fabrication, the micro-cantilevers are layered, composite structures involving a stacking of materials. Schematic (not to scale) cross sectional views A-A, taken across the width of the platform, and B-B, taken across the base of the support arms (as illustrated in Figure 3.1(b)), are shown in Figure 3.2; the material properties of the cantilever structural layers are summarized in Table 3.2. Additional layers are present in cross section B-B due to the presence of polysilicon piezoresistive

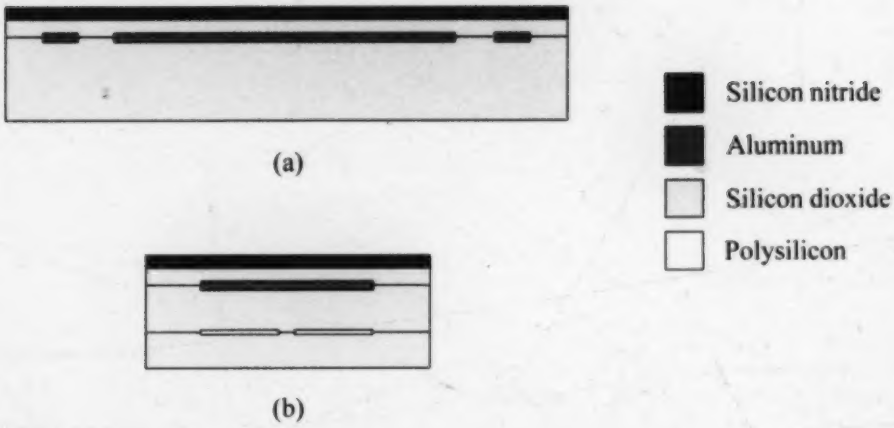

Figure 3.2: Schematic (not to the same scale) cross sections (a) of the micro-cantilever platform (section A-A) and (b) one of the two support arms in section B-B.

Table 3.2: List of constitutive layer thickness and material properties.

Layer	Thickness [μm]	Young's Modulus [GPa]	Poisson's Ratio	Density [kg/m^3]
Silicon nitride	0.5	380	0.24*	3100
Silicon dioxide	0.5	75	0.17	2200
Aluminum (Metal2)	0.8	70	0.33*	2700*
Silicon dioxide	1.6	75	0.17	2200
Polysilicon (Poly1)	0.3	150	0.23	2320
Silicon dioxide	1.0	75	0.17	2200

NOTE: Values for the thickness of the layers were ascertained from information pertaining to the Mitel 1.5 μm CMOS fabrication process. In this process, the aluminum and polysilicon layers present in the micro-cantilevers are termed Metal2 and Poly1,

respectively. Material properties were obtained from reference [33]; properties marked with an asterisk denote bulk material values whereas the remainder of the values pertain to thin films.

elements at the base of the arms. These sensors, shown in Figure 3.3, were incorporated into the devices, so as to allow for the determination of cantilever deflection. The use of piezoresistive sensors in MEMS devices will be discussed later in this chapter.

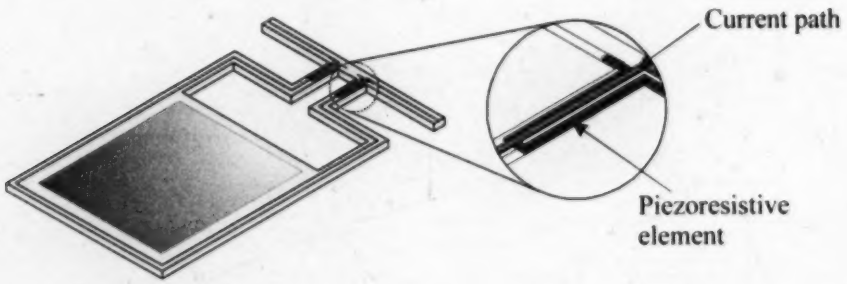

Figure 3.3: Polysilicon piezoresistive elements embedded into the base of the support arms of the device.

Of the structural layers, two are of particular interest to the overall function of the devices – the silicon nitride and aluminum layers. As previously stated in Chapter 2, it is the uppermost layer, the silicon nitride, which may be partially or wholly etched by XeF_2. This layer has a modulus of elasticity that is approximately five times that of the aluminum and silicon dioxide, therefore the subsequent exclusion or inclusion of this layer into device models will greatly affect the results. For the dynamic response, for instance, inclusion of the silicon nitride (or passivation) layer will result in lesser tip

deflections and a higher resonant frequency than a model of similar geometry in which the passivation layer is excluded.

The second layer that is of particular interest is the aluminum layer. This layer, as shown in Figure 3.2(a), is comprised of an aluminum mirror in the center of the structures, and a 10 μm-wide current path around the edges of the devices, which is essential in the magnetic actuation of the devices. A nominal gap of 5 μm separates the edges of structure from the trace; this gap is required in order to conform to specific design rules that are followed during manufacture of the CMOS devices. If the gap separating the aluminum from the device edges is less than the specified minimum, the aluminum may be etched during fabrication, thereby destroying the current path.

Following receipt of the devices from CMC, the devices were packaged, bonded and etched in XeF_2. Release of the structures required approximately 28 etch pulses resulting in near-complete undercutting the Si substrate that supports the cantilever devices. This undercutting served to increase the fragility of the devices and led to cracking and breakage of bonding pads if the devices were not handled with extreme care.

Following etching, residual deflections of approximately 300, 450, and 750 μm were determined for the small, medium, and large cantilevers respectively. Residual deflections, as illustrated in Figure 3.4, are a result of an intrinsic stress gradient, which is due to the various thermal cycles undergone by the structural layers during layer deposition. As related in Chapter 2, the layers utilized to form the micro-cantilevers are deposited at differing rates and temperatures. As the films are grown and the fabricated structures are subsequently cooled, certain films comprising the structure may shrink

more than others; differing thermal expansion coefficients for the various materials used during the fabrication process result in the shrinkage of layers. The stress that results from the deposition methods used during CMOS micromachining may result in thin films that are either in tensile or compressive stress, which in turn will warp the released structures and affect the dynamic response of the cantilevers.

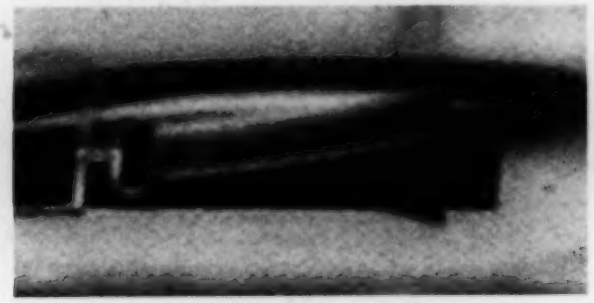

Figure 3.4: Deflection due to residual stress of a CMOS-fabricated micro-cantilever device following XeF_2 post-processing.

3.2.2 Mode of Actuation

Actuation of the devices is achieved via Lorentz forces, as illustrated in Figure 3.5. In this figure, the symbol I_o denotes the actuation current, $\vec{L}_i$ indicates the length of a straight aluminum trace over which the magnetic force acts and $\vec{B}$ represents the imposed, external magnetic field. A Lorentz force, given by

$$\vec{F}_i = I_o \vec{L}_i \times \vec{B} \qquad (i = 1, 2, \ldots n) \qquad (3.2.1)$$

arises from the interaction between the current and the magnetic field, thereby causing the deflection of the micro-cantilever. In Equation (3.2.1), the subscript i denotes the current path (either in a support arm or at the end of the platform) on which the Lorentz force, F_i, is produced, and n represents the total number of current paths on which Lorentz forces are produced. Direct and alternating currents will cause the devices to deflect statically and dynamically respectively.

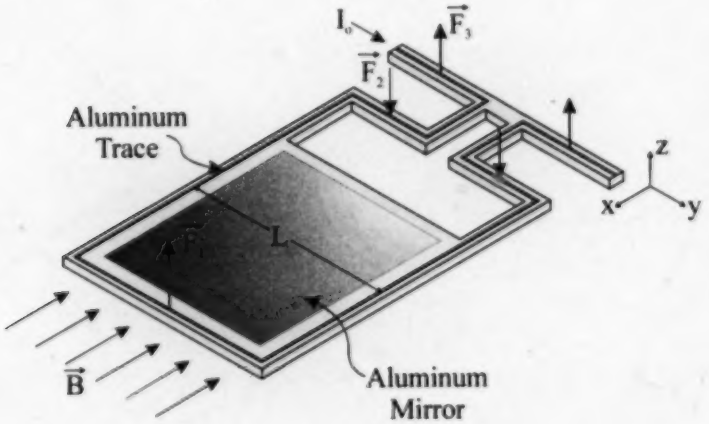

Figure 3.5: Magnetic actuation principle for micro-cantilever structures.

3.3 Device Modeling and Simulation

3.3.1 Static Deflection Modeling

The static behaviour of beams under concentrated point loads is a classical problem in structural mechanics. Research conducted at the University of Alberta on similar CMOS-fabricated structures has shown that due to the materials used in the manufacture of the devices, static deflections are small and therefore the device may be

characterized using small deflection beam theory [34].

Small deflection theory assumes that the vertical displacement, δ, of the free end of a cantilever beam is small in comparison to the length, L of the beam, or $\delta/L \ll 1$. For the simple, homogeneous cantilever beam shown in Figures 3.6(a), subjected to a single point load, the deflection, δ, and rotation, θ, of the free end are given by

$$\delta = \frac{PL^3}{3EI} \tag{3.3.1}$$

$$\theta = \frac{PL^2}{2EI} \tag{3.3.2}$$

respectively, where P is the concentrated point load, L is the length of the beam, E is Young's modulus of the material comprising the beam and I is the moment of inertia of the cross-section of the beam. Similarly, for a beam subject to a moment, M, at the free end, such as that illustrated in Figure 3.6(b), the deflection and rotation of the free end are given by

$$\delta = \frac{ML^2}{2EI} \tag{3.3.3}$$

$$\theta = \frac{ML}{EI} \tag{3.3.4}$$

For a structure that is composed of a number of cantilever beam segments, these equations must be utilized in conjunction with the superposition principle in order to determine the maximum tip deflection of the structure. The superposition principle

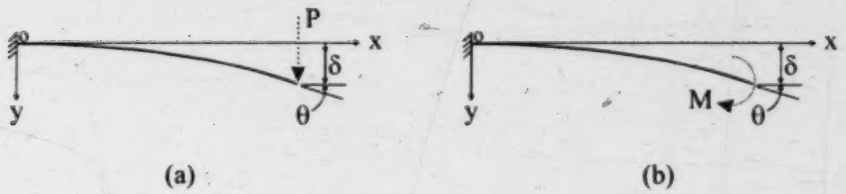

Figure 3.6: Static end deflection and rotation of a homogeneous cantilever beam under the influence of (a) a concentrated point load and (b) a moment.

discretizes the structure into its constitutive homogeneous members and performs simple beam analysis on these segmented portions. For the micro-cantilevers studied, for example, it is necessary to first divide the beam into three sections, as shown in Figure 3.7.

Initially, the beam is considered to be rigid at support A, as illustrated in Figure 3.7 (i) and the deflection at the free end (point B) is calculated. Sections BC and CD are then treated as individual cantilevers, as shown in Figure 3.7 (ii) and (iii), and the end deflections and rotations are calculated using the aforementioned equations.

The total end deflection of the beam is then given by

$$\delta_{Free-end} = \delta_D + \delta_B + \theta_B(L_B + L_c) + \delta_c + \theta_c(L_c) \qquad (3.3.5)$$

where the quantities δ_D, δ_B, δ_C, θ_B and θ_C are illustrated in Figure 3.8, and calculated using equations (3.3.1) through (3.3.4). Equation (3.3.5) does not take into account torsion acting on the members perpendicular to Sections AB and BC. The rotations due

to torsion of these members were calculated to be approximately 10^{-6} rads for a current of 30 mA and magnetic filed of 750 Gauss, and are therefore considered to be negligible.

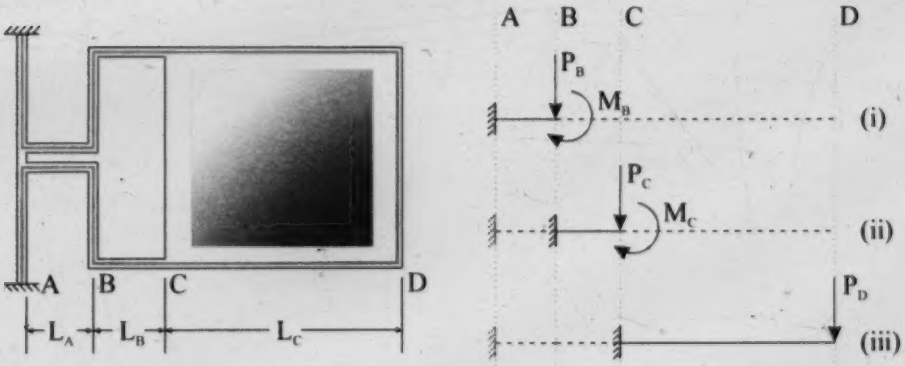

Figure 3.7: Discretized micro-cantilever utilized with superposition principle.

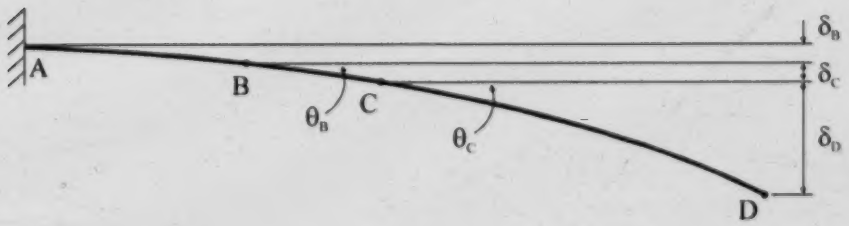

Figure 3.8: Schematic of the total deflection of a micro-cantilever device.

The moments of inertia for the individual beam segments shown in Figure 3.7 are calculated using the equivalent cross-section method. This method involves the conversion of the composite, layered rectangular cross sections into homogeneous T-

shaped cross sections. A detailed discussion of this method is contained in reference [10]. Using this method, the moments of inertia for sections AB and BC (for all three sizes of micro-cantilever) with and without the uppermost nitride layer, were calculated to be approximately 293.16 μm^4 and 123.48 μm^4 respectively. For section CD, the moments of inertia were obtained to be approximately 4528, 6918, and 9056 μm^4 for the small, medium and large cantilevers with the inclusion of the nitride layer respectively, and approximately 1850, 2826, and 3700 μm^4 respectively, when the nitride layer is excluded from the surface of the structures.

3.3.2 Dynamic Response Modeling

Many engineering problems require, at minimum, a rudimentary understanding of the mechanical dynamics or vibrations of structures. One such problem is centered on the determination of the deformation, w, of plates subject to time-dependent, transverse surface loads. The partial differential equation governing the forced vibration of plates is expressed by the classical equation [35, p. 158]

$$D\nabla^4 w + \rho h\ddot{w} + c\dot{w} = F(x,y,t) \tag{3.3.6}$$

Assuming the plate is subject to the homogeneous boundary conditions

$$w = 0 \quad \text{on the bounded region} \tag{3.3.7}$$

and the initial conditions

$$\begin{aligned} w(x,y,0) &= w_o(x,y) \\ \dot{w}(x,y,0) &= \dot{w}_o(x,y) \end{aligned} \tag{3.3.8}$$

where ρ is the mass/surface area of the structure, h is the plate thickness, c is the damping/surface area term, D is the flexural rigidity of the plate, and F is the applied load/surface area, the solution of Equation (3.3.6) can be characterized by the eigenfunction expansion [35, p. 158]

$$w(x,y,t) = \sum_{i=1}^{\infty} W^{(i)}(x,y) q_i(t) \tag{3.3.9}$$

where $W^{(i)}$ are the mode shapes that satisfy the boundary condition and $q_i(t)$ are functions to be determined. Essentially, this problem can only be solved through implementation of numerical methods; therefore, as an approximation to this complex problem we assume the motion of the harmonically excited micro-cantilever structures to follow that of a fundamental single degree-of-freedom system.

A mechanical system is considered to have one degree-of-freedom if the motion of the system can be fully expressed by a single value, such as vertical displacement alone, for any given time instance [36]. For a cantilever, the behaviour or motion of the structure may be related by the out-of-plane displacement of the free end; therefore, describing a micro-cantilever as a single degree-of-freedom system appears to be a sound initial assumption.

The motion of a fundamental, single degree-of-freedom system, as shown in Figure 3.9, is related by the differential equation

$$m\ddot{w} + c\dot{w} + kw = P_o \sin \omega t \tag{3.3.10}$$

with initial conditions

$$w(0) = w_o$$
$$\dot{w}(0) = \dot{w}_o$$

where m is the mass of the system, c is the coefficient of damping, k is the stiffness of the structure, and $P_o \sin \omega t$ is the external, alternating force acting on the system. The four terms in Equation (3.3.10) correspond to the inertia, damping, spring, and external forces respectively acting on the mass.

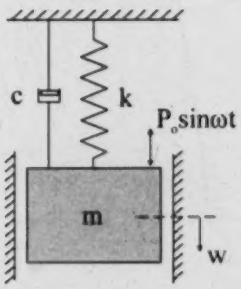

Figure 3.9: Schematic representation of a fundamental single degree-of-freedom system subject to forced vibrations with viscous damping.

The complete solution of Equation (3.3.10) consists of the sum of the homogeneous and particular solutions, both of which have been extensively derived in the theory of mechanical vibrations [36]. Following a sufficient time period and the

subsequent passing of the transient response, the solution to Equation (3.3.10) is given by

$$w_P = w_o \sin(\omega t - \varphi) \tag{3.3.11}$$

where

$$w_o = \frac{\frac{P_o}{k}}{\sqrt{\left(1-\frac{\omega^2}{\omega_n^2}\right)^2 + \left(2\xi \cdot \frac{\omega}{\omega_n}\right)^2}} \tag{3.3.12}$$

and

$$\tan\varphi = \frac{c\omega}{k - m\omega^2} \tag{3.3.13}$$

The above expressions for the amplitude, w_o, and the phase angle, φ, are in terms of two dimensionless parameters: ω/ω_n, the frequency ratio, and ξ, the damping ratio. The first parameter includes the natural frequency, ω_n, which is given as

$$\omega_n = \sqrt{k/m} \tag{3.3.14}$$

This quantity represents the frequency at which the structure will resonate if damping is negligible. In general, k is unknown; however, this quantity may be approximated by Hooke's Law, which states that the structural stiffness is the ratio of the applied load, F, to the resultant static deflection, δ, or

$$k = F/\delta \tag{3.3.15}$$

Similarly, the damping ratio, ξ, given by the equation

$$\xi = \frac{c}{2m\omega_n} \tag{3.3.16}$$

is also an unknown, that depends on the environment or fluid in which the devices are actuated. For small values of damping, this quantity may be determined through a technique referred to as the bandwidth method, which utilizes the following equation:

$$\xi = \frac{f_2 - f_1}{2f_{\max}} \tag{3.3.17}$$

In this equation, f_1 and f_2 are frequencies that bracket $f_{\max}$, the frequency at which the largest amplitude of vibration occurs, and correspond to amplitude values 0.707 times that of the maximum amplitude. f_1 and f_2, are also referred to as the half-power points of the response curve. The damping ratio is calculable only after experimental results have been obtained.

3.3.3 Piezoresistive Polysilicon Physical Sensors

Sensors enable MEMS designers and researchers to acquire information regarding device behaviour and interactions with surrounding environments. In general, sensors may be divided into two categories: chemical sensors – which are utilized to identify and classify gases and chemicals; and physical sensors – employed to quantify parameters such as displacement, velocity and acceleration. The latter class of sensors can be further divided into electrical, magnetic and optical sensing subcategories [32, p.223].

Of these three sensor subcategories, a form of the electrical sensing method was incorporated into the devices investigated for this thesis work. One example of electrical sensing involves integration of piezoresistive material into the microstructure. The resistivity of the piezoresistive material is a function of the internal stress acting on the sensor (induced by deflection, for example) and can therefore be used to obtain information to characterize the motion of structures when actuated.

This piezoresistive effect was first documented for germanium and silicon by researchers at the Bell Telephone Laboratories in 1953 [37], and is presently employed as the primary sensing means in several MEMS devices [38]-[39]. For the micro-cantilever devices studied in this thesis, polysilicon material was positioned at the base of the support arms. By passing a small current through the polysilicon and measuring the resulting voltage (during actuation of the structures), the change in resistivity of the material can be determined. This change in resistivity is then related to the motion of the actuated cantilevers.

For this thesis, the static tip deflection and amplitude of vibration of the micro-cantilevers will be related to the output of the polysilicon piezoresistive elements. These derivations, presented in this section, will serve as precursors to developing expressions that will couple the effect of cantilever motion (determined from piezoresistive response) on the production or modification of fluid flow. These latter expressions dealing with the fluid aspect will be left to future work.

The change in resistivity of a piezoresistive material due to an externally applied stress is given by

$$\frac{\delta\rho_i}{\rho_0} = \Pi_{ij} X_j \qquad (i, j = 1, 2, \ldots 6) \qquad (3.3.18)$$

where $\delta\rho_i$ denotes the change in resistivity, ρ_o is the scalar resistivity, Π_{ij} is the piezoresistivity of the material, and X_j is the mechanical stress acting on the sensing element [40]. Conversely, Equation (3.3.18) may also be expressed in terms of the strain, ε_j, based on strains defined by the strain-displacement relation from *small* displacement theory, as

$$\frac{\delta\rho_i}{\rho_0} = GF_{ij}\,\varepsilon_j \qquad (i, j = 1, 2, \ldots 6) \qquad (3.3.19)$$

where GF_{ij} represents the dimensionless elastoresistance of the piezoresistive material [37]. GF_{ij} is then related to the piezoresistivity via an elastic stiffness tensor, c_{kj} by

$$GF_{ij} = \Pi_{ik}\, c_{kj} \qquad (i, j, k = 1, 2, \ldots 6) \qquad (3.3.20)$$

The internal symmetry of the piezoresistivity tensor and the structural properties of polysilicon are such that the piezoresistivity tensor can be fully defined by two coefficients, Π_{11} and Π_{12}, the longitudinal and transverse piezoresistive coefficients respectively. Furthermore, due to actuation of the device out of the plane of the micro-cantilever surface, transverse stress on the structure will be approximately zero; therefore substitution of Equations (3.3.19) and (3.3.20) into (3.3.18) and applying the reductions

of the piezoresistivity tensor, yields

$$\frac{\Delta R}{R} \approx \frac{\Delta \rho}{\rho} = (GF)\,\varepsilon \tag{3.3.21}$$

or

$$\Delta V = I_o \Delta R = I_o (GF)\,\varepsilon R \tag{3.3.22}$$

where ΔV is the change in voltage of the piezoresistive elements due to deformation, GF is a quantity known as the gage factor and I_o is the constant driving current passed through the piezoresistors.

The gage factor, GF, for polysilicon and other piezoresistive materials has been shown to be dependent on both the doping concentration and annealing used to fabricate the sensor [41]. Typical values for LPCVD-deposited polysilicon range from 5 – 25; however, for the Mitel 1.5 μm CMOS process a gage factor of 25 has been reported [42].

The surface strain along a beam is given by

$$\varepsilon = \frac{(t/2)}{r} \tag{3.3.23}$$

where t is thickness of the beam and r is the radius of curvature of the beam. The Bernoulli-Euler Law states that

$$\frac{1}{r} = \frac{M}{EI} = \frac{F(L-x)}{EI} \tag{3.3.24}$$

where M is the bending moment, and E and I are the Young's modulus and the moment of inertia of the beam, respectively. As shown in Figure 3.10, F, L, and x denote the externally applied force, the length of the structure, and the midpoint of the length of the piezoresistors, respectively. Therefore, direct substitution of Equations (3.3.23) and (3.3.24) into Equation (3.3.22), and manipulation of the resultant equation gives

$$F = \frac{2\Delta VEI}{I_o(GF)(L-x)R} \tag{3.3.25}$$

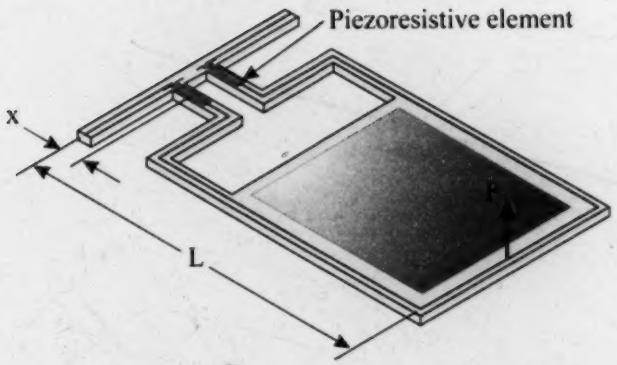

Figure 3.10: Schematic relating physical quantities related in Equation (3.3.25).

For the case of a static loading, substituting Hooke's law (Equation (3.3.15)) into Equation (3.3.25) and subsequent rearrangement of the resulting equation yields,

$$\delta = \frac{2\Delta VEI}{kI_o(GF)(L-x)R} \tag{3.3.26}$$

where δ is the deflection of the tips of the piezoresistors. Similarly, for dynamic loading of the micro-cantilever devices, substitution of Equation (3.3.12) into Equation (3.3.25) results in the following:

$$w_o = \frac{2\Delta VEI}{kI_o(GF)(L-x)R\sqrt{\left(\left(1-\frac{\omega^2}{\omega_n^2}\right)^2+\left(2\xi\cdot\frac{\omega}{\omega_n}\right)^2\right)}} \tag{3.3.27}$$

where w_o represents the amplitude of vibration of the micro-cantilever.

It is anticipated that Equations (3.3.26) and (3.3.27) can be utilized to determine the tip deflections, both static and dynamic, respectively, of the micro-cantilever structures from the response of the piezoresistive elements. In knowing the relationship between piezoresistive response and amplitude of vibration, Equation (3.3.27) may be expounded upon to illustrate a relationship between piezoresistive response and fluid flow. The results from Equations (3.3.26) and (3.3.27) will be compared with both FEM models and experimental results in Chapter 5.

3.3.4 Finite Element Simulation

Many problems in engineering are often extremely complex and can therefore not readily be solved using conventional analytical methods. With the advent of high-speed computers, however, the emphasis in engineering analysis was, and continues to be, shifted from analytical analyses to numerical, finite element analyses. Finite element analysis (FEA), or the finite element method (FEM), was originally pioneered in the area

of structural analysis and was later introduced into the aerospace industry in the 1950's and 60's [43]. Today, FEA is widely used throughout most areas of engineering and is utilized to solve structural, thermal, fluid, and coupled-field analyses.

FEA involves the discretization of a physical system, such as a solid or fluid, into subsections or elements. Through the application of loads and constraints to the system, algebraic equations are derived that relate the behaviour of each element to its surrounding elements. The resulting set of simultaneous equations is then solved to determine the overall behaviour of the modeled system. In general, FEA involves three distinct steps:

- creating the model,
- applying loads and obtaining the solution, and
- reviewing the results.

In the first step, the model geometry is input, the element types and constants (such as thickness, material direction angles, and material properties of the composite layers) are defined, and the resulting model is sectioned or meshed. For the devices modeled in this work, the commercial FEA software package ANSYS® Version 5.3 was utilized. From this package, element type SOLID46 was incorporated to model the micro-cantilever structures. This element, shown in Figure 3.11, is a three-dimensional, layered, 8-noded structural solid designed to model layered shells or solids. A detailed discussion of SOLID46 is contained in the ANSYS Elements Reference Manual [44]. For the bulk of the cantilever structures, including the platform and a portion of the support arms, a four-layered element was generated, whereas for areas of the structures containing piezoresistive elements, such as at the base of the support arms, a six-layered

configuration of the same element type was created. The thickness of the uppermost (silicon nitride) layer of these elements was varied from 0, 50, and 100% of the manufacturer's specified thickness of 0.5 μm. Cross-sections of both element configurations are shown in Figure 3.12.

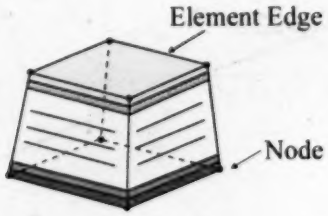

Figure 3.11: Schematic of the Three-Dimensional structural solid SOLID46.

Essentially, in using the four-layered element, the assumption is made that the constituent layers of the platform and support arms are uniform throughout the width and breadth of the cantilever; however, as was shown in Figure 3.3 the aluminum layer is non-uniformly distributed throughout the cantilever structures. Enveloping both the aluminum mirror and trace is silicon dioxide, which has comparable material properties to those of aluminum (Table 3.2); therefore use of element layer configurations such as those shown in Figure 3.12 is thought to be valid.

Following the definition of the system geometry and the element parameters, the system is discretized or meshed. For the micro-cantilever models created, the meshes were comprised of hexahedral (brick) volume elements and the number of elements along structural edges was explicitly (manually) inputted. Along the widths and lengths of the support arms and platform, for instance, the number of element divisions was specified

by the program user. Initial meshes were crude, as the number of element divisions along an edge was small. The meshes were subsequently refined in areas where large amounts of bending or translation were anticipated to occur, such as in the region of the folded support arms. Mesh refinement is required in order to determine whether the results for a solution have converged.

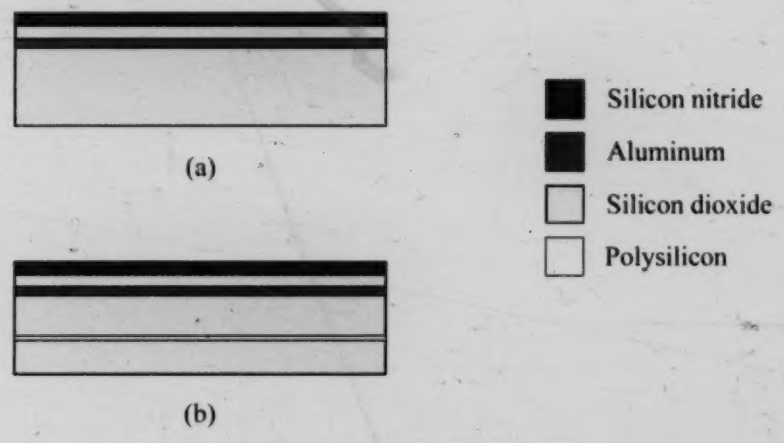

Figure 3.12: Schematic of the cross section of the two layered element configurations used in the micro-cantilever simulation: (a) four layered and (b) six layered elements.

Convergence of results is achieved when further refinement of the mesh no longer produces appreciable changes in output. In general, coarse meshes will produce values that greatly differ from analytical output. A coarsely meshed fixed-end cantilever beam, for instance, subject to a point load at the free end may produce output that varies appreciably from the output predicted by theory (Equation 3.3.1). Mesh refinement is conducted particularly in regions where large stress or strain gradients are expected. For

the special case of a homogeneous cantilever, for instance, subjected to a point load at the free end, ANSYS results following final mesh refinement agree well with analytical results.

The next step in conducting the finite element analysis involves the definition and application of loads onto the model. The analysis type (static, modal, or harmonic, for example) to be conducted is chosen based on the loading conditions and the response that is to be calculated. The accompanying loads for static, harmonic, or modal analyses may be defined as constraints, forces, surface loads, body loads, inertia loads, and coupled-field loads. For the micro-cantilever models generated, only constraints and forces were applied. The models were constrained at the support arm/micro-channel interface, and the Lorentz forces were applied along the location of the centerline of the aluminum trace. A complete ANSYS model, meshed, constrained and with applied loads, of the small micro-cantilever device is shown in Figure 3.13.

For the purpose of this work, both static and dynamic analyses were conducted. A sample command file created to compile data concerning these analyses is contained in the Appendix. The static analysis of the structures was conducted by applying currents varying from 1 to 40 mA and computing the corresponding Lorentz forces; harmonic analysis was performed by specifying a value for the Lorentz force and the frequency range over which to determine the response of the device.

Following the analysis definition stage, complete models are solved for static, modal or harmonic output and the output carefully reviewed to determine the validity of the results. At this phase of analysis, results are also checked for convergence.

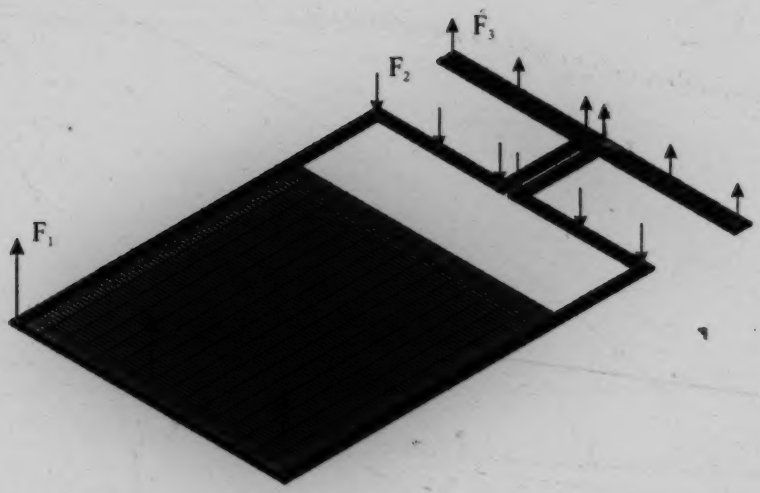

Figure 3.13: ANSYS model of a small cantilever device under the influence of simulated Lorentz forces.

Chapter 4

EXPERIMENTAL DESIGN AND RESULTS

4.1 Introduction

Experimental results were obtained for the static deflections in air, and the dynamic behaviour, in fluid media, of the micro-cantilever devices. Air, distilled water, and isopropyl alcohol (IPA) were employed as individual test fluids in order to determine the effects of fluid viscosity on the ability of the structures to resonate. These fluids were utilized due to availability and non-toxicity. This chapter outlines the experimental methods utilized to obtain the required data as well as the results obtained from implementing these methods.

4.2 Experimental Setup

4.2.1 Static and Dynamic Response Experimental Method

The experimental layouts utilized for the determination of both the static and dynamic responses of the micro-cantilevers in various media are shown in Figures 4.1, 4.2 and 4.3. Initial preparation of the devices prior to experimentation involved the packaging and bonding of a single CMOS-fabricated die onto a 40 pin Dual Inline Package (DIP). Norland Optical No. 81 UV-curable adhesive was then deposited (in sufficient quantity to fully cover the bonding wires) into the space between the micro-cantilevers and package walls. This polymer dam/well was constructed to isolate and protect the electrical connections on both the die and the package from the test fluids, as

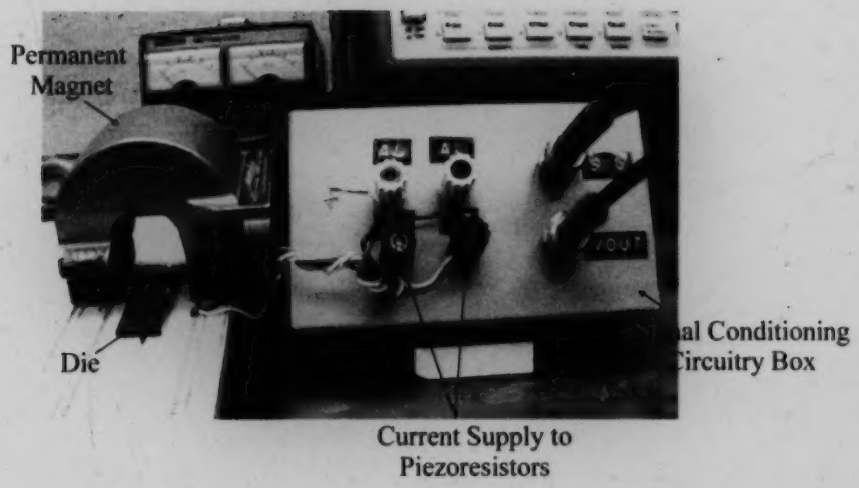

Figure 4.1: Experimental layout of device and permanent magnet.

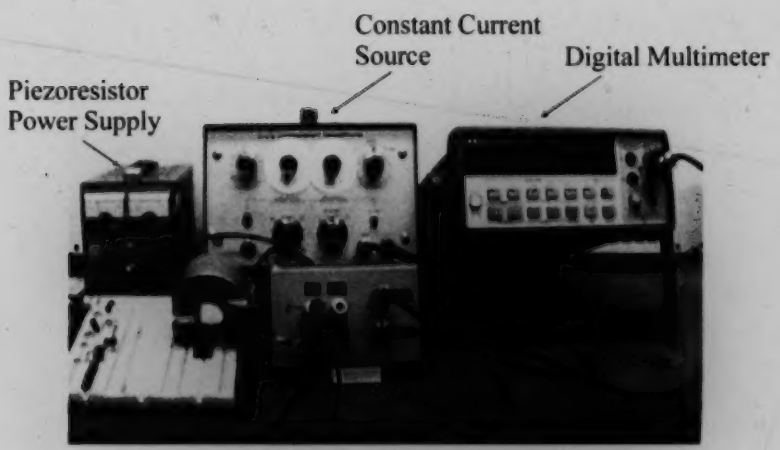

Figure 4.2: Experimental layout for determination of static response of micro-cantilever devices.

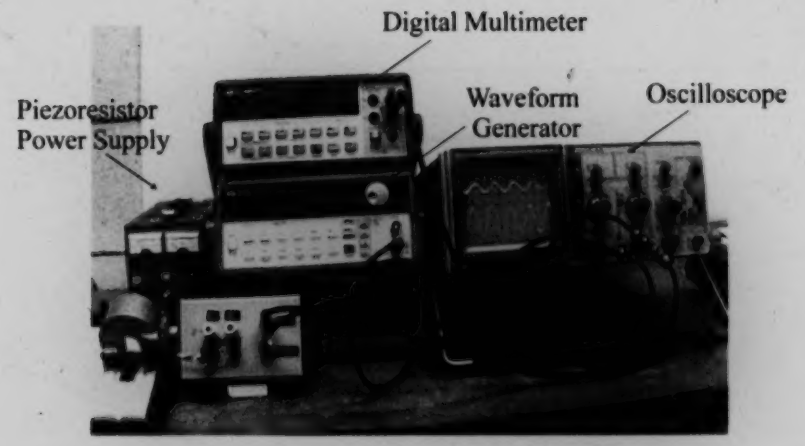

Figure 4.3: Experimental layout for determination of dynamic response of micro-cantilever devices.

well as to contain the test fluids within the vicinity of the cantilever array.

An assembly diagram and a cross-section of the fully prepared test device are shown in Figures 4.4(a) and (b), respectively. Of the fluids tested, the distilled water and IPA are prone to rapid evaporation, therefore an acrylic tube, approximately 3.5 mm in diameter and 2 mm in height, was positioned over the die. The tube was filled with the test fluid using a syringe equipped with a 250 μm inner diameter syringe needle, and the mouth of the tube capped with a 0.2 mm thick microscope cover glass.

Following etching using XeF_2, as described in Chapter 2, the above configuration was positioned onto a circuit board. A horseshoe magnet mounted above the surface of the breadboard, as shown in Figure 4.1, provided an external magnetic field of approximately 750 Gauss. The magnitude of the magnetic field was measured using a RFL Inc. model 1890 gaussmeter. The position of the magnet with respect to the packaged device was carefully noted over the course of experimentation, so as to achieve

relatively similar magnetic fields in the vicinity of the micro-cantilevers during the course of testing in different fluids.

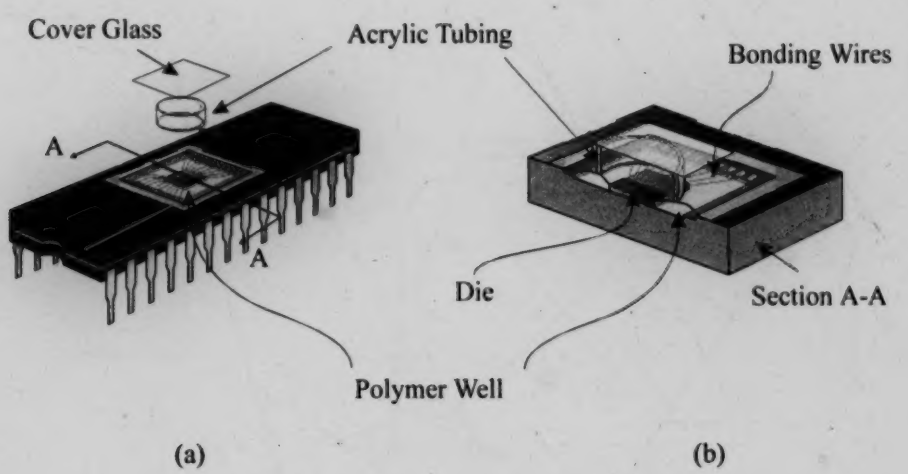

Figure 4.4: (a) Assembly diagram and (b) illustration of the cross section A-A of fully pre-experimentation prepared die.

The experimental setup employed for the static testing of the micro-cantilever devices is shown in Figure 4.2. The actuation current required to produce a Lorentz force was supplied by a Keithley Instruments 225 current source; data was acquired manually for currents ranging from 1 to 30 mA for the experimental layout both with and without the external static magnetic field.

For dynamic testing, a Hewlett Packard 33120A waveform generator and Hewlett Packard 34401A digital multimeter were used to create sinusoidal input signals and to monitor the response of the piezoresistors, respectively. This experimental setup is shown in Figure 4.3. To facilitate data collection, a computer-based data acquisition

system, which had been previously devised in the Micromachining Applications and Development Laboratory, was utilized [11]. The data acquisition system consisted primarily of a middle-language source code created so as to control and allow user interface with the signal generator and digital multimeter. The design principles and examples of the source code are provided in reference [11]. A resistance of 270 Ω was placed in series with the devices, so as to compensate for heating of the current path in the cantilever structures, which in turn affects the resistance of the trace and produces a decrease in the actuation current. By incorporating the 270 Ω resistor in series, the actuation current will remain relatively constant throughout experimentation.

Through use of the data acquisition system, the system user specified the starting and ending frequencies for actuation of the devices, as well as the desired frequency step size within the specified range. At each frequency step, 10 data readings of the digital multimeter output were taken by the data acquisition system and then averaged in order to reduce noise in the measurement of piezoresistive response of the cantilevers.

The signal conditioning circuitry used throughout the course of both the static and dynamic response characterization had also been previously employed for other research efforts at the University of Alberta [11], [27]. A constant DC current of 500 μA was supplied to the piezoresistive elements in series by the implementation of a Wilson current mirror; this device allows for the provision of constant current to the piezoresistive elements independent of the resistive load on the elements.

4.2.2 Optical Detection Measurements

The deflections, both static and dynamic, of the cantilever platforms were also

determined by implementing an optical method of deflection measurement as shown in Figure 4.5(a). The 40 pin DIP containing the devices was placed into a Zero Insertion Force (ZIF) socket, which was in turn mounted into an aluminum magnet holder, as shown in Figure 4.5(b). Attaching two ceramic magnets on either side of the non-magnetic holder provided the required external magnetic field. The resultant magnetic field at the mid point of the two magnets was measured to be approximately 550 Gauss. The horseshoe magnet was not utilized, as it would be necessary to mount the magnet above the chip and this positioning would interfere with the laser beam.

A Thorlabs Model S1021 laser diode was used as the light source during optical measurements. The beam from the laser diode was first focused onto the mirrored surface of the cantilever and then reflected onto a flat screen. The positions of the reflected beam on the screen before and after static actuation were used to determine the angle of deflection, θ, of the cantilever device, as indicated in Figure 4.6. Similarly, during dynamic actuation of the devices, the reflected laser beam spreads out into a fan of light, the width of which was measured and related to the angle of deflection of the oscillating cantilever. In knowing the angle of rotation and by applying trigonometric relations, the approximate displacement of the cantilever tip is calculated.

For static deflections, driving currents of 1 to 30 mA were applied to the test configuration both with and without the presence of the ceramic magnets. The dynamic response of the devices was monitored by inputting sinusoidal waveforms at frequencies bracketing the resonant frequency determined from the experimental method as explained in the previous section.

Optical measurements were conducted solely in air, due to difficulties

encountered with obtaining a well-defined reflected beam while the micro-cantilevers were immersed in liquid. Obtaining data using a poorly defined beam would introduce large errors in data analysis.

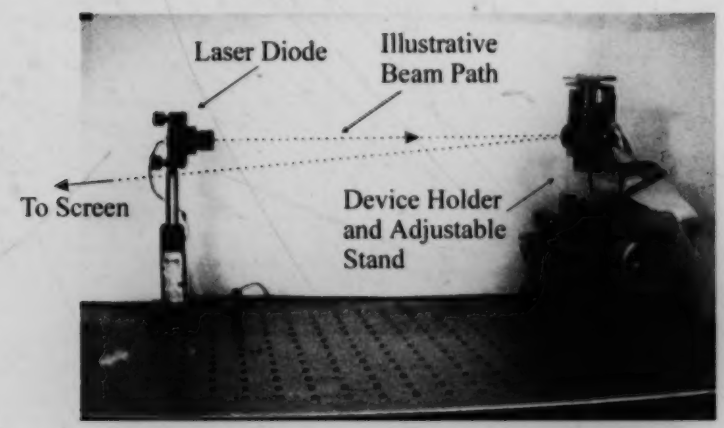

(a)

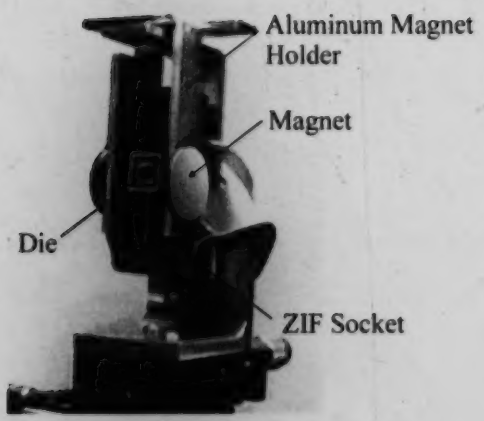

(b)

Figure 4.5: (a) Experimental layout and (b) external magnet orientations used in optical method of deflection measurement.

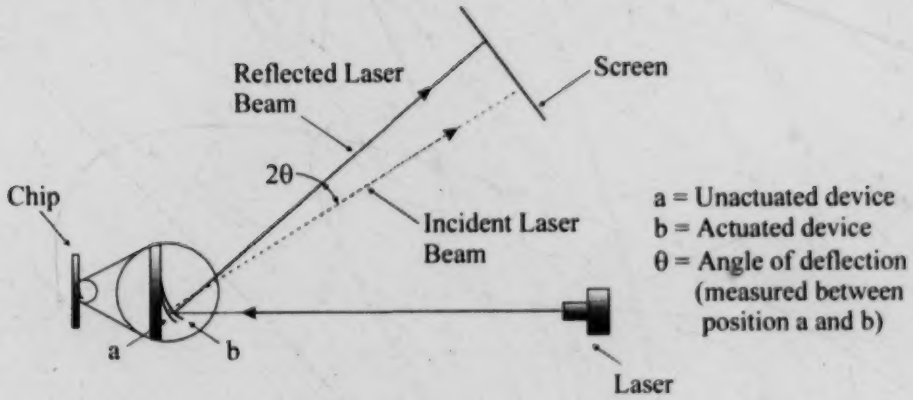

Figure 4.6: Correlation between reflected beam and micro-cantilever deflection.

4.3 Experimental Results and Analysis

Using the experimental techniques outlined in Section 4.2, results were obtained for the three sizes of cantilevers while submerged in air, distilled water and IPA. The results for the three microstructures are presented in the following sections.

4.3.1 Static Deflection

4.3.1.1 Piezoresistive Response Data

The three cantilevers were first tested to determine static deflection in air. The structures were tested at atmospheric conditions of approximately 93 kPa, by varying the direct current from 1 to 30 mA_{dc}. Three tests were conducted for each cantilever. The first investigation involved the inclusion of the external static field and applying an actuation current along the aluminum trace in one direction. The polarity of the current was then reversed and the tests repeated.

The last test involved removal of the external magnetic field and repetition of the two previous tests. Figures 4.7 and 4.8 show the results that were obtained from monitoring the piezoresistive response during the course of actuation for the small and medium cantilevers, respectively. The large cantilever showed no piezoresistive response due to high residual stress and therefore no data will be presented on this particular micro-cantilever; an explanation regarding the lack of piezoresistive response is provided in Chapter 5. All plots have been fitted using straight lines between data points; errors less than $\pm$ 0.2 mV were calculated, for Figures 4.7 and 4.8, by determining the standard deviation of the seven data readings recorded at each actuation current.

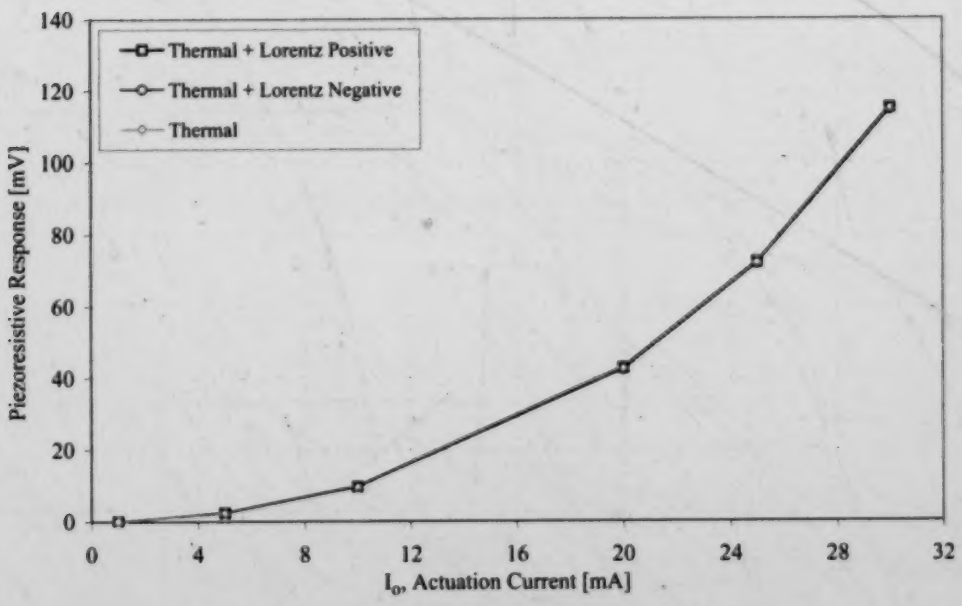

Figure 4.7: Static deflection piezoresistive response for the small micro-cantilever in air and at constant actuating current.

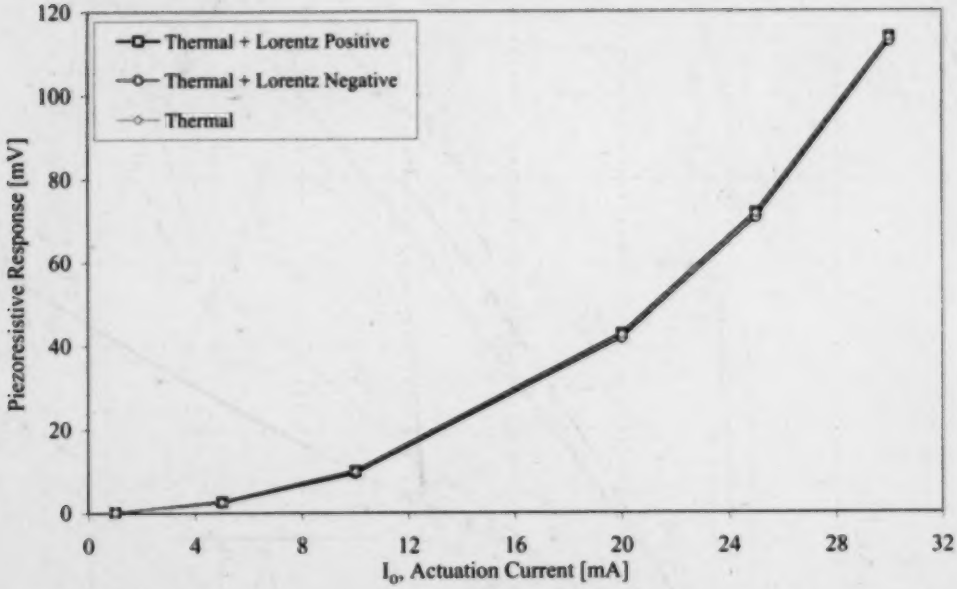

Figure 4.8: Static deflection piezoresistive response for the medium micro-cantilever in air and at constant actuating current.

In Figures 4.7 and 4.8, and the remainder of figures in this thesis pertaining to static analysis, the terms "Lorentz Positive" and Lorentz Negative" denote the Lorentz force at the tip of the structure to be directed away from the substrate and towards the substrate, respectively. The term "Thermal" is used to describe data acquired with the passage of current and without the presence of the external magnetic field. This latter designation was chosen based on prior research [10], which has indicated that electro-thermal actuation plays a large role in the static actuation of MEMS devices. Resistive or Joule heating of the structures and subsequent differential thermal expansion of the structural layers result in deflection of the micro-cantilever. Figure 4.9 illustrates the effect of electro-thermal actuation alone on both the small and medium devices. Unlike the linear trend hypothesized (in Section 3.3.1) for the mechanical deflection of the

micro-cantilevers, the thermal deflection exhibits a non-linear polynomial curve. The curves, given by best-fit approximations (both with correlation factors of 1) as shown in Figure 4.9, indicate that a small difference (approximately 1.28 mV) exists between the piezoresistive response of the small and medium cantilevers actuated at 30 mA. For both devices, the thermal effect produces a deflection of the device downward or towards the substrate, thereby effectively straightening the microstructures.

In order to eliminate these thermal effects, the thermal deflections illustrated in Figure 4.9 have been subtracted from their corresponding curves shown in Figures 4.7 and 4.8. The resulting plots, indicating the deflection of the devices due to Lorentz forces are shown in Figures 4.10 and 4.11 for the small and medium devices, respectively.

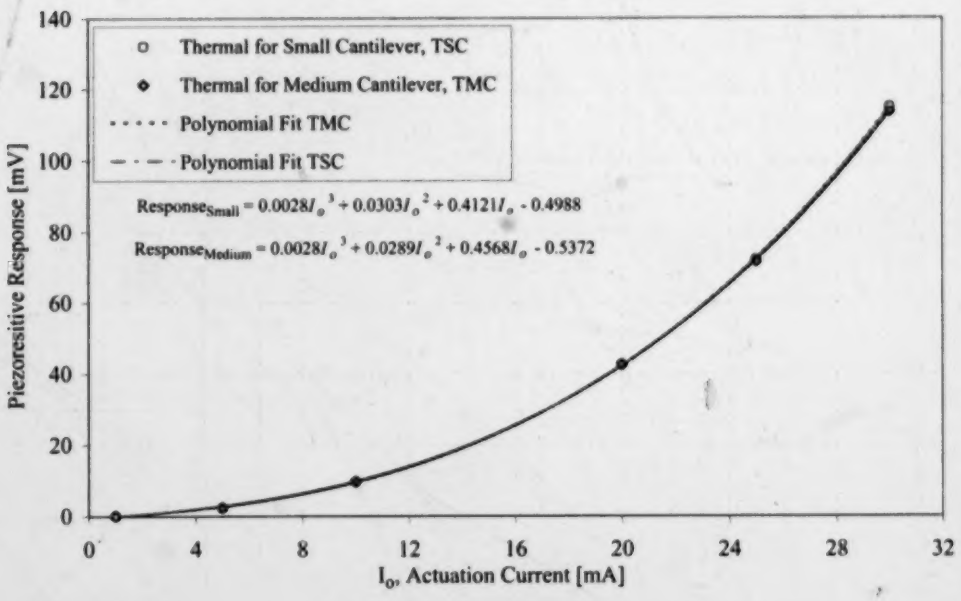

Figure 4.9: Thermal effect for the small and medium cantilevers in air.

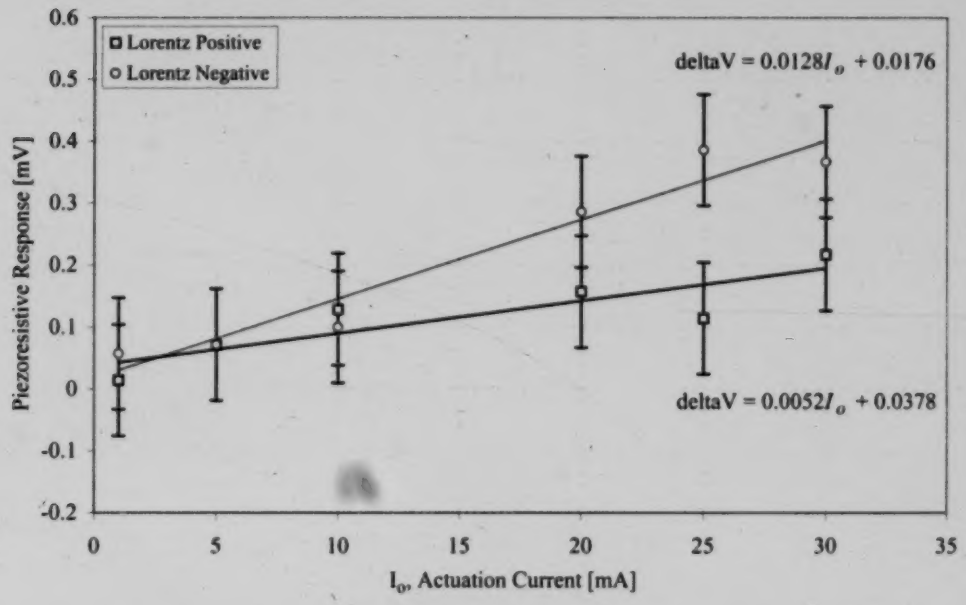

Figure 4.10: Static piezoresistive response for the small cantilever in air.

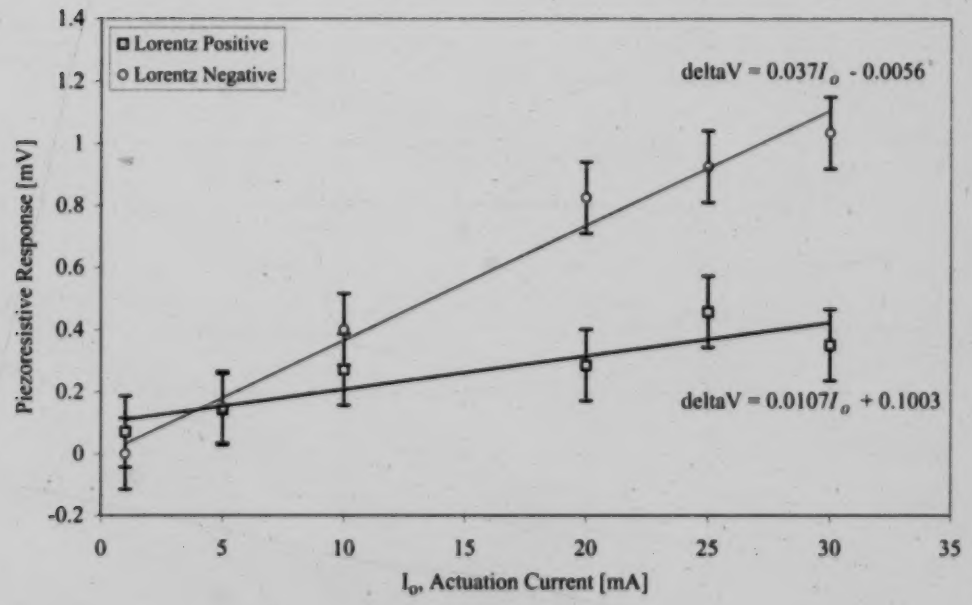

Figure 4.11: Static piezoresistive response for the medium cantilever in air.

The results presented in the preceding figures indicate that the static response of the two structures is well predicted by a linear relationship between actuation current (and therefore Lorentz force) and piezoresistive response. Such a relationship was developed in Section 3.3.3 of this thesis, the results of which will be compared with experimental data in the following chapter.

Errors shown in both Figures 4.10 and 4.11 are a result of fluctuations in the piezoresistive response during testing. The output of the piezoresistors was allowed to equilibrate for approximately two minutes following actuation; however, slight fluctuations in piezoresistive response were still observed following this two minute time period. Seven data readings were taken at each actuation current; the error bars signify the standard deviation of the results.

4.3.1.2 Optical Detection Data

The above series of tests was repeated using the optical detection measuring method outlined in Section 4.2.2. Figures 4.12 and 4.13 show the results that were obtained, as described in Section 4.2.2, from optical data for the small and medium cantilevers, respectively. The data points are connected via straight lines. Figures 4.14 and 4.15 illustrate the deflections due to the effect of solely Lorentz forces for both cantilevers.

The linear trends illustrated in Figures 4.14 and 4.15 show that small deflections occur under static actuation, and therefore simple beam theory is appropriate in determining the behaviour of the devices. This theory, however, does not explain the occurrence of two linear equations, a result of changing the direction of the actuating

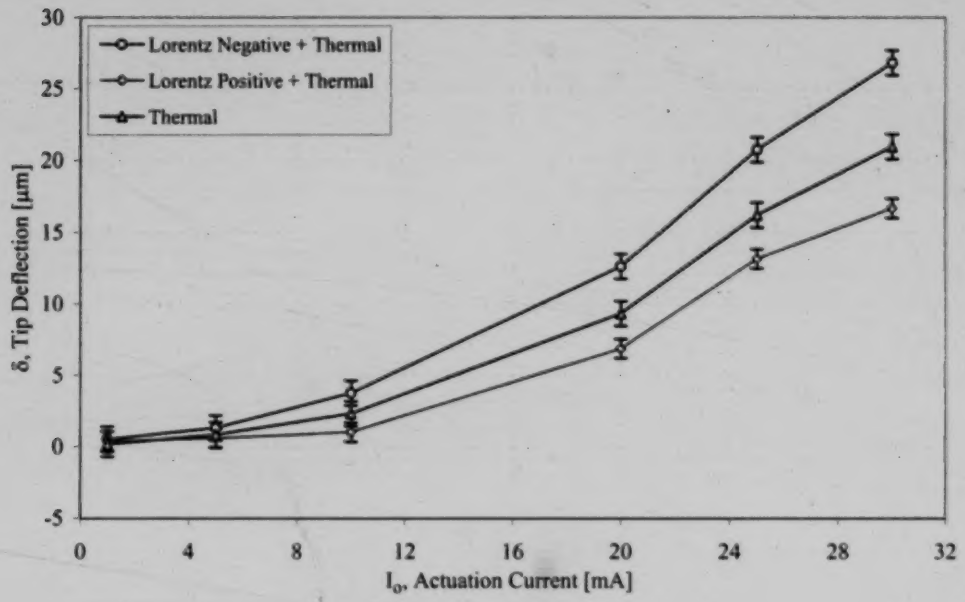

Figure 4.12: Static deflection of the small cantilever, measured using optical method.

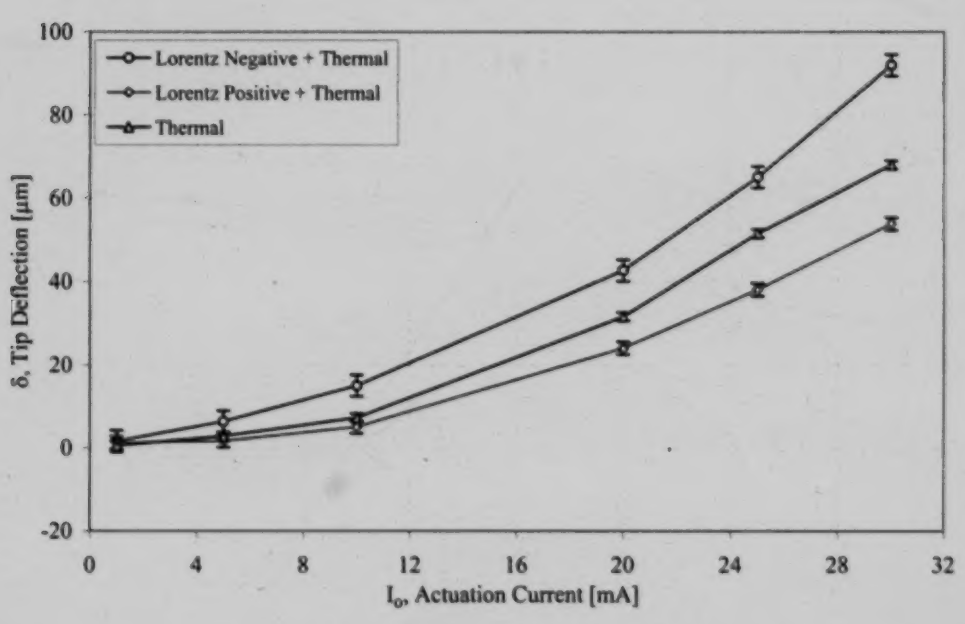

Figure 4.13: Static deflection of the medium cantilever, measured using optical method.

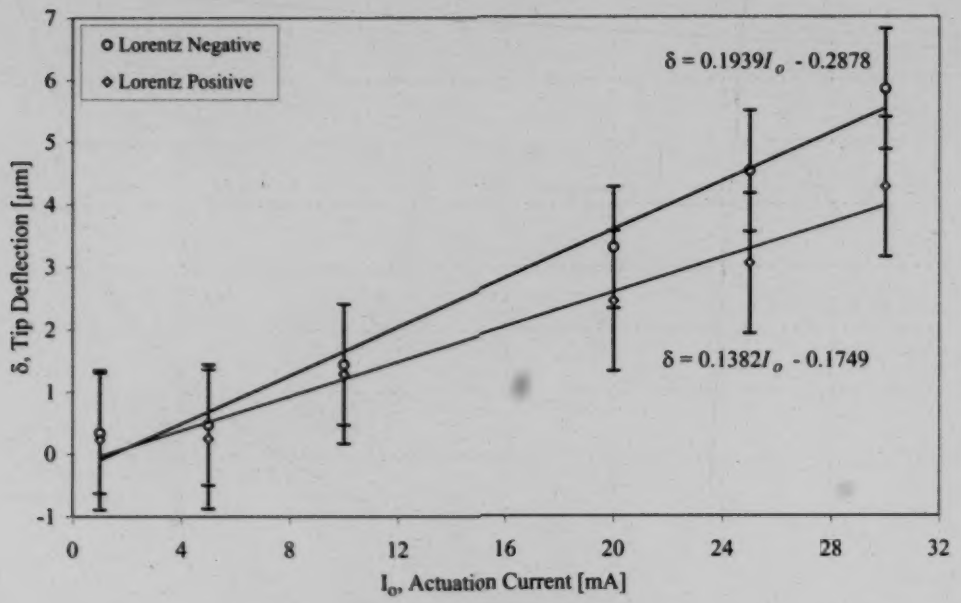

Figure 4.14: Static deflection of the small cantilever due solely to Lorentz forces.

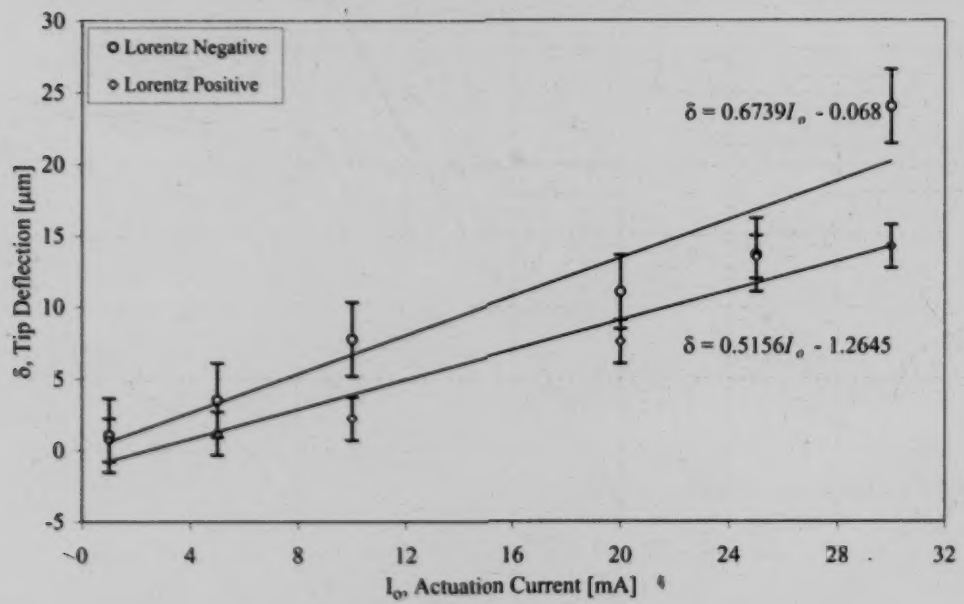

Figure 4.15: Static deflection of the medium cantilever due solely to Lorentz forces.

current along the aluminum trace. The two expressions are a result of residual stress acting on the structures, which hinders the deflection of the devices in one direction and facilitates in the other. This hypothesis will be further discussed in Chapter 5.

4.3.2 Dynamic Response

4.3.2.1 Piezoresistive Response Data

Dynamic response data was taken for the small and medium micro-cantilevers as described in Section 4.2.1. As with static testing, the large cantilever did not transmit a detectable response during actuation. This occurrence will be explained in Chapter 5. The three micro-cantilevers were initially tested in the same atmospheric conditions as those employed throughout the static testing of the micro-cantilevers. The data acquisition system was utilized to acquire data, at frequency intervals of 20 Hz, within a frequency interval bracketing the resonant frequency. The resonant curves, shown in Figures 4.16 and 4.17, respectively, for the small and medium cantilevers, were produced with alternating currents of 1, 5, 10, 20, 30, and 40 mA_{pp} and a static, magnetic field of approximately 750 Gauss. The resonant frequencies for the small and medium structures were measured to be approximately 2663 and 1132 Hz, respectively, in air. Piezoresistive response data ranging from 16.8 to 555.1 mVrms for the small cantilever and 24.5 to 703.7 mVrms for the medium cantilever was collected over the actuation range of 1 to 40 mA_{pp}. It is not known why the medium cantilever does not exhibit a smooth, classical resonance curve. Two small peaks, occurring at 1340 Hz for the small cantilever and 570 Hz for the medium cantilever, are also present in both resonance curves. It is believed that these maxima correspond to an extraneous mode of vibration.

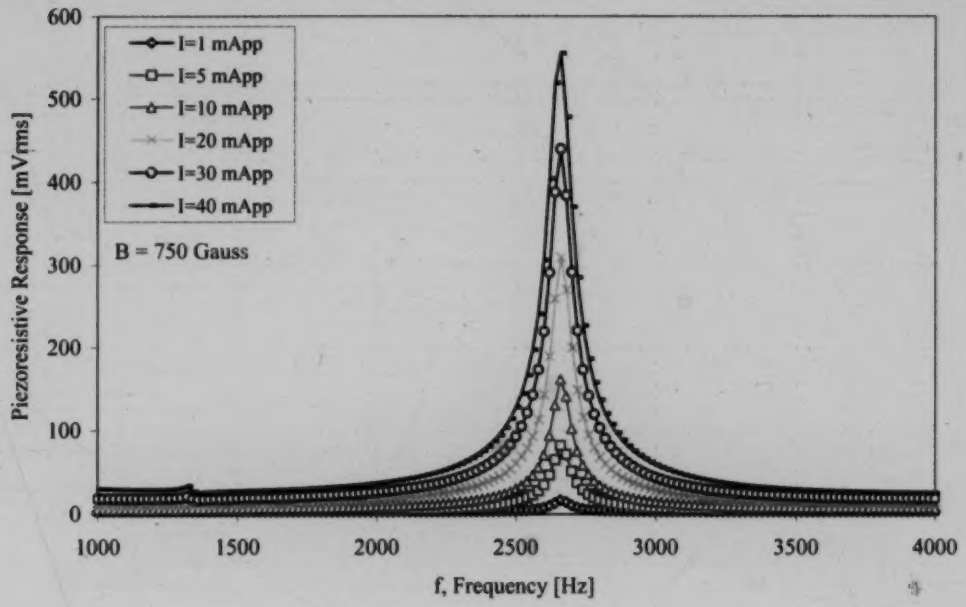

Figure 4.16: Piezoresistive response of small cantilever dynamically actuated in air.

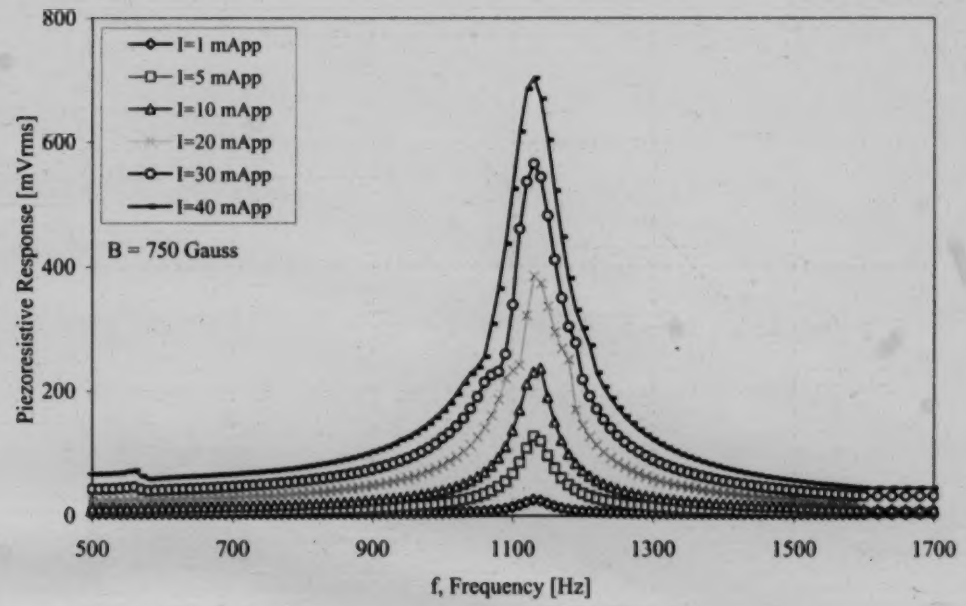

Figure 4.17: Piezoresistive response of medium cantilever dynamically actuated in air.

Figure 4.18 illustrates that as the Lorentz force is increased, the increasing piezoresistive response does not follow a linear relationship, as predicted by Equation (3.3.25). It is assumed that the deviation from linearity is due to heating of the piezoresistors, which will increase the strain on the elements. The effect of piezoresistor heating during actuation was not accounted for in Equation (3.3.25).

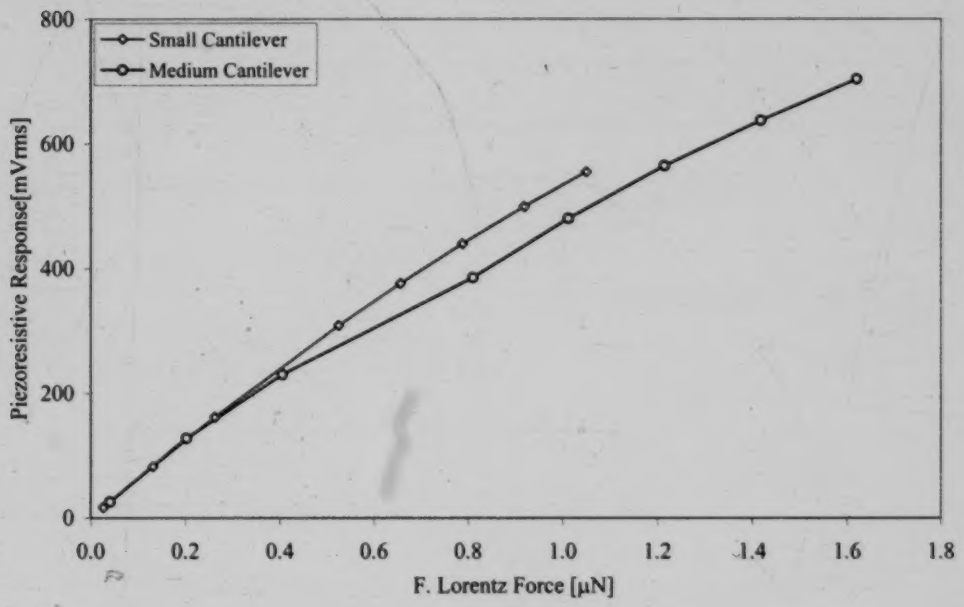

Figure 4.18: Maximum piezoresistive response for given value of Lorentz force.

Dynamic testing was then repeated in isopropyl alcohol and distilled water for actuation currents ranging from 20 to 40 mA_{pp}. Both fluids were at room temperature, approximately 25°C, throughout the course of experimentation. The resultant piezoresistive response versus frequency data is illustrated in Figures 4.19 and 4.20 for the small cantilever and Figures 4.21 and 4.22 for the medium cantilever.

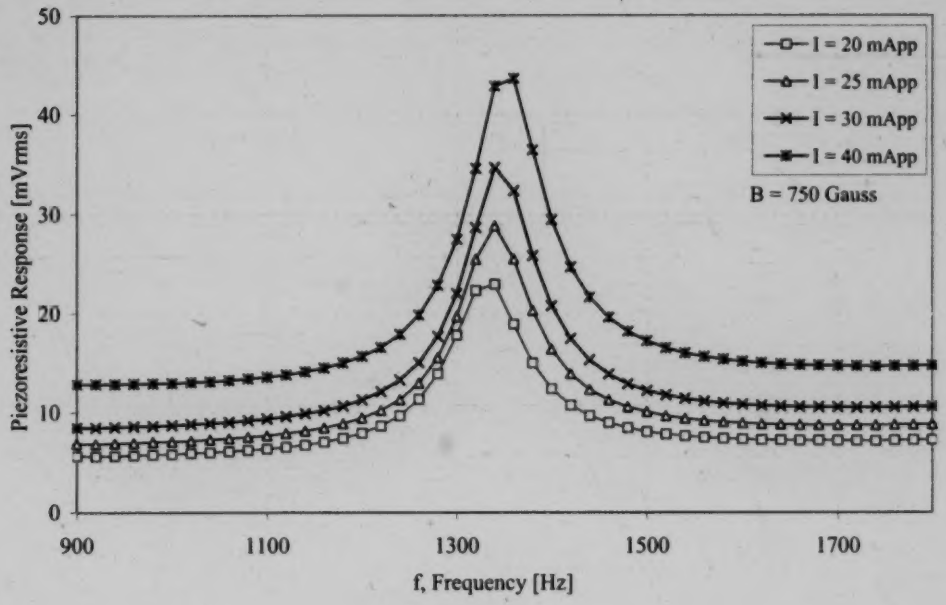

Figure 4.19: Piezoresistive response of small cantilever dynamically actuated in distilled water.

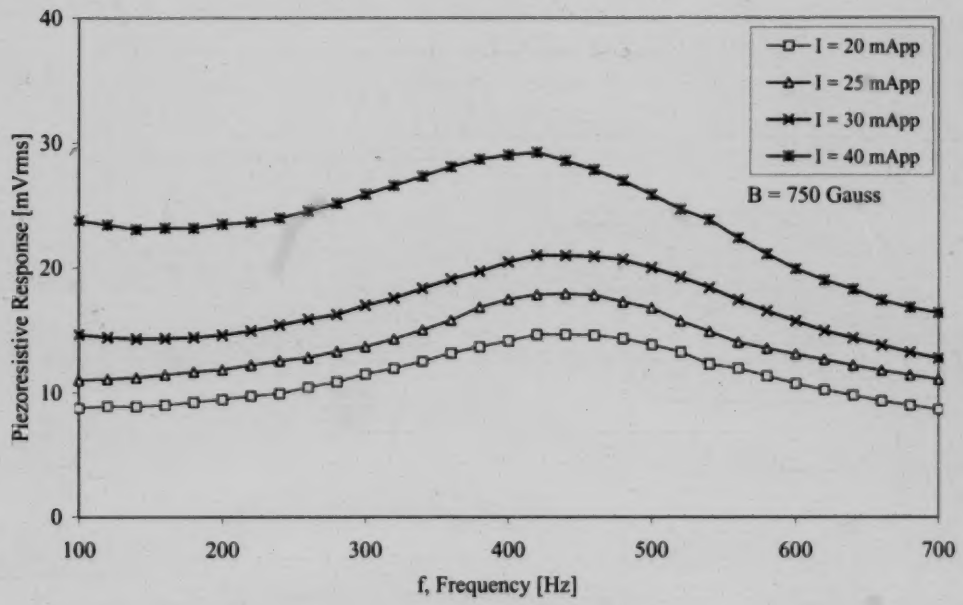

Figure 4.20: Piezoresistive response of small cantilever dynamically actuated in IPA.

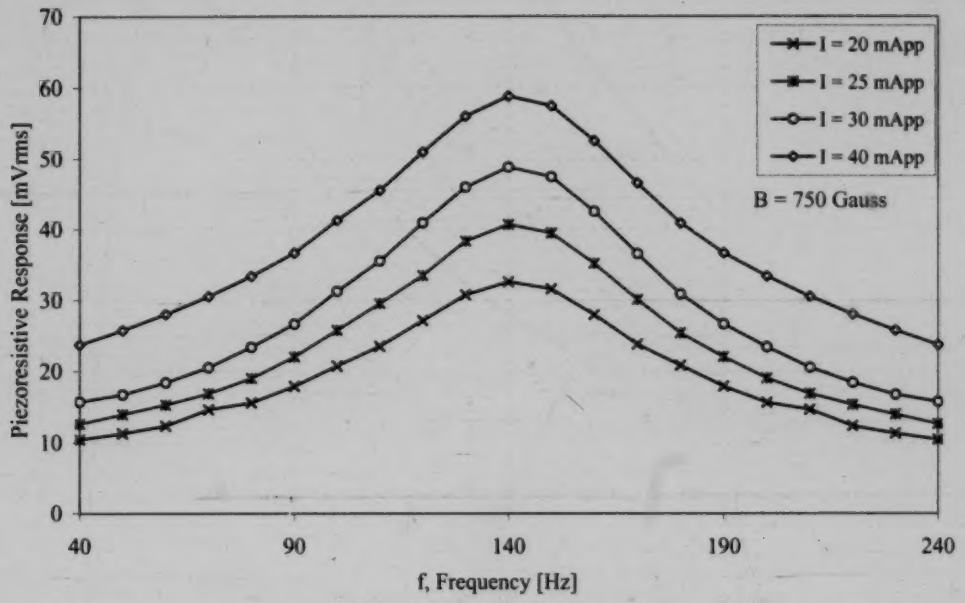

Figure 4.21: Piezoresistive response of medium cantilever dynamically actuated in distilled water.

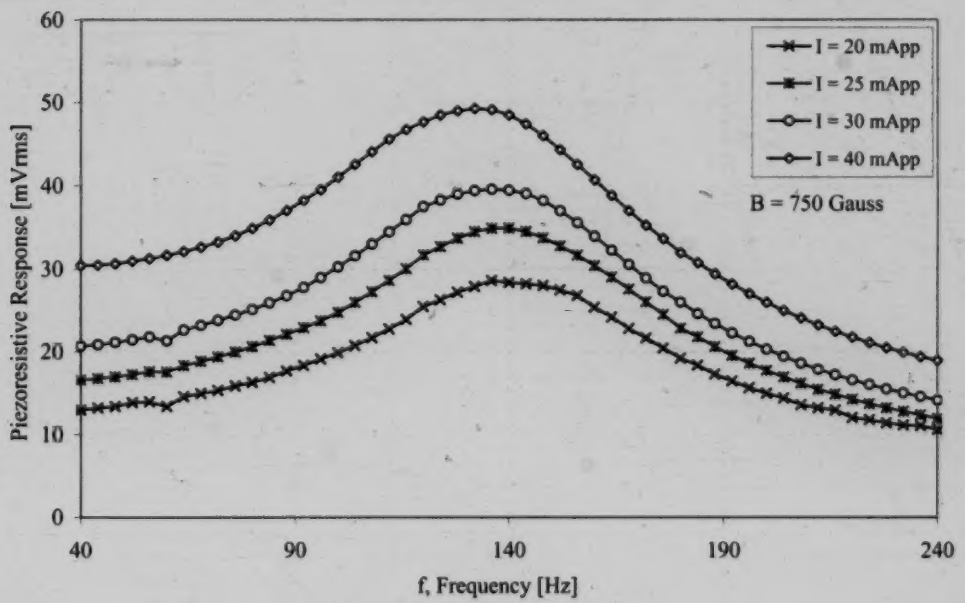

Figure 4.22: Piezoresistive response of medium cantilever dynamically actuated in IPA.

The resonant frequency of the small cantilever was observed to diminish from 2663 Hz in air to 1350Hz in distilled water and to 420 Hz in IPA. Similarly, the resonant frequency of the medium cantilever decreased from 1132 Hz in air to approximately 140 and 136 Hz in distilled water and IPA, respectively. At present, it is not known why the small cantilever exhibits a large distinguishable difference between resonant frequencies in the two differing fluids, and the medium cantilever does not.

The maximum piezoresistive responses (at 40 mA_{pp} actuation current) for the small cantilever were recorded as 43.6 mVrms and 29.2 mVrms in distilled water and IPA, respectively, compared with 555.1 mVrms in air. For the medium cantilever, the maximum piezoresistive responses (also at 40 mA_{pp} actuation current) were recorded as 58.4 mVrms and 49.3 mVrms in distilled water and IPA, respectively, in comparison with 703.7 mVrms in air. The diminished piezoresistive responses for both cantilevers in IPA and distilled water indicate that the highly damped structures are undergoing smaller oscillations. The decreases in resonant frequency and amplitude of vibration, from the values obtained in air, are discussed in Chapter 5.

It was also observed that the resonant frequency of both devices was altered following testing in fluids. After immersion in, and evaporation of distilled water onto the devices, the cantilevers were retested for dynamic response in air. The resonant frequency of the small device was observed to decrease by approximately 83 Hz (compared with initial test results in air); the frequency of the medium device decreased by 80 Hz. Similarly, the resonant frequency of devices following submergence in and evaporation of isopropyl alcohol deviated an additional 60 and 30 Hz for the small and medium cantilevers, respectively. This behaviour, exhibited during a typical immersion-

drying cycle was investigated once, and should be further investigated to determine if this behaviour regularly occurs during fluids testing. The shifts in resonant frequency observed during the single round of tests are not readily explained; however, hypotheses are presented in the following chapter.

4.3.2.2 Optical Detection Data

In order to corroborate the amplitude of vibration data obtained by employing Equation (3.3.26), dynamic response data was taken for the small and medium size micro-cantilevers utilizing the optical detection method outlined in Section 4.2.2. The results presented in this section were collected prior to testing of the devices in distilled water or IPA. Figures 4.23 and 4.24 illustrate the resonance curves obtained for the small and medium micro-cantilevers, respectively. These results were produced with an external magnetic field of approximately 675 Gauss and actuation currents of 44.4 mA_{pp} for both the small and medium structures. The Lorentz forces produced by the interaction of the current and magnetic field of these magnitudes are equal to those produced during testing of the piezoresistive response. The resonant frequencies for the small and medium structures were measured to be 2663 and 1132 Hz, respectively. At resonance, the maximum tip deflection was approximately 185.1 ± 3.5 μm for the small cantilever and 542.5 ± 10.3 μm for the medium. The results from these, and previous experimentation are discussed in the following chapter.

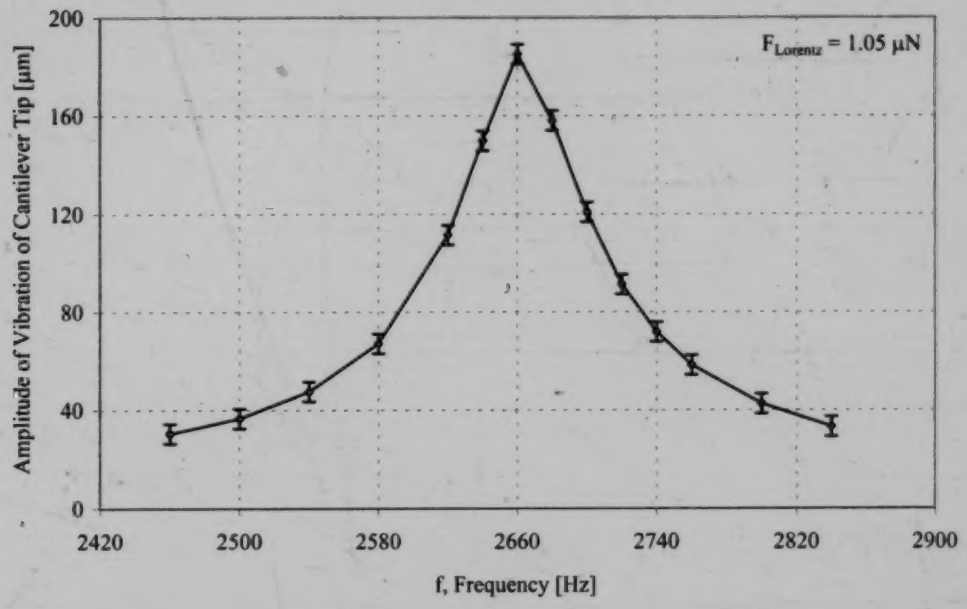

Figure 4.23: Tip deflection of small micro-cantilever, measured using optical method.

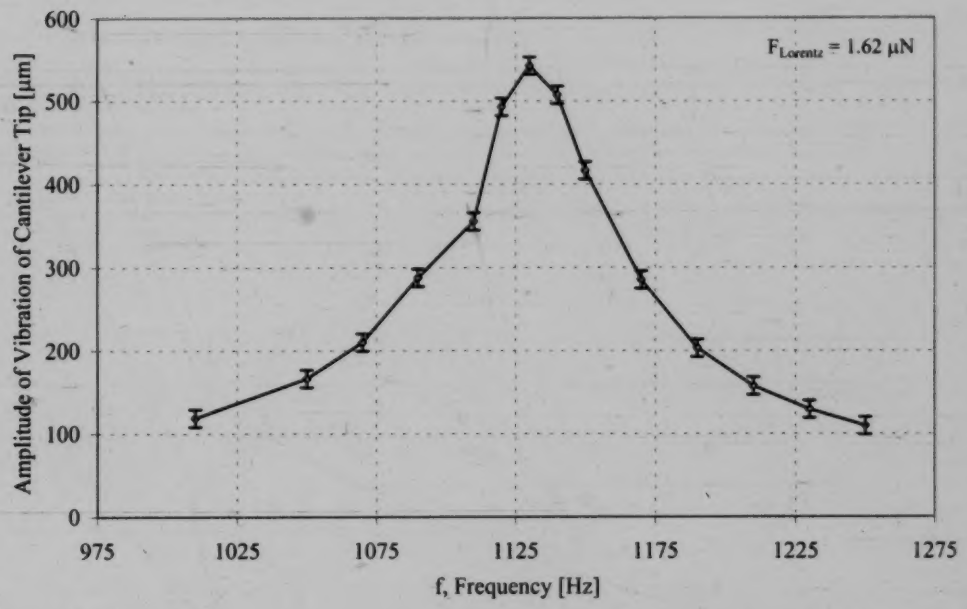

Figure 4.24: Tip deflection of medium micro-cantilever, measured using optical method.

Chapter 5

DISCUSSION

5.1 Introduction

Over the past few years, research endeavours have shown the feasibility of utilizing micro-flap-based actuators to control and produce localized airflow [6]-[8]. Projects involving micro-size structures have focused primarily on the production or modification of local flow in air, but have not attempted to quantify micro-actuator response in fluid media.

In order to determine whether CMOS-fabricated micro-cantilever devices can induce local fluid flow, it is necessary, as a preliminary step, to investigate the behaviour of the devices in differing fluid media. This characterization will allow for the determination of the environments for which the devices are best suited. If the dynamic response of the devices is severely affected or hampered by a highly viscous fluid, for instance, the devices may be optimally functional only in fluids that produce minimal damping on the structures. Similarly, the size of the structures must be recognized as an important factor in the performance of the micro-actuators. Smaller devices cannot be subjected to large Lorentz forces and therefore may not produce sufficient motion to counteract viscous drag effects. Larger devices produce larger Lorentz forces; however, these devices may also be limited due to drag acting on large surface areas.

In this chapter, the experimental data presented in Chapter 4 will be discussed and compared with results obtained from both the theoretical and finite element models introduced in Chapter 3. Difficulties encountered with the present designs and possible

improvements are also discussed. Furthermore, the possibility of utilizing the micro-cantilever-based device as a suitable fluid control mechanism will be put forward, as well as other possible device applications.

5.2 Static Deflection

5.2.1 Deflection in Air

In this section, the experimental performance of the cantilever devices during static actuation is compared with the results from both finite element simulation and simple beam theory. Figure 5.1 illustrates the resultant data obtained from optical testing, ANSYS simulation and analytical computation for the small micro-cantilever. Similarly, the equivalent curves for the medium micro-cantilever are shown in Figure 5.2.

Finite element and simple beam theory-based calculations were conducted for the micro-cantilevers with varying thickness of nitride. The 0% and 100% nitride results are shown for the FEM model and only the 0% nitride results are presented for the simple beam theory model. As shown in Figures 5.1 and 5.2, the nitride-free models, from the two computational methods, best approximate the experimental results. The FEM and simple beam theory models show excellent agreement of results for both cantilevers, with errors of approximately 5%; larger deviations are evident in comparing the two models with experimental data. There exist, for the small cantilever, approximate 39.1 and 15.1% differences between the ANSYS 0% nitride simulation and the best-fit curves for negative and positive Lorentz forces, respectively. Similarly, differences of approximately 3.7 and 34.7% are observed for the medium cantilever.

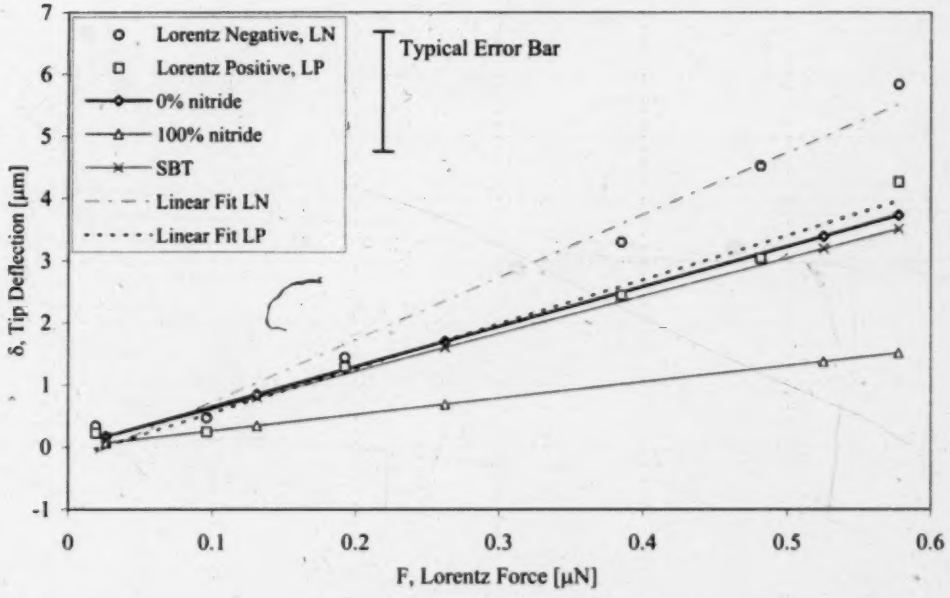

Figure 5.1: FEM, analytical, and optical static deflection data for the small cantilever. LN and LP denote optical results, the 0 and 100 % nitride lines are results from ANSYS modeling and SBT denotes results obtained from applying simple beam theory.

Discrepancy between results from both the small and medium cantilever optical results and those from simple beam theory and FEA are assumed to be a result of residual stress. This would also account for the difference in magnitude of deflection observed in the negative and positive directions. As previously discussed in Chapter 3, certain layers comprising the composite cantilever are either in tension or in compression as a consequence of thermal cycles and differing deposition rates during manufacture. These compressive and tensile stresses will limit the deflection of the structures either into or out of the plane of motion. If, for example, the bottom layers of the device are in tension, the small Lorentz Forces (typically on the order of 0.03 to 0.8 μN) generated may not be

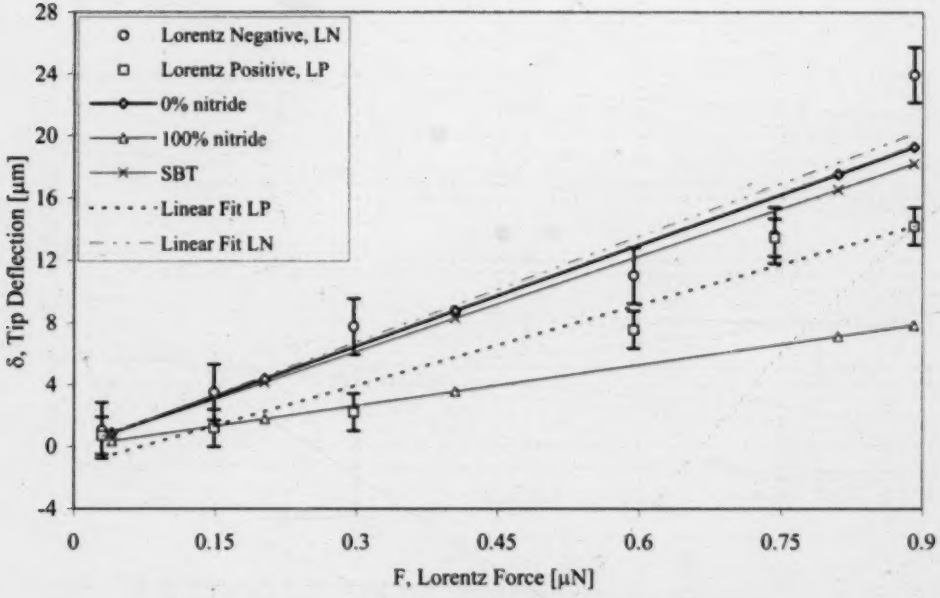

Figure 5.2: FEM, analytical, and optical static deflection data for the medium cantilever. LN and LP denote optical results, the 0 and 100 % nitride lines are results from ANSYS modeling and SBT denotes results obtained from applying simple beam theory.

sufficient to appreciably deflect the cantilevers downwards.

Residual stress is also the cause of the non-functionality of the large cantilever device. It is believed that the residual stresses are too great for the generated Lorentz forces to overcome. Small deflections of the tip may occur; however, the curvature of the structure is so great, that minimal deflection of the free end of the cantilever will not readily translate to the support arm region in which the piezoresistive elements are located. In order to understand the small deflections that are undergone by a curved (circularly arced) beam, we consider Castigliano's theorem [45, p. 181] for the end deflection, δ, of a curved, unstressed beam, which gives

$$\delta = \frac{\partial U}{\partial P} \tag{5.2.1}$$

where U is total strain energy of the system and P is the applied point load. The total strain energy is typically given by the summation of the strain energies due to bending, axial loading and shear loading. If the ratio of the length to the depth of the beam is greater than ten, as with all three micro-cantilevers, the strain due to axial and shear loading may be neglected; therefore, the deflection of the cantilever tip may be written as

$$\delta = \frac{\partial U}{\partial P} = \int \frac{M}{EI} \frac{\partial M}{\partial P} dz \tag{5.2.2}$$

where dz is taken along the length of the structure. In polar coordinates, the moment along the curved beam is given by

$$M = rP(\cos\beta - \cos(\phi + \beta)) \tag{5.2.3}$$

where r is the radius of curvature and ϕ is the angle as measured between the point of application of the load and a point, x, along the beam, as shown in Figure 5.3.

In combining Equations (5.2.2) and (5.2.3), and solving for the deflection of the tip of the cantilever, it is determined that an actuation current of 30 mA and a magnetic field of 750 Gauss will produce a deflection of approximately 27.4 μm (for a radius of curvature of 663 μm, as determined for the large cantilever by visual inspection of microphotographs). This relatively small translation at the tip of the device will cause a

minimal deflection at the location of the piezoresistors (the center of which is located 937.5 μm from the cantilever tip). This small deflection will create a negligible strain on the piezoresistors, which will result in an undetectable piezoresistive response.

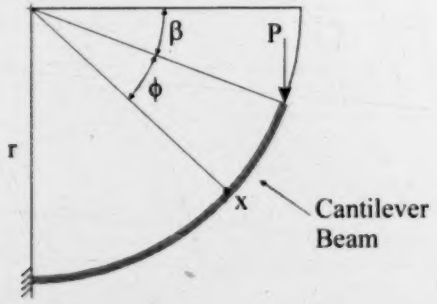

Figure 5.3: Curved Beam subject to free end loading.

5.2.2 Comparison of FEM Simulation and Expression (3.3.26)

The computational data was further compared with results obtained from determining the static deflections of the structures based on piezoresistive response. Equation (3.3.26), relating the piezoresistive response to the static deflections of the micro-cantilevers, was developed in Section 3.3.3. Figures 5.4 and 5.5 show the curves as calculated utilizing this expression. In developing Equation (3.3.26), it was assumed that the tip deflection of the structures could be effectively predicted with small deviation from experimentally obtained results. In knowing the static deflection of the structures, the stiffness, k, of the cantilevers can be calculated and applied to similar expressions developed to determine amplitude of vibration during dynamic actuation.

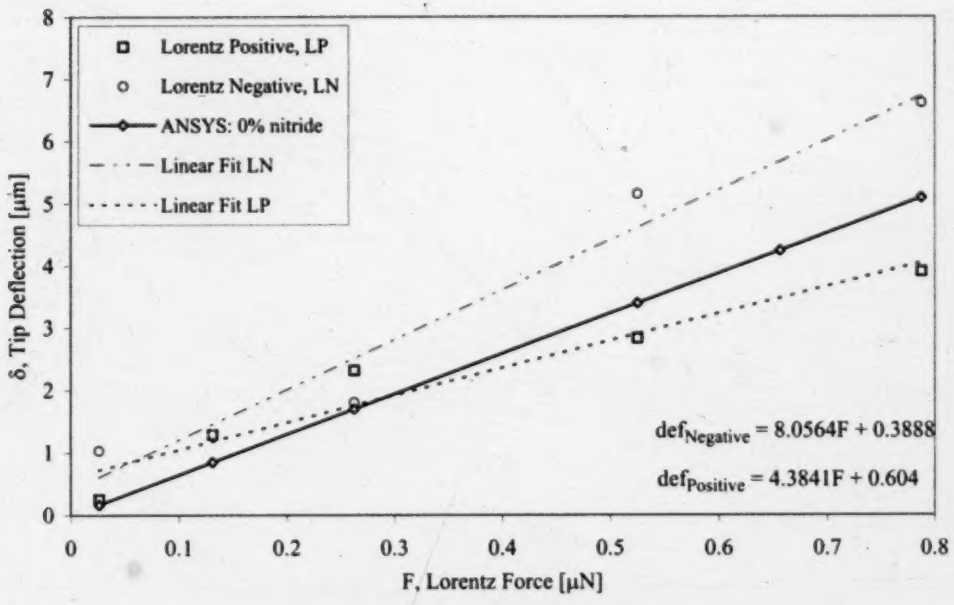

Figure 5.4: Static tip deflection results for the small cantilever obtained from FEM modeling and application of Equation (3.3.26).

In incorporating the stiffness constant (calculated by taking the average of the inverse slope of the optical measurement plots shown in Figures 5.1 and 5.2), the piezoresistive output and known material and geometric parameters into Equation (3.3.26), it was determined that the curves for tip deflection versus Lorentz force correspond well with the nitride-free finite element and simple-beam theory curves. The finite element results, illustrated in Figures 5.4 and 5.5, for both devices fall within the deflection range obtained through implementing Equation (3.3.26). This agreement supports the hypothesis that the nitride is being etched during post-processing. Furthermore, the good agreement of the results computed using Equation (3.3.26) with optical results implies that the methodology behind developing Equation (3.3.26) is valid

in approximating the tip deflection of the micro-cantilevers, while under the influence of a static force.

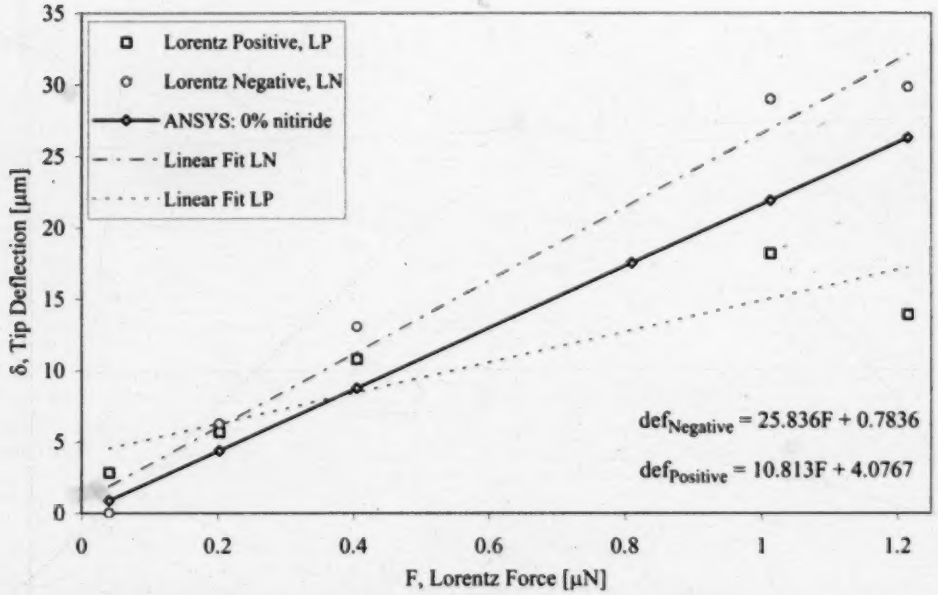

Figure 5.5: Static tip deflection results for the medium cantilever obtained from FEM modeling and application of Equation (3.3.26).

5.3 Dynamic Response

5.3.1 Structural Response in Air

In this section, the results obtained in Chapter 4 for the dynamic behaviour of the devices are compared against similarly based models as those incorporated in the static analysis. Finite element simulations and single degree-of-freedom vibration theory analyses were conducted and results derived from coupling Equation (3.3.27) with experimentally obtained piezoresistive response were generated. These analyses were performed in order to predict and characterize the motion of the micro-actuators in air.

These predictions will essentially be used as the first step in characterizing the interaction between micro-cantilever structures and fluids, and the efficiency of CMOS cantilever-based devices as suitable actuators or fluid modification systems.

The finite element models, generated for both the small and medium cantilevers, were initially tested to determine the different modes of vibration that occur over a specified frequency range in which such devices are typically actuated. It was found that within the frequency range of 2400 to 12000 Hz for the small cantilever and 900 to 9500 Hz for the medium cantilever, the micro-structures undergo four distinct modes of vibration, as illustrated in Figure 5.6: (a) out-of-plane bending, (b) torsion about the x-axis, (c) torsion about the z-axis, and (d) undulating motion. It was assumed that the motion created by out-of-plane bending would be most prominent in the production of fluid flow or active control of fluid behaviour, and therefore the primary focus of the subsequent FEM analyses was placed exclusively on this mode.

The results from the single degree-of-freedom model (developed in Section 3.3.2) were generated by inputting resonant frequencies equal to those obtained experimentally (2663 Hz and 11332 Hz for the small and medium cantilever, respectively). The thickness of the nitride layer was then varied in the model until the computed tip deflections were observed to be comparable with experimental results compiled using the optical detection method. Furthermore, the resonant frequencies and damping ratios were input based on results obtained experimentally. The damping ratios, determined in air to be approximately 1.42% for the small cantilever and 2.04% for the medium cantilever, were also input into the finite element models. Figure 5.7 illustrates the existing correlation, for the small cantilever, between ANSYS simulations (with 0, 50, and 100%

of the manufacturer's specified nitride thickness of 0.5 μm) and single degree-of-freedom theory results, as well as the results obtained from optical measurements. Similarly, the results compiled from similar models and testing procedures are shown in Figure 5.8 for the medium device. In both Figures 5.7 and 5.8, the data points for have been joined via straight lines.

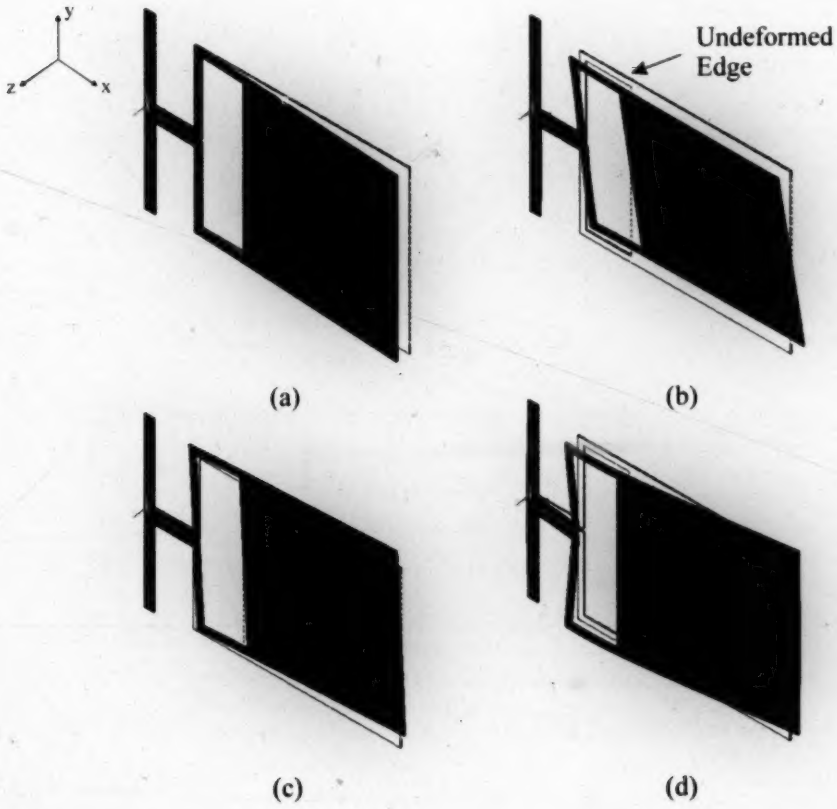

Figure 5.6: ANSYS results illustrating the first four modes of vibration for the micro-cantilevers. Small Cantilever: (a) 2.5 kHz; (b) 11.9 kHz; (c) 19.5 kHz; (d) 23.8 kHz. Medium Cantilever: (a) 0.9 kHz; (b) 4.3 kHz; (c) 7.1 kHz; (d) 9.4 kHz.

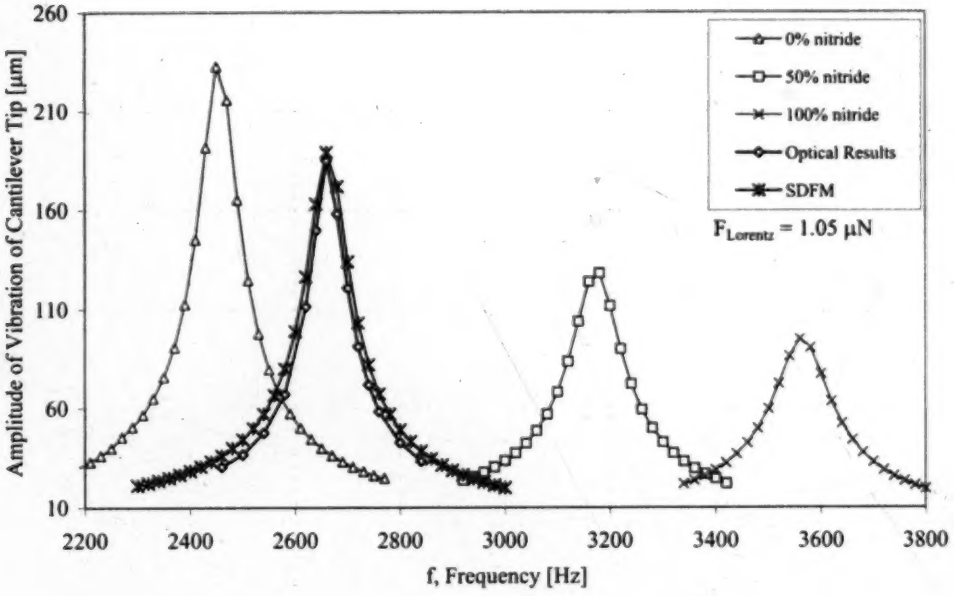

Figure 5.7: FEM, analytical, and optical measurement dynamic response data for the small cantilever. The 0, 50 and 100 % nitride lines are results from ANSYS modeling and SDFM denotes results obtained from applying the single degree-of-freedom model.

As illustrated in Figures 5.7 and 5.8, as the uppermost nitride layer is diminished, from 0.5 to 0 μm (100-0% of the original nitride layer), the resonant frequencies of both devices increase and the amplitudes of vibration decrease. The nitride layer contributes greatly to the stiffness of the devices (as it exhibits a Young's modulus approximately five times greater than that of the remaining constitutive layers), thereby reducing the range of tip vibration and increasing the frequency at which resonance occurs, as predicted by single degree-of-freedom theory. Data pertaining to the finite element simulations, for the small and medium cantilever devices, as well as the single degree-of-freedom theory and optical results, are contained in Table 5.1.

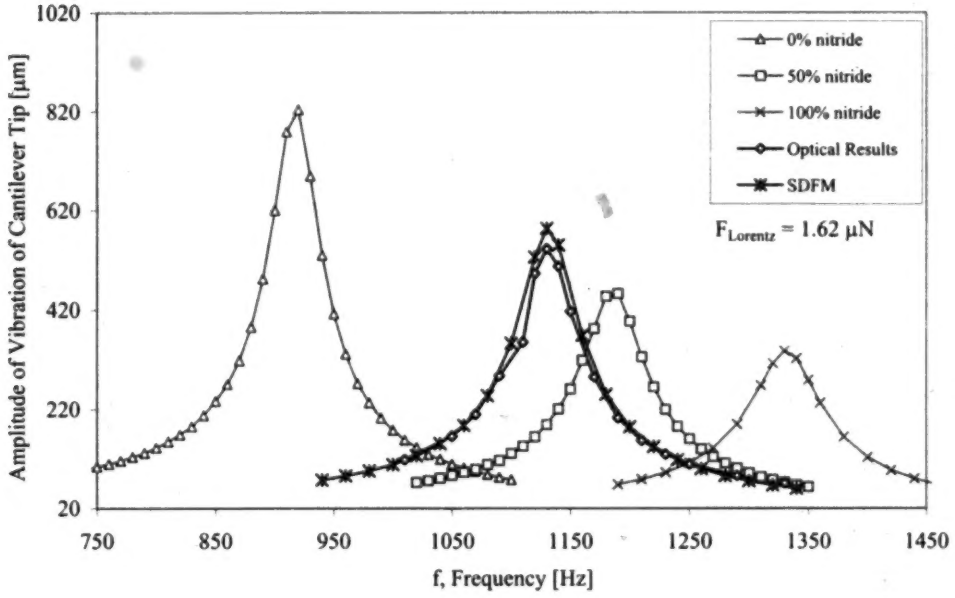

Figure 5.8: FEM, analytical, and optical measurement dynamic response data for the medium cantilever. The 0, 50 and 100 % nitride lines are results from ANSYS modeling and SDFM denotes results obtained from applying the single degree-of-freedom model.

Table 5.1: Finite element, analytical, and optical results for Figures 5.7 and 5.8.

	Small Cantilever		Medium Cantilever	
Result Method	Frequency [Hz]	Amplitude [μm]	Frequency [Hz]	Amplitude [μm]
ANSYS				
0% N Model	2455	232.7	917	824.4
50% N Model	3180	128.3	1190	452.6
100% N Model	3560	95.0	1330	337.3
SDFM	2663*	189.1	1132*	583.7
Optical	2663*	185.1	1132*	542.5

**NOTE: In Table 5.1, data pertaining to the simple beam theory was derived by inputting the resonant frequency obtained through experimentation, therefore the resonant frequencies of the SDFM analyses and optical data are equivalent.*

From the data presented in Table 5.1, it is shown that, for the small cantilever, the resonant frequency and amplitude of vibration obtained by optical means correspond with least error to the ANSYS 0% nitride simulation. As with Figures 5.1 and 5.2, the proximity of the two curves would indicate that most, if not all, of the passivation layer is etched during device post-processing in XeF_2. The medium cantilever, however, shows better agreement with the 50% nitride FEM model. The analytical models with approximately 11%, for the small cantilever, and 20%, for the medium cantilever, of the original nitride layer thickness, were determined to correspond best with optical results.

For the small cantilever, the difference in amplitude between the simulated (0% nitride) and optical results is approximately 20.5%, in comparison with a difference of approximately 2.2% between analytical (11% nitride) and optical results; the difference in resonant frequency is 7.7% between the simulated and optical data sets. Similarly, for the medium structure, the difference in amplitude between the ANSYS 0% model and experimental data, and theoretical (20% nitride) and experimental results are 52.0% and 7.6%, respectively, with a resonant frequency deviation of 19.0% when comparing finite element and experimental data. These results would indicate that a small fraction of the original nitride layer is present on the surface of the micro-cantilevers following 28 etch pulses in XeF_2.

Discrepancies between the finite element and experimental curves, for both

structures, could also result from uncertainties in the thickness and material properties of the constitutive layers. The finite element models were created using dimensional data provided by the Mitel Corporation; however, Mitel concedes that the specified thickness of the layers may deviate by 10 to 20%. Furthermore, the material properties of the layers may be different from those used for the purpose of simulation. Thin film values were utilized where available; however, bulk values were substituted when the thin film values were not known. Differences in material properties used for simulation and actual values will cause the resonant frequencies of the devices to differ from experimental results. Values for density, for example, if specified to be greater than in the real case will cause resonance to occur at lower frequencies; higher values of Young's modulus will increase the stiffness of the devices, thereby also increasing resonant frequency. The material properties and layer thickness were not modified during investigation.

Furthermore, the stiffness of the devices is altered by the presence of residue on the support arms of the structures and the exclusion of residual stress effects from the FEM models. The folded support arms were incorporated into the design of the structures so as to allow for greater flexibility of the devices. During manufacture of the devices, a residue was deposited or formed between adjacent arm sections and at sharp corners of the devices, as shown in Figure 5.9. At present, the material composition of the residue and the means of formation are not known. The presence of the residue effectively reduces the flexibility of the arms, thereby increasing the overall stiffness of the structure. As the stiffness of the structure is increased, the natural frequency (equivalent to the resonant frequency for small damping) of the structure will also experience an increase. This relationship between device stiffness and resonant

frequency was previously illustrated in Chapter 3, by Equation (3.3.14).

The mass of the residue will also affect the response of the structure; however, the mass ratio of the residue to that of the structure was visually estimated to be small, therefore it is believed that the extraneous material will more adversely affect the stiffness of the structure, rather than the total mass.

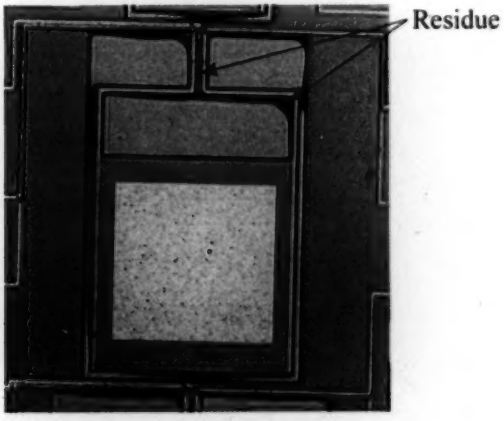

Figure 5.9: Micro-cantilever with residue attached to the folded support arms.

Similarly, it has been shown that the resonant frequency is affected by the presence of residual stress. It has been observed that when compared with experimental results, finite element models that do not compensate for residual stress show resonant frequencies that differ from 7 to 10% [27], [46]. Following the CMOS fabrication process, the layers comprising the micro-cantilevers are either in a state of compression or tension. These internal stresses add to the stiffness of the devices, which will, as with the residue, increase the resonant frequency of the freestanding structure.

5.3.2 Comparison of FEM Simulation and Expression (3.3.27)

Expression (3.3.27) relating the piezoresistive response to the amplitude of vibration of the microstructures was developed in Section 3.3.3. This expression is a precursor to developing relationships between amplitude of vibration and pressure distribution in a fluid, and subsequently between pressure distribution and fluid behaviour and motion. In utilizing the final set of derived equations and by monitoring the piezoresistive response, the fluid flow may be calculated and regulated by modifying the resonant response of the micro-cantilevers. From applying expression (3.3.27) at varying frequencies, curves were compiled and compared with the FEM (0% nitride) simulation results presented in the preceding section. The comparison of the two models is shown in Figures 5.10 and 5.11 for the small and medium cantilevers, respectively.

The percentage differences in amplitude, shown between the FEM and Equation (3.3.27) results, for the small cantilever are approximately 17%, 28%, and 14% at actuation currents of 1, 20 and 40 mA_{pp}, whereas the medium cantilever yields differences in amplitude of approximately 31%, 16%, and 7% for the same values of alternating current. Disparities arise partially from simplification of the strain term incorporated into Equation (3.3.27). The expressions (developed to relate piezoresistive response to the amplitudes of vibration of the structures) were derived by taking only bending strain into account. The total strain at the surface of each layer, however, is given by the superposition of strains due to thermal expansion and bending. The strain at the top and bottom surface of the piezoresistive element is therefore given by

$$\varepsilon_i = \varepsilon_{thermal} + \varepsilon_{bending} \qquad i = 1, 2 \qquad (5.3.1)$$

where the subscripts i denote the top (i=1) and bottom (i=2) surfaces of the piezoresistive sensor. The thermal strains on the surfaces of the element is given by the equation

$$\varepsilon_{thermal} = \alpha(T - T_o) \tag{5.3.2}$$

where α is the thermal coefficient of expansion of the material, T is the temperature the layer equilibrates to during actuation, and T_o is the temperature of the device when not actuated.

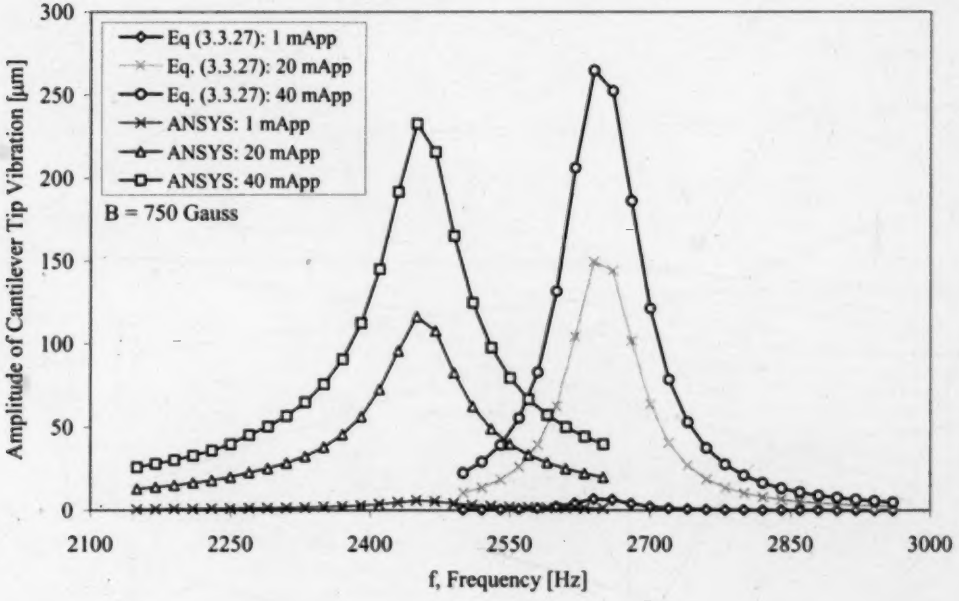

Figure 5.10: Dynamic response results for the small cantilever obtained from FEM modeling and application of Equation (3.3.27).

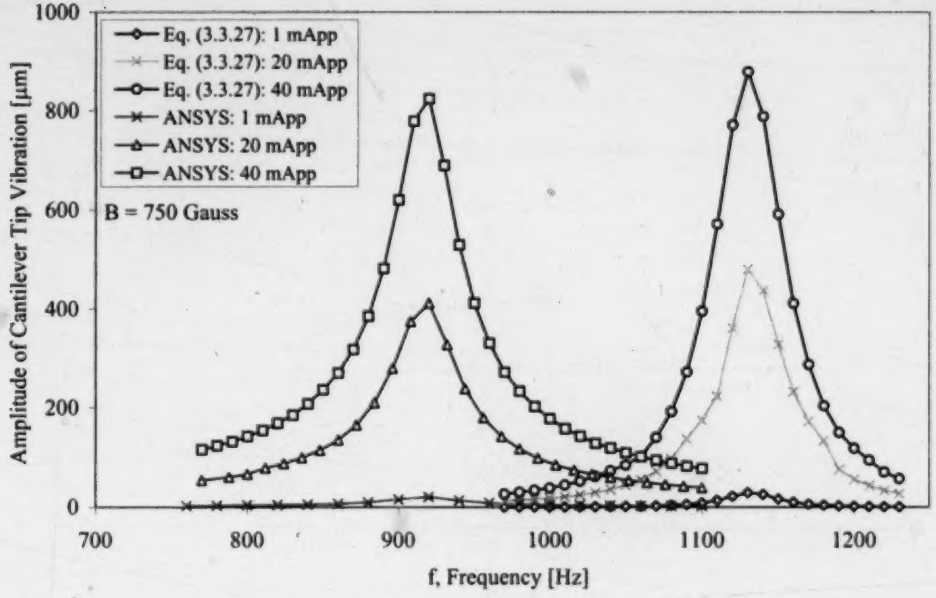

Figure 5.11: Dynamic response results for the medium cantilever obtained from FEM modeling and application of Equation (3.3.27).

Substituting Equations (5.3.1), (5.3.2), (3.3.23), (3.3.24), and (3.3.12) into (3.3.22) and rearranging the resultant equation gives

$$w_o = \frac{a}{k} \cdot \left[\frac{\Delta V}{I_o (GF) R} - \alpha (T - T_o) \right] \cdot \frac{1}{b}$$

where

$$a = \left[\frac{EI}{t(L-x)} \right] \tag{5.3.3}$$

and

$$b = \sqrt{\left(1 - \frac{\omega^2}{\omega_n^{\,2}} \right)^2 + \left(2\xi \cdot \frac{\omega}{\omega_n} \right)^2}$$

In implementing these changes, it is expected that the extrapolated amplitude of vibration for both devices will be less than that calculated by taking into account only the bending strain acting the structures. In order to determine the degree to which Equation (5.3.3) better approximates the amplitude of vibration of the micro-cantilever devices, it is necessary to know the temperature to which the piezoresistive element will rise during actuation. To determine the average temperature of the piezoresistors, the resistance of the aluminum trace, directly beneath the piezoresistors, is measured. Through conduction, the piezoresistors will be heated by the trace and equilibrate to approximately the same temperature. In knowing the resistance, the temperature of the trace can be calculated using the temperature coefficient of resistance or TCR. At the time of writing, the average temperature of the trace was unknown, and therefore it is not known the extent to which Equation (5.3.3) will increase the accuracy of the extrapolated amplitude of vibration response.

Differences in amplitude of vibration resulting from use of Equation (3.3.27) are relatively large, with a maximum of 31%; however, it is believed that this expression is adequate in providing a rudimentary perspective into the amplitude of vibration of lightly damped systems. Care must be taken in implementing this expression, as it is sensitive to changes in the input parameters. A change in stiffness, for instance, for the small cantilever, from 0.1693 to 0.1603 μN/μm or approximately 6%, will produce amplitudes of 264.7 and 281.8 μm, respectively, or 6.5%, for an actuation current of 40 mA and a magnetic field of 750 Gauss.

Of the variables in Equation (3.3.27), k is determined through best-fit approximations of experimental results; the remaining variables are known due to device

geometry, material properties or experimentation with low uncertainties (piezoresistive response). It is therefore imperative that values for device stiffness accurately reflect the geometry and behaviour of the structures. This can be accomplished by conducting further experiments regarding static device deflections and refining simulations to include the effects of residual stress.

5.3.3 Comparison of Micro-cantilever Response in Fluids

Structures are prone to changes of dynamic response in differing fluids, due to the viscosity of the fluid media. This fluid property is often described as the ability of a fluid to resist a change of form due to internal friction. A highly viscous fluid, for example will not be as easily influenced by a shearing force as a low viscosity fluid. In order to characterize the behaviour of MEMS cantilevers in fluids of differing viscosities, the microstructures were tested in atmospheric conditions, as well as in IPA and distilled water. These fluids were employed at room temperature (approximately 25°C); properties of the three fluids utilized during testing are summarized in Table 5.2. The results of the fluids testing are shown in Tables 5.3 and 5.4, which compile the frequency, maximum piezoresponse, and a parameter known as the quality factor attained for an actuation current of 40 mA_{pp}.

As with the damping ratio, the quality factor, Q, is a ratio relating the resonant frequency to the two half power points, given by

$$Q = \frac{\omega_o}{\Delta\omega} \tag{5.3.5}$$

where ω_o and $\Delta\omega$ represent the resonant frequency of the suspended structure and the width between half power points, respectively.

Table 5.2: Physical properties of fluids utilized during experimentation.

Fluid	Density [gm/cm^3]	Viscosity [gm/(cm·s)]
Air	0.0012	1.827x 10^{-4} @ 18°C
		1.904x 10^{-4} @ 30°C
Distilled Water	1.00	0.0100 @ 20°C
		0.0089 @ 25°C
IPA	0.78	0.0286 @ 15°C
		0.0177 @ 30°C

NOTE: The values, shown in Table 5.2, were obtained from reference [47].

Table 5.3: Dynamic response obtained from small cantilever interaction with fluids.

Fluid	Resonant Frequency [Hz]	Piezoresistor Response [mVrms]	Quality Factor Q
Air	2663	555.1	42.2
Distilled water	1350	43.6	17.6
IPA	420	29.2	1.1

Table 5.4: Dynamic response obtained from medium cantilever interaction with fluids.

Fluid	Resonant Frequency [Hz]	Piezoresistor Response [mVrms]	Quality Factor Q
Air	1132	703.7	18.4
Distilled water	140	58.4	2.1
IPA	136	49.3	1.5

As the bandwidth increases due to the effects of increased damping, the value for Q will diminish. From the data presented in Tables 5.2 and 5.3, it is observed that as the viscous damping on the given structure is increased the quality factor decreases. This decrease in quality factor illustrates that as the viscosity of the test fluid increases, both the piezoresistive responses and resonant frequencies of the cantilevers decrease. By observing the behaviour of the resonant frequency, piezoresistive response, or quality factor, it is feasible to determine the viscosity of the fluid media being tested. More importantly, both the small and medium structures exhibit detectable dynamic motion over the range of viscosities tested. This would indicate that fluids with viscosities smaller than approximately 0.0213 gm/(cm.s) can be identified and potentially controlled and/or propelled via the dynamic motion of the cantilevers.

Similarly, it may be possible to determine the properties of a fluid by the resonant shift displayed by the micro-cantilever following fluid immersion and evaporation. As shown in section 4.3.2, the resonant frequency of the both cantilevers shifted following testing in a fluid. The small cantilever resonant frequency was observed to decrease approximately 83 Hz, while the medium cantilever resonant frequency was recorded as shifting approximately 80 Hz. It is uncertain why this decrease in resonant frequency

occurs; however, two possible hypotheses exist to explain this phenomenon. The first proposition is that the residue found on the support arms of the device has broken way, thereby reducing the stiffness of the devices. This reduction in stiffness will allow the structures to resonate at a lower frequency than the initial post-processed devices. Through visual inspection alone, it cannot be confirmed if the residue has been diminished following fluids testing. Furthermore, repeated testing of several devices would not aid in determining if the residue is broken during testing, as the residue deposits are not uniform from die to die.

The second possible explanation for the decrease in resonant response is adhesion of microscopic droplets of water onto the surfaces of the device. Again, visual inspection of the devices does not show droplets on the upper surface of the structures, however, it is not known if liquid remains on or below the bottom face. One way of determining if droplets remain on the lower surface is to design and fabricate a device without a central aluminum mirror; silicon dioxide is transparent, therefore it would be possible to determine if fluid particles are present. Visual inspection of the devices would ideally be performed following evaporation of the working fluid, as over a prolonged period of time the fluid may fully evaporate.

Water or IPA droplets attached to the platform will cause a detectable shift in the frequency at which resonance occurs. If adhesion does occur, it would be necessary to determine the number and size of the droplets that adhere to the surfaces of the structures. In developing a relationship for the number and mass of the adhered droplets to resonant frequency of the given device, it may be feasible to identify the fluid tested.

These hypotheses are speculative in nature, as this behaviour was tested for solely once. Further testing is required to determine if this shifting of resonant frequency, following an immersion/drying cycle, is observable in other devices on other die.

5.3.4 Finite Element Simulation in Fluids

Finite element simulation was not conducted on the micro-cantilevers in fluids, primarily due to two factors: damping effects and mesh size. The models created for this thesis cannot be utilized to characterize the behaviour of the structures in fluids due to inadequate modeling of the fluid-structure interaction. While submerged in fluid, the cantilevers are subject to both viscous damping and mass loading by a fluid boundary layer around the periphery of the devices [48]. This added mass moves in tandem with the structure and serves to reduce the resonant frequency of the system; therefore simply inputting the damping ratio into the ANSYS models will not produce reliable FEM output.

In order to solve this complication, a finite element acoustic analysis may be performed that takes into account the interaction between a solid and a surrounding fluid medium. Coupled acoustic analysis, which is available in ANSYS, may be employed to determine quantities such as pressure distribution, pressure gradient and particle velocity in a fluid under the influence of a structure in motion.

ANSYS element type FLUID30 is specifically designed for the 3-D model generation of coupled acoustic problems. This element type effectively simulates both the fluid medium and the boundary layer that surrounds the cantilever device. The relatively large size of the pit or channel surrounding the cantilever structures in this

work, however, dictates that the fluid component of the model have a fine mesh to attain convergence of results. The models created for the small and medium cantilevers contain 9894 and 12554 nodes, respectively. In adding the fluid medium, the number of nodes and elements will increase greatly, thereby increasing computational time and reaching the nodal number limit (32000) in the University High Option version of ANSYS employed during the course of this work. In decreasing the number of elements in the models, it may be possible to perform acoustic coupled analysis; however, reduction of elements will not lead to full result convergence and in turn will yield results with a certain degree of error. A coupled acoustic analysis was not performed for this thesis.

5.4 Device Design and Optimization

The micro-cantilever devices were designed such that the platforms would be allowed an optimized range of motion during both static and dynamic actuation. This relatively large range of motion was attained through the implementation of folded support arms at the base of the platform; however, this support arm structure also contributed to the structural fragility of the microstructures.

The member spanning the width of the channel and the support arms attached to the platform were designed to be 20 μm in width, thereby minimizing the moment of inertia of the constitutive arms and reducing the overall stiffness of the micro-cantilevers. In minimizing the dimension of the support arm cross-section, however, the thin nature of the arms proved challenging in the successful post-processing of the devices. During post-processing, the material beneath the structures is slowly etched, creating a gradually diminishing silicon pyramidal column centered beneath the platform. At the final point

of detachment of the platform from the pillar, the residual stress inherent throughout the structure causes the platform to spring out of the plane of the CMOS die. At random instances, the released devices showed severed connections between the two piezoresistors in series. At this particular location, the residual stress is maximum. If the support is considered to be a simply supported beam [45, p. 473] the critical stress, or the stress at which this member will fail is given by

$$\sigma_{critical} = \frac{\pi^2 EI}{L^2 A_{member}} \tag{5.4.1}$$

where I is the moment of inertia, L is the length, and A_{member} is the cross-sectional area of the support beam. For the small and medium cantilevers, the critical stress was calculated to be approximately 3.53 and 1.62 MPa. The medium device was more prone to breakage than the smaller structure; this trend is due to the greater length (a difference of 190 μm) of the medium cantilever support. The difference in length results in the critical stress for the medium cantilever being approximately one half that of the small cantilever. Increasing the thickness of the arms will create a more robust device, while sacrificing some of the flexibility of the structure. A similar analysis was conducted in [49] for fixed micromachined beams.

Furthermore, increasing the width of the support arms will potentially protect the aluminum layer during device fabrication. The yield of functional devices designed for this thesis was poor, approximately 30-40%. Poor yield arose from over-etched aluminum regions thereby creating damaged or incomplete aluminum current paths. It is

believed that the proximity of the aluminum trace to the regions open to the substrate was too close.

Lastly, residual stress was observed to have a greater effect on devices with relatively large surface area. Although structurally sound (i.e. aluminum trace and support arms are intact) residual stress served to contribute to the rigidity of the structures; in particular, it is believed that the large micro-cantilever was rendered inoperable by the inherent stress. The small and medium devices also exhibited residual stresses, but not to the extent of the large structure. The non-functionality of the large device indicates that there is a design threshold for the length and/or width of the structures that can be designed and successfully tested using CMOS fabrication. Finite element modeling of the device designs prior to submission for fabrication would predict device behaviour and/or diminished device performance.

5.5 Pumping Performance Testing

Attempts were made during the course of experimentation to determine the fluid pumping ability of the dynamically actuated devices. A schematic of a prepared die devised to be utilized in the determination of pumping performance is shown in Figure 5.12. Channel walls were first created onto the surface of the CMOS fabricated devices via a laser writing technique. This technique initially involves the spinning of a thin (approximately 150 – 200 μm thick) layer of Norland Optical Adhesive No. 81 UV-curable adhesive onto the surface of a sectioned 6-inch diameter wafer. Micro-channels are then formed, along both sides of the micro-cantilever array, by computer-controlled movement of the wafer under the focused beam from a helium cadmium (HeCd) laser.

The sections of adhesive exposed to the laser radiation are cured or harden, whereas regions not exposed remain pliable and are subsequently removed in an acetone bath. Following the removal of excess adhesive, the wafer section is placed into a UV box for approximately one hour in order to allow the patterned polymer to fully cure.

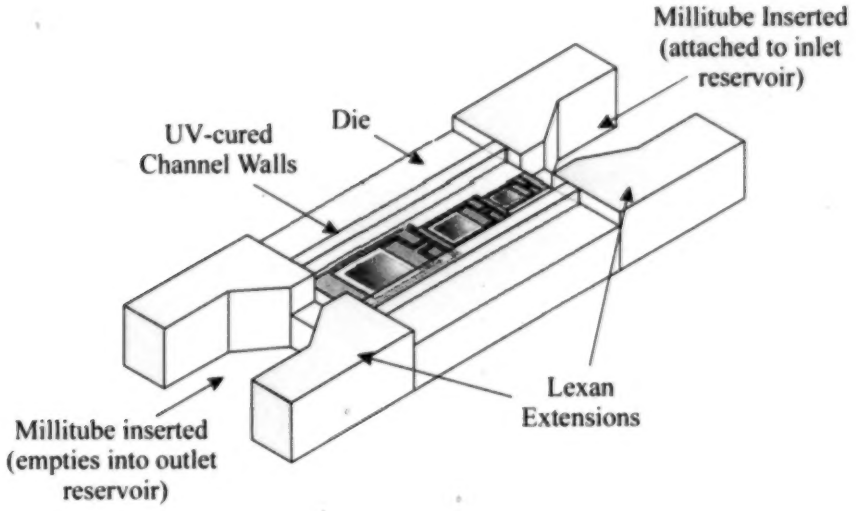

Figure 5.12: Schematic of a die prepared for pumping performance testing (performed while devices are dynamically actuated).

Following the laser writing process, the wafer section was diced and the individual devices or die were adhered to a customized, printed circuit board. Lexan® extensions, flanking the inlet and outlet of the cantilever array and millitubes inserted into the side extensions, were then added in order to facilitate the measurement of attainable flow rates. The devices were then bonded and post-processed and the micro-channels capped with a thin glass lid; this configuration was in turn positioned onto a circuit

breadboard. Following this preparation, the millitubes were to be connected to an inlet reservoir, as indicated in Figure 5.12, containing a specified fluid and an outlet reservoir into which the fluid would ideally flow. As the devices were actuated, the level of fluid collected in the outlet reservoir and the time required for collection would be monitored. From these quantities, the flow rate at different actuation currents was to be determined.

This setup was proven unsuccessful due to the large undercutting of the devices that occurred during post-processing in XeF_2. The undercut resulted in the cracking and chipping of the die surface, which yielded non-functional devices that could not be tested in fluids. It is believed that anisotropic etching will produce less fragile devices, that in conjunction with the laser writing process, can be tested for fluid propulsion efficiency.

5.6 Micro-cantilever Applications

MEMS based micro-flaps or actuators can potentially be employed in a variety of environments and/or applications. In particular, cantilever-based actuators have possible applications in the aerospace, industrial and medical fields.

The original intent of this thesis was to demonstrate that magnetically actuated micro-cantilevers could control, modify or produce fluid flow. While it has been shown that these structures, when actuated dynamically, have mobility in fluids, it remains to be demonstrated that flow is modified or produced. Studies on large cantilevers [7] have shown flow generation abilities; therefore, it may be feasible to incorporate micro-cantilever-based actuators into industrial and medical fields. It is possible that as the cantilevers oscillate a pressure gradient will be induced along the length of a channel in which the cantilevers, studied for this work, are suspended. This pressure gradient would

in turn produce fluid flow in sufficient quantity to deliver minute quantities of fuel to micro-engines or specified dosages of drugs to patients.

In addition, in industrial applications, similar micro-cantilever devices may be utilized to determine the viscosity of fluids and gases. As demonstrated in this chapter, as the viscosity of a fluid increases, the resonant response of the micro-cantilevers decreases. Portable viscosity meters could essentially be utilized to identify an unknown spilled chemical or an accidentally released gas. More fluids must be tested, however, to determine a relationship that couples resonant response, or piezoresistive response, with medium viscosity.

Lastly, micro-flaps have been studied in the area of aerodynamics in order to reduce the drag on aircraft wings. CMOS-fabricated devices could ultimately be manufactured rapidly and in large quantities that may produce sufficient motion to alter the motion of air flowing over a wing. Replacement of the large permanent magnet with a less cumbersome magnetic field source would create compact, lightweight devices that can be mounted onto the surface of a wing. The airflow over the surface can then be modified by the motion of the devices to control turbulence and thereby reduce drag.

Chapter 6

CONCLUSIONS AND FUTURE WORK

6.1 Magnetically Actuated Micro-cantilevers

Three simple CMOS-based micro-cantilevers of varying size were designed, fabricated and tested during the course of this work. Testing of the devices included determination of both the static behaviour in air and the dynamic response in air, distilled water, and isopropyl alcohol, for the three devices. The compiled data from this experimental work was then compared with analytical models (for the static and dynamic tip deflection) and finite element models.

The static tip deflections of the devices were determined to be small, and are therefore considered not to produce suitable motion for fluid control or propulsion. Conversely, dynamically actuated in air the cantilever devices produce appreciable amplitudes of vibration; however, less substantial vibrational deflections are observed in fluids. It remains to be determined if fluid flow can be modified or produced utilizing these dynamically actuated CMOS-fabricated structures.

Good agreement exists between experimental, finite element and analytically derived static and dynamic results. From the static characterization, it was observed that the static deflection of the micro-cantilevers varies linearly with constant actuation current Moreover, it was determined that the experimentally attained results coincided with model predictions obtained when the passivation or nitride layer was excluded from the model. Similar results, indicating the diminished thickness of the nitride layer, were observed through comparison of experimental and modeling results for the dynamic

response of the micro-cantilevers. It is therefore hypothesized that the silicon nitride layer is being etched during device post processing in XeF_2.

Lastly, results procured from piezoresistive detection of device behaviour were utilized to extrapolate the static tip deflection and amplitude of vibration for the devices. The extrapolated results also show good agreement with simulated results and therefore it is assumed that the extrapolation expressions are valid in making an approximation as to the motion of the micro-devices.

6.2 Future Work

The work presented in this thesis is of a preliminary nature, and may be continued or improved upon in a number of areas. Further research into the use of micro-cantilevers for flow production or control may concentrate on:

- Device optimization. Problems, such as over-etched aluminum regions, arising due to intentional violation of CMOS design rules, may potentially be compensated for by creating a set of design criteria that ensure compatibility of MEMS design with CMOS manufacturing protocols. Essentially, such design criteria can be formulated after testing and evaluating several generations of CMOS-fabricated designs. Similarly, this iterative approach will aid in the design of properly proportioned/dimensioned structures that maximize structural surface area, while minimizing the effects of residual stress.
- Device simulation. Device optimization may also be approached initially through the use of finite element modeling (FEM) rather than purely through experimentation. Finite element packages, either commercial or customized, may

be utilized to determine size thresholds and to modify shapes of structures in order to attain desired performance. Furthermore, FEM can effectively model the residual stresses acting on the structure [27], as well as the affect of these stresses on the behaviour of the structures.

- On-wafer magnetic field generation. Reduction of the external magnetic field source would aid in the transport and eventual implementation of micro-actuator devices into an intended application. On-die magnets have been demonstrated and employed to actuate similar devices utilizing a magnetic powder deposited onto the surface of the die [50].
- Anisotropic etching of structures. The structures studied for this thesis were post-processed using XeF_2. This processing method is simple, and cost effective; however, the isotropic nature of the etchant results in the undercutting of large portions of the devices. The resulting MEMS is fragile and prone to cracking or breaking; therefore, it would be beneficial to use an anisotropic etchant that shows high selectivity for the micro-cantilever structural layers. EDP, for instance may be used as the post-processing etchant; however, appropriate safety protocols must be observed due to the hazardous nature of this etchant.
- Expansion of fluids testing and determination of pumping performance. Fluids, encompassing a wide range of viscosities should ideally be tested to determine the full effect of viscous media on the behaviour of the resonating micro-cantilevers. Furthermore, in knowing that the micro-cantilever devices can be actuated dynamically in fluids, the next step in studying these devices would be to

determine the flow rate, if any, that is attainable by actuating the devices simultaneously while submerged in fluid.

REFERENCES

[1] H. Fujita, "A Decade of MEMS and its Future", Proceedings of the IEEE Microelectromechanical Systems (MEMS), (1997), pp. 1-8

[2] M. Sen, D. Warjerski, and M. Gad-el-Hak, "A Novel Pump for MEMS Applications", Trans. of the ASME – Journal of Fluids Engineering, vol. 118 (1996), pp. 624 – 626.

[3] F.C. Van de Pol, H.T. Van Lintel, M. Elwenspoek, and J.H. Fluitman, "A Thermopneumatic Micropump Based on Micro-Engineering Techniques", Sensors and Actuators, A21-A23 (1990), pp. 198 – 202.

[4] H. Mizoguchi, M. Ando, T. Mizuno, T. Takagi, and Nakajima, "Design and Fabrication of Light Driven Micropump", Proceedings of the IEEE Micro Electro Mechanical Systems (1992), pp. 31 – 36.

[5] J. G. Smits, "Piezoelectric Micropump with Three Valves Working Peristaltically", Sensors and Actuators, A21 – A23 (1990), pp. 203 – 206.

[6] F. Sherman, S. Tung, C. Kim, C. Ho, and J. Woo, "Flow Control by Using High-Aspect ratio, In-plane Microactuators", Sensors and Actuators, A73 (1999), pp. 169 – 175.

[7] H. Suzuki, N. Kasagi, Y. Suzuki, and H. Shima, "Manipulation of Round Jet with Electromagnetic Flap Actuators", Proceedings of the 1999 Annual International Workshop on Micro Electro Mechanical Systems (1999), pp. 534 – 540.

[8] T. Tsao, C. Liu, and Y. Tai, "Micromachined Magnetic Actuator for Active Fluid Control", Application of Microfabrication to Fluid Mechanics ASME (1994), pp. 31 – 38.

[9] B. Shen, "CMOS Actuators", PhD Thesis, University of Alberta, Canada, 1996.

[10] Y. Ma, "Magnetically Actuated CMOS Micromachined CIC Devices", MSc Thesis, University of Alberta, Canada, 1997.

[11] K.B. Brown, "Gas Pressure Measurements with Cantilever-in-Cantilever Micro-structures", MSc Thesis, University of Alberta, Canada, 1999.

[12] A. Gotz, I. Garcia, C. cane. E.L. Tomayo, M.C. Horillo, J. Getino, C. Garcia, and J. Gutierrez, "Micromachined Solid State Integrated Gas Sensor for the Detection of Aromatic Hydrocarbons", Sensors and Actuators, B44, no. 1-3, pt. 5 (1997), pp. 483 - 487.

[13] I. Stiharu, S. Rakheja, L. Wang, "Humidity Sensor in CMOS Technology", IEEE Can. Conf. Electrical and Computer Engineering, Edmonton, vol. 3 (1999), pp. 1652-

1657.

[14] I.M. Filanovsky, "Two Temperature Sensors Realized in BiCMOS Technology", Proceedings of the IEEE International Symposium on Circuits and Systems, vol. 6 (1998), pp. 621 – 624.

[15] C. Hierfold, A. Hilderbrandt, U. Naher, T. Scheiter, B. Mensching, M. Steger, R. Tielert, "A Pure CMOS Surface-micromachined Integrated Accelerometer", Sensors and Actuators, A57 (1996), pp. 111 – 116.

[16] M. Madou, Fundamentals of Microfabrication, Florida: CRC Press LLC, 1997.

[17] D.P. Askeland, The Science of Engineering Materials, Second SI Edition, London Chapman & Hall, 1990.

[18] L. Ristic (Editor), Sensor Technology and Devices, Boston: Artech House, 1994.

[19] J.M. Bustillo, R.T. Howe, R.S. Muller, "Surface Micromachining for Micro mechanical Systems", Proceedings of the IEEE, vol. 86, no. 8 (1998), pp. 1552-1574.

[20] G.T.A. Kovacs, N. I. Maluf, K. E. Peterson, "Bulk Micromachining", Proceeding of the IEEE, vol. 86, no. 8 (1998), pp. 1536-1551.

[21] W. Kern, C.A. Deckert, "Chemical Etching", Thin Film Processes, Vossen, J. L. and Kern, W., Eds., Academic Press, Orlando, 1978.

[22] H.F. Winters, J.W. Coburn, "The Etching of Silicon with XeF_2 Vapour", Appl. Phys. Lett., vol. 34, no. 1 (1979), pp. 70-73.

[23] K.R. Williams and R.S. Muller, " Etch Rates for Micromachining Processing", MEMS, vol. 5, no. 4 (1996), pp. 256-269.

[24] Y. Ma, Internal communication, University of Alberta, Edmonton, Alberta, Canada, 1999.

[25] M. Parameswaran, H.P. Baltes, L. Ristic, A.C. Dhaded and A.M. Robinson, "A New Approach for the Fabrication of Micromechanical Structures", Sensors and Actuators, A19 (1989), pp. 289 – 307.

[26] M. Parameswaran, "Microelectronic and Micromechanical Sensors and Actuators in CMOS Technology", PhD Thesis, University of Alberta, Canada, 1990.

[27] T. Zhou, "CMOS Cantilever Microresonator", MSc Thesis, University of Alberta, Canada, 2000.

[28] D.A. Johns and K. Martin, Analog Integrated Circuit Design, Wiley, 1997.

[29] S. Dew, EE 619 – Microelectronics Process Technology, Course Notes, University of Alberta, Canada, 1997.

[30] K.B. Brown, W. Allegretto, F. Vermeulen, and A.M. Robinson, "Cantilever-in-Cantilever Micro-Structures for Pressure and Magnetic Filed Measurement", Sym. Microelectronics R&D Can. (TEXPO '98), Ottawa, Canada, June 25-26, 1998.

[31] M. Spacek, K.B. Brown, Y. Ma, A.M. Robinson, R.P.W. Lawson, and W. Allegretto, "CMOS Cantilever Microstructures as Thin Film Deposition Monitors", IEEE Can. Conf. Electrical and Computer Engineering, Edmonton, 1999.

[32] M. Tabib-Azar, Microactuators: Electrical, Magnetic, Thermal, Optical, Mechanical, Chemical and Smart Structures, Kluwer Academic Publishers, 1998 Boston, Massachusetts.

[33] Website: mems.isi.edu/mems/materials/index.html

[34] B. Shen, W. Allegretto, Y. Ma, B. Yu, M. Hu, and A.M. Robinson, "Cantilever Micromachined Structures in CMOS Technology with Magnetic Actuation", Sensors and Materials, vol. 9, no. 6 (1997), pp. 347 - 362.

[35] H. Reismann, Elastic Plates: Theory and Application, New York: John Wiley and Sons, 1988.

[36] J.P. Den Hartog, Mechanical Vibration, Dover, 1985.

[37] C.S. Smith, "Piezoresistive Effect in Germanium and Silicon", Physical Review, vol. 94, no. 1 (1954), pp. 42 - 49.

[38] N. Svedin, E. Kalvesten, E. Stemme, and G. Stemme, "A New Silicon Gas-Flow Sensor Based on Lift Force", Journal of Microelectromechanical Systems, vol. 7, no. 3 (1998), pp. 303 – 308.

[39] G. Lin, K. S. J. Pister, and K. P. Roos, "Novel Microelectromechanical System Force Transducer to Quantify Contractive characteristics From Isolated Cardiac Muscle Cells", Journal of the Electrochemical Society, vol. 142, no. 3 (1995), pp. L31 – L33.

[40] R.C. Dorf, ed., The Electrical Engineering Handbook, CRC Press, Florida, pp. 1099-1105, 1993

[41] J.W. Seto, "Piezoresistive Properties of Polycrystalline Silicon", Journal of Applied Physics, vol. 47, no. 11 (1976), pp. 4780 - 4783.

[42] J. Chen, "Sub-nanogram Mass Sensor for In-Liquid Measurement", MSc Thesis, School of Engineering Science, Simon Fraser University, Canada, 1995.

[43] R.T. Fenner, Finite Element Methods for Engineers, The Macmillan Press Ltd, 1975 London.

[44] Swanson Analysis Systems, Inc., ANSYS User's Manual for Revision 5.3, Volume III – Elements, 1998.

[45] A.P. Boresi, R.J. Schmidt, O.M. Sidebottom, Advanced Mechanics of Materials, Fifth Edition, John Wiley & Sons, 1993, United States of America.

[46] G.K. Fedder, S. Santhanam, M.L. Reed, S.C. Eagle, D.F. Guillou, M.S.-C. Lu, L.R. Carley, "Laminated High-Aspect-Ratio Microstructures in Conventional CMOS Process", Sensors and Actuators, A57 (1996), pp. 103 – 110.

[47] R.C. Weast (Editor), Handbook of Chemistry and Physics – 56TH Edition, CRC Press, 1976 Cleveland, Ohio.

[48] D. Westberg, O. Paul, G.I. Anderson, H, Baltes, " A CMOS-compatible Device for Fluid Density Measurements", Proceedings of the 1997 Annual International Workshop on Micro Electro Mechanical Systems (1999), pp. 278 – 283.

[49] J. Wylde and T. Hubbard, "Elastic Properties and Vibration of Micromachined Structures Subject to Residual Stresses", IEEE Can. Conf. Electrical and Computer Engineering, Edmonton, 1999.

[50] B.M. Dutoit, P.A. Besse, H. Blanchard, L. Guerin, R.S. Popovic, "High Performance Micromachined Sm_2Co_{17} Polymer Bonded Magnets", Sensors and Actuators, A77 (1999), pp. 178 – 182.

APPENDIX

The following is a sample ANSYS command file, utilized to compile the FEM results presented in Chapter 5. The command file shown generates the static tip deflection value for the small micro-cantilever under the influence of a specified magnetic field and actuation current.

```
! Generate model
!
/FILNAM,Small_Static
/TITLE,Static Analysis
/PREP7
!-------------------------------------------------------------------------------------------
! Specify element type and element options

ET,1,solid46,0,0,1,0,2,0
KEYOPT,1,8,0
KEYOPT,1,9,
KEYOPT,1,10,0

!-------------------------------------------------------------------------------------------
! THE FOLLOWING SECTION DEFINES THE REAL CONSTANT SET 1
! FOR AREAS WITHOUT POLYSILICON
!-------------------------------------------------------------------------------------------
! The following is to be used when the nitride layer is included in the model

!R,1,4,0,1,4,,          ! The 0 indicates not to mirror layers about the mid-plane
!RMORE,2,,,,,          ! The 2 indicates to take the top of the element as the
                       ! reference  plane
!RMORE,1,90,1.0*0.5,2,90,0.5   ! Includes layer thicknesses,
!RMORE,3,90,0.8,2,90,2.65      ! material properties and orientations

!-------------------------------------------------------------------------------------------
! The following is to be used when the nitride layer is excluded in the model

R,1,3,0,1,2
RMORE,2,,,,,
RMORE,2,90,0.5,3,90,0.8
RMORE,2,90,2.65
```

```
!-------------------------------------------------------------------------------
! THE FOLLOWING SECTION DEFINES THE REAL CONSTANT SET 2
! FOR AREAS WITH POLYSILICON
!-------------------------------------------------------------------------------
! The following is to be used when the nitride layer is included in the model

!R,2,6,0,1,6,,
!RMORE,2,,,,,
!RMORE,1,90,1.0*0.5,2,90,0.5
!RMORE,3,90,0.8,2,90,1.35
!RMORE,4,90,0.3,2,90,1.0

!-------------------------------------------------------------------------------
! The following is to be used when the nitride layer is excluded in the model

R,2,5,0,1,5,,
RMORE,2,,,,,
RMORE,2,90,0.5,3,90,0.8
RMORE,2,90,1.35,4,90,0.3
RMORE,2,90,1.0

!-------------------------------------------------------------------------------
!-------------------------------------------------------------------------------
! Define material properties

! Young's modulus for various layers
! Young's modulus is defined in (kg.microns/s^2)/(microns^2)

MP,EX,1,380000          ! Young's modulus for Nitride
MP,EX,2,75000           ! Young's modulus for Oxide
MP,EX,3,70000           ! Young's modulus for Aluminum
MP,EX,4,150000          ! Young's modulus for Polysilicon

!-------------------------------------------------------------------------------
! Density for various layers
! Density is defined in kg/micron^3

MP,DENS,1,3.1e-15       ! Density for Nitride
MP,DENS,2,2.2e-15       ! Density for Oxide
MP,DENS,3,2.7e-15       ! Density for Aluminum
MP,DENS,4,2.32e-15      ! Density for Polysilicon

!-------------------------------------------------------------------------------

/PREP7
```

```
! Specify parameters for creation of volumes
! Place origin in center of device
! All dimensions given in microns

L=430                    ! L=length of main platform
space=5                  ! space=distance from origin to corner of arm1
w1=33                    ! width of arm1
w2=20                    ! width of remaining arms
arm1=175                 ! arm'x' specifies the length of given arms
arm2=90
arm3=135
arm4=65
t=3.95+0.0*0.5           ! t=thickness of structure+N layer thickness
a2=w1+arm2
a3=w1+w2+arm2
a6=w1+w2+arm2+arm4
a7=w1+w2+arm2+arm4+L

! Create device geometry
block,0,w1/2,0,-space,0,t
block,w1/2,w1,0,-space,0,t
block,0,w1/2,-space,-(space+w2/2),0,t
block,w1/2,w1,-space,-(space+w2/2),0,t
block,0,w1/2,-(space+w2/2),-(space+w2),0,t
block,w1/2,w1,-(space+w2/2),-(space+w2),0,t

delta=(arm1-w1/2)/2
block,0,w1/2,-(space+w2),-(space+w2+delta),0,t
block,w1/2,w1,-(space+w2),-(space+w2+delta),0,t
block,0,w1/2,-(space+w2+delta),-(space+w2+arm1),0,t
block,w1/2,w1,-(space+w2+delta),-(space+w2+arm1),0,t


block,w1,a2,-space,-(space+w2/2),0,t
block,w1,a2,-(space+w2/2),-(space+w2),0,t


block,a2,(a2+w2/2),-space,-(space+w2/2),0,t
block,(a2+w2/2),a3,-space,-(space+w2/2),0,t
block,a2,(a2+w2/2),-(space+w2/2),-(space+w2),0,t
block,(a2+w2/2),a3,-(space+w2/2),-(space+w2),0,t

block,a2,(a2+w2/2),-(space+w2),-(space+w2+arm3/2),0,t
block,(a2+w2/2),a3,-(space+w2),-(space+w2+arm3/2),0,t
block,a2,(a2+w2/2),-(space+w2+arm3/2),-(space+w2+arm3),0,t
block,(a2+w2/2),a3,-(space+w2+arm3/2),-(space+w2+arm3),0,t
```

```
block,a2,(a2+w2/2),-(space+w2+arm3),-(space+w2+arm3+w2/2),0,t
block,(a2+w2/2),a3,-(space+w2+arm3),-(space+w2+arm3+w2/2),0,t
block,a2,(a2+w2/2),-(space+w2+arm3+w2/2),-(space+2*w2+arm3),0,t
block,(a2+w2/2),a3,-(space+w2+arm3+w2/2),-(space+2*w2+arm3),0,t

block,a3,a6,-(space+w2+arm3),-(space+w2+arm3+w2/2),0,t
block,a3,a6,-(space+w2+arm3+w2/2),-(space+2*w2+arm3),0,t

block,a6,(a7-w2/2),-(space+w2+arm3),-(space+w2+arm3+w2/2),0,t
block,a6,(a7-w2/2),-(space+w2+arm3+w2/2),-(space+2*w2+arm3),0,t
block,(a7-w2/2),a7,-(space+w2+arm3),-(space+w2+arm3+w2/2),0,t
block,(a7-w2/2),a7,-(space+w2+arm3+w2/2),-(space+2*w2+arm3),0,t

block,a6,(a7-w2/2),0,-(space+w2+arm3),0,t
block,(a7-w2/2),a7,0,-(space+w2+arm3),0,t

VSYMM,Y,ALL,,,0,          ! Mirror above objects

VGLUE,ALL                 ! Glue all volumes


!-----------------------------------------------------------------------------------
! Create mesh by specifying number of elements along given lines
a1=5                      ! Elements along 1/2 width of arms + edges of platform
a2=5                      ! Elements along 1/2 width of rigid support arms
b1=30                     ! Elements along 1/2 arm1
b2=30                     ! Elements along 1/2 arm1
c=15                      ! Elements along arm2
d=15                      ! Elements along 1/2 arm3
e=10                      ! Elements along arm4
f=40                      ! Elements along platform length
g=8                       ! Elements along 1/2 width of platform


lesize,742,,,1,,,,,       ! Specify only one element along thickness

lesize,783,,,a1,,,,,
lesize,855,,,a1,,,,,
lesize,851,,,a1,,,,,
lesize,771,,,a1,,,,,
lesize,796,,,a1,,,,,
lesize,868,,,a1,,,,,
lesize,806,,,a1,,,,,
lesize,878,,,a1,,,,,
lesize,895,,,a1,,,,,
lesize,891,,,a1,,,,,
```

```
lesize,819,,,a1,,,,,
lesize,823,,,a1,,,,,
lesize,958,,,a1,,,,,
lesize,1016,,,a1,,,,,

lesize,485,,,a2,,,,,
lesize,996,,,a2,,,,,
lesize,101,,,a2,,,,,
lesize,964,,,a2,,,,,

lesize,863,,,b1,,,,,
lesize,791,,,b1,,,,,

lesize,859,,,b2,,,,,
lesize,787,,,b2,,,,,

lesize,800,,,c,,,,,
lesize,872,,,c,,,,,

lesize,881,,,d,,,,,
lesize,809,,,d,,,,,
lesize,886,,,d,,,,,
lesize,814,,,d,,,,,


lesize,832,,,e,,,,,
lesize,902,,,e,,,,,

lesize,970,,,f,,,,,
lesize,1012,,,f,,,,,

lesize,846,,,g,,,,,
lesize,843,,,g,,,,,


MSHKEY,1              ! Specify mapped meshing
VMESH,ALL             ! Mesh all volumes

! Modify elements of Real Constant set 1 by converting them
! into Real Constant set 2; modified elements contain piezoresistive
! material

EMODIFY,2931,REAL,2
*REPEAT,12,1

EMODIFY,2946,REAL,2
```

```
*REPEAT,12,1

EMODIFY,451,REAL,2
*REPEAT,12,1

EMODIFY,436,REAL,2
*REPEAT,12,1

EMODIFY,2041,REAL,2
*REPEAT,12,1

EMODIFY,2056,REAL,2
*REPEAT,12,1

EMODIFY,4171,REAL,2
*REPEAT,12,1
EMODIFY,4156,REAL,2
*REPEAT,12,1

EMODIFY,2972,REAL,2
EMODIFY,432,REAL,2
EMODIFY,2082,REAL,2
EMODIFY,4152,REAL,2

EMODIFY,3076,REAL,2
*REPEAT,10,1

EMODIFY,2881,REAL,2
*REPEAT,10,1

EMODIFY,3066,REAL,2
*REPEAT,3,1

EMODIFY,3071,REAL,2
*REPEAT,3,1

EMODIFY,22,REAL,2
*REPEAT,4,1

EMODIFY,27,REAL,2
*REPEAT,4,1

EMODIFY,17,REAL,2
*REPEAT,3,1

EMODIFY,92,REAL,2
```

```
*REPEAT,3,1

EMODIFY,3476,REAL,2
*REPEAT,10,1

EMODIFY,3696,REAL,2
*REPEAT,10,1

EMODIFY,3706,REAL,2
*REPEAT,3,1

EMODIFY,3711,REAL,2
*REPEAT,3,1

EMODIFY,1647,REAL,2
*REPEAT,4,1

EMODIFY,1652,REAL,2
*REPEAT,4,1

EMODIFY,1662,REAL,2
*REPEAT,3,1

EMODIFY,1657,REAL,2
*REPEAT,3,1

FINISH

!-------------------------------------------------------------------------------
! Apply loads and obtain the solution
/SOLUTION

ANTYPE,STATIC        ! Indicate static analysis

DA,243,all,0,,       ! Constrain all DOF on given areas
DA,608,all,0,,       ! ie. areas in contact w/ channel wall
DA,51,all,0,,
DA,572,all,0,,

! Define forces that will act on structure
Lplat=3.5e-4         ! Length of Al trace in platform [m]
L2=1.65e-4           ! Length of trace in arm3 [m]
L1=1.90e-4           ! Length of trace in arm1 [m]

I=(1/1000)           ! Magnitude of current [A]
B=0.075              ! magnitude of magnetic field [N/A.m]
```

```
!-------------------------------------------------------------------------------
! Define forces at keypoints
! All forces have units of [kg.microns/s^2]

! Apply load at end of platform
Fplat=(I*Lplat*B/3)*(1000000)
FK,470,FZ,Fplat,
FK,247,FZ,Fplat,
FK,214,FZ,Fplat,

! Apply load on arm3
F3=(-I*L2*B/3)*(1000000)
FK,422,FZ,F3,
FK,390,FZ,F3,
FK,358,FZ,F3,
FK,102,FZ,F3,
FK,134,FZ,F3,
FK,166,FZ,F3,

! Apply load on arm1
F1=(I*L1*B/3)*(1000000)
FK,326,FZ,F1,
FK,310,FZ,F1,
FK,278,FZ,F1,
FK,22,FZ,F1,
FK,54,FZ,F1,
FK,70,FZ,F1,
```

Harmonic and modal analyses for the micro-cantilever structures are performed by replacing the solution phase of the above code with ANSYS commands prevalent to the desired analysis. More information can be found in the ANSYS user manuals.